Model-Based Vibration Diagnostic of Cracked Beams in the Time Domain

Sergio H. S. Carneiro

Dissertation submitted to the Faculty of the
Virginia Polytechnic Institute and State University
in partial fulfillment of the requirements for the degree of

Doctor of Philosophy
in
Engineering Mechanics

Daniel J. Inman, Chairman
Mehdi Ahmadian
Romesh C. Batra
Norman E. Dowling
Surot Thangjithan

August 15, 2000
Blacksburg, Virginia

Keywords: Vibrations, Damage Detection, Cracked Beams, Genetic Algorithms

Model-Based Vibration Diagnostic of Cracked Beams in the Time Domain

Sergio H. S. Carneiro

(ABSTRACT)

A time-domain model-based crack diagnostic methodology using vibration data is presented. Most of the damage detection methods proposed to date are based on modal parameters and are limited by the loss of information caused by data reduction and by the implicit assumption of linearity. The use of time domain information permits the direct inclusion of the nonlinear behavior due to crack opening-closure cycles. In addition, very little information is lost, since no signal processing or parameter identification steps are involved. The proposed method is based on a continuous model for the transverse vibrations of beams consisting of partial differential equations of motion with varying coefficients to account for the presence of damage. In order to provide accurate representation of the structure's behavior over a broader frequency range, a new continuous cracked beam model including shear effects and rotatory inertia is developed using the Hu-Washizu-Barr variational method. The resulting equations of motion are discretized by a Galerkin method using local B-splines as test functions. The crack is assumed to be either fully open or fully closed, resulting in a bilinear system. The simultaneous identification of crack location and depth is performed by minimizing the norm of the differences between the numerical and experimental time responses to multiple excitations. Impact, low frequency sinusoidal and Schröeder–phased multisine inputs are investigated as potential excitation methods. The cost function to be minimized presents several local minima that are shown to be related to the length of the response records. A genetic algorithm is used to overcome the multimodal nature of the objective function. The methodology is validated through simulated identifications of several damage scenarios. The importance of the inclusion of the nonlinear behavior is addressed, and the effects of model uncertainties and measurement noise are quantified in terms of minimum identifiable crack size.

Dedication

To Lúcia, Pedro and Letícia.

Acknowledgments

First, I must thank my wife Lúcia for all the support over the four years we spent in Blacksburg. It started even before that, when the idea of leaving Brazil with two small kids was never a problem to her. Through the years, the same positive attitude towards the hand we were dealt in life was always present, and that's what gave me the confidence I needed to keep going. I could not ask for a stronger demonstration of love, which I promise I will always try to match. Huge thanks to my kids, Pedro and Letícia, for the much needed reenergizing breaks, even when it meant less sleep or extra physical activities. You were the real inspiration for everything I've accomplished.

I am also immensely grateful to my parents for the encouragement and support throughout my life. The sacrifices they've endured in order to provide education to their two kids were not always well understood in the neighborhood we grew up, but in the end I believe my brother and I are living proof of the discernment of their decisions. The best I can do to thank them is to do the same for their grandkids. I hope they started a family tradition that will last for ages to come.

Next, I'd like to say a special thanks to one of the most remarkable human beings I ever met, my supervisor Prof. Daniel J. Inman, who happens to be also one of the most gifted professionals I worked with in almost fifteen years of experience. From our relationship, I am afraid I am the one leaving with the best share: a role model for technical excellence and academic wisdom. Cheers!

I want to thank my committee, Professors Mehdi Ahmadian, Romesh C. Batra, Norman E. Dowling, and Surot Thanghjithan, and the former member Prof. Landgraf, for all the knowledge they shared with me through coursework, evaluation steps and discussions. It was a pleasure to work with such a group of talented educators and researchers. Thanks also to my masters advisor, Prof. José Roberto Arruda, who always encouraged me to continue my graduate studies. Thanks to all CIMSS members, to Prof. Leo for the helpful comments, and to the project manager Beth Howell for all the help, but especially for turning me, through example, into a Hokie fan. The price she'll pay is that I might ask her to tape a few games and mail me sports magazines in the future. Big thanks to the two Brazilian visiting professors, Profs. Vicente Lopes and Valder Steffen, for all the great suggestions and for the wonderful friendship our families developed during their stay.

My final acknowledgments go to the incredible group of people that were true "teammates" during the past years: Greg Agnes, Mauro Attala, Eric Austin, Clay Carter, Jens Cattarius, Dan Cole, Prasad Gade, Myung-Hyun Kim, Marca Lam, Gyuhae Park, Debbie Pilkey and Dino Sciulli. All the friendships I developed these past years are at least as important as the degree I earned. To the new generation, Luciano, Rodrigo, Kenji, Greg, and others to come: keep this special workplace atmosphere alive, including the Friday lunch tradition at Mike's. Very special thanks to Kim for the detailed review of the manuscript and for the much-needed discussions and keen suggestions. Big thanks to Jens and Melissa, who managed to find time between diaper changes to send their words of support all the way from Germany during my final stretch. A chat with Jens is always a great experience. Finally, huge thanks to now Prof. Eric Austin, with whom I shared the experience of going through a Ph.D. program while helping to raise two small children. His reviews and technical discussions were invaluable. I am happy for the students that will take advantage of his vast engineering knowledge and outstanding teaching skills.

This work was sponsored by the Brazilian Air Force under the technical and academic supervision of Lt. Col. Maurício Pazini Brandão. The author wishes to express his gratitude to all those in the Force that trusted his potential by selecting him for this mission, and he will make every effort to return the credit with the highest professional dedication to our great Country.

Contents

1 Introduction **1**

1.1 Motivation for Vibration-Based Damage Detection 1

1.2 No-Model versus Model-Based Diagnostics 3

1.3 Modal versus Time Domain Methods 6

1.4 Identification via Genetic Algorithm 7

1.5 Objectives 9

1.6 Overview 10

2 Review of Literature **11**

2.1 Introductory Remarks 11

2.2 Vibration-Based Damage Diagnostics 12

2.2.1 Historical Overview 12

2.2.2 Methods Based on Natural Frequency Shifts 13

2.2.3 Methods Based on Mode Shapes 14

2.2.4 Methods Based on FRFs 15

2.2.5 Methods Based on Structural Matrices 16

2.2.6 Time-Domain Methods 16
2.3 Vibrations of Cracked Structures 17
2.3.1 "Smeared" Crack Models 18
2.3.2 Lumped Flexibility Models 18
2.3.3 Continuous Models 20
2.3.4 Crack Opening-Closure Models 21
2.4 Genetic Algorithms 22
2.4.1 Historical Overview 22
2.4.2 Diagnostic Methods Using GA's 23
2.5 Summary 23

3 Derivation of Mathematical Model **24**

3.1 Introduction 24
3.2 The Hu-Washizu-Barr Variational Principle 25
3.3 Kinematic Assumptions 28
3.3.1 Normal Stress/Strain Disturbance Function 29
3.3.2 Shear Stress/Strain Disturbance Function 30
3.3.3 Displacement Disturbance Function 31
3.4 Derivation of the Equations of Motion 32
3.4.1 Strain-Displacement Term 32
3.4.2 Stress-Strain Energy Density Term 33
3.4.3 Velocity-Momentum Term 33

3.4.4 Dynamic Equilibrium Term 34
3.4.5 Differential Equations of Motion 34
3.4.6 Boundary Conditions 36
3.4.7 Calculation of Constants m_1 and m_2 37
3.5 Symmetric Form and Check of Self-Adjointness 38
3.6 Euler-Bernoulli Cracked Beam Model Revisited 42
3.6.1 Kinematic Assumptions 43
3.6.2 Equations of Motion 44
3.6.3 Boundary Conditions 44
3.6.4 Comments on Shen's Model 44
3.6.5 Proposed Modification 45

4 Numerical Implementation **47**

4.1 Introduction 47
4.2 Galerkin Discretization Using B-Splines 48
4.3 Model Validation 49
4.3.1 Convergence Study 49
4.3.2 Effects of Displacement Disturbance Function $g(x, z)$ 59
4.3.3 Influence of Aspect Ratio 63
4.3.4 Comparison with data from literature 67
4.3.5 Comparison with Finite Element Model 72
4.4 Computation of Time Responses 76

4.4.1 General Procedure 76
4.4.2 Damping Model 79
4.4.3 Representation of Crack Closure 80
4.4.4 Adaptive Time Step Implementation 81
4.4.5 Excitations 82
4.4.6 Numerical Response Results 85

5 Time Domain Crack Diagnostic via Genetic Algorithms 92

5.1 Introduction 92
5.2 Basics of Genetic Algorithms 94
5.2.1 Selection 98
5.2.2 Crossover Operators 99
5.2.3 Mutation Operators 101
5.3 Implementation of the Identification Procedure 103
5.4 Results 104
5.4.1 Definition of Test Cases 104
5.4.2 GA Parameters 106
5.4.3 Excitation Method 107
5.4.4 Effect of Noise 108
5.4.5 Influence of Nonlinearities 109
5.4.6 Effect of Model Uncertainties 111

6 Conclusions, Contributions and Future Work **118**

6.1 Conclusions 118

6.2 Contributions 124

6.3 Future Work 125

6.4 Closing Remarks 126

A Euler-Bernoulli Cracked Beam Models **138**

A.1 Check of Self Adjointness of Shen's Model 138

A.2 Proposed Correction 139

B Cubic B-Spline Functions **145**

B.1 Preliminary Remarks 145

B.2 Mathematical Definitions 146

B.3 Test Functions for Galerkin Discretization of PDE's 147

List of Figures

3.1 Typical geometry of a cracked beam 28

3.2 Crack function for normal stress disturbance f_1. 30

3.3 Crack function for shear stress disturbance f_2. 31

4.1 Comparison of convergence characteristics of the Euler and Timoshenko models for undamaged short and slender simply supported beams. 52

4.2 Comparison of convergence characteristics of the Euler and Timoshenko cracked beam models. Crack depth ratio $a/2d = 0.1$. 53

4.3 Comparison of convergence characteristics of the Euler and Timoshenko cracked beam models. Crack depth ratio $a/2d = 0.3$. 54

4.4 Comparison of convergence characteristics of the Euler and Timoshenko cracked beam models. Crack depth ratio $a/2d = 0.5$. 55

4.5 Comparison of convergence characteristics of the Euler and Timoshenko cracked beam models. Curves normalized to the same element length. Crack depth ratio $a/2d = 0.5$. 56

4.6 Variations of natural frequencies due to increase in crack depth for different levels of discretization of a short, simply-supported beam, $L/2d = 5$. 57

4.7 Variations of natural frequencies due to increase in crack depth for different levels of discretization of a slender, simply-supported beam, $L/2d = 20$. 58

4.8 Influence of displacement disturbance function g on the natural frequencies of a simply supported slender beam, $L/2d = 24.65$, $x_c/L = 0.2$. 60

4.9 Influence of displacement disturbance function g on the natural frequencies of a simply supported slender beam, $L/2d = 24.65$, $x_c/L = 0.3$. 61

4.10 Influence of displacement disturbance function g on the natural frequencies of a simply supported slender beam, $L/2d = 24.65$, $x_c/L = 0.4$. 62

4.11 Differences in natural frequencies estimated by Euler and Timoshenko models as a function of aspect ratio for a simply supported beam with a midspan crack. . . . 67

4.12 Variation of normalized natural frequencies of simply supported beams with respect to crack depth. $x_c/L = 0.5$. 68

4.13 Variation of normalized natural frequencies of simply supported beams with respect to crack location. Short beam: $L/2d = 4$; Slender beam: $L/2d = 20$; Crack depth: $a/2d = 0.3$. 69

4.14 Influence of crack depth on displacement mode shapes of a simply supported Timosehnko cracked beam. $x_c/L = 0.5$. 70

4.15 Influence of crack depth on rotation mode shapes of a simply supported Timoshenko cracked beam. $x_c/L = 0.5$. 71

4.16 Comparison of finite element model and beam theory results for the first and second natural frequencies of a simply supported beam with a midspan crack.$L/2d = 20$. FE results from Reference [101]. 72

4.17 Comparison of finite element model and beam theory results for the third natural frequencies of a simply supported beam with a midspan crack. $L/2d = 20$. FE results from Reference [101]. 73

4.18 Comparison of experimental and beam theory results for the first and third natural frequencies of a simply supported beam with a midspan crack. $L/2d = 25.64$. Experimental results from Reference [101]. 73

4.19 Finite element model of a simply supported short beam, with detailed illustration of the mesh at the cracked region. $L/2d = 5$. 75

4.20 Variations of the normalized values of natural frequencies of a short simply supported beam with a midspan crack. $L/2d = 5$. Left-hand-side plots: values normalized by the undamaged natural frequency from the corresponding model; right-hand-side plots: values normalized by the undamaged natural frequency from the 2-D FE model. 78

4.21 Block diagram of the adaptive time step algorithm to identify crack opening/closure instants. 83

4.22 Time responses due to initial velocity at tip computed with different combinations of time step and adaptive refinement tolerance. 84

4.23 Time responses to a 5 Hz sinusoidal excitation at the tip. 86

4.24 Power Spectrum of the responses to a 5 Hz sinusoidal excitation at the tip. 86

4.25 Time responses to a unit initial tip velocity. 87

4.26 Power Spectrum of the responses to a unit initial tip velocity. 87

4.27 Schröeder phased multi-sine excitations. 88

4.28 Time response to a Schröeder phased input in the vicinity of the first and second natural frequencies. $a/2d = 0.05$. 89

4.29 Time response to a Schröeder phased input in the vicinity of the first and second natural frequencies. $a/2d = 0.25$. 90

4.30 Time response to a Schröeder phased input in the vicinity of the first and second natural frequencies. $a/2d = 0.50$. 91

5.1 Time histories and power spectra for a single-degree-of-freedom system in free vibration. Damage state corresponds to a 1% drop in the undamped natural frequency. 94

5.2 Effect of the time record length on the objective function for a SDOF system under free vibration. 95

5.3 Objective function obtained from forced vibration responses of a cracked cantilever beam: one measured point, three narrow band excitations. Crack parameters: $a/2d = 0.5$, $x_c/L = 0.2$. 96

5.4 Block diagram of a typical genetic algorithm with schematic illustration of the basic genetic operators in binary form. 97

5.5 Flow chart of the proposed time-domain, model-based crack diagnostic procedure. 103

5.6 Evolution of fitness function for a population of 200 individuals. 106

5.7 Time responses to first Schröeder excitation. Damage case B. 109

5.8 Effect of noise on diagnostic results. Damage case L ($x_c/L = 0.15$, $a/2d = 0.04$). Loading cases 2S and 3S. 116

5.9 Comparison of diagnostic results using the open crack model and the breathing crack model. Damage case L ($x_c/L = 0.15$, $a/2d = 0.1$). Loading case 3S. 116

5.10 Comparison of diagnostic results using the Euler Bernoulli model and the Timoshenko model with fitness functions $\mathbf{J}$ and $\bar{\mathbf{J}}$. Damage case L ($x_c/L = 0.15$, $a/2d = 0.1$). Loading case 3S, no noise added. 117

5.11 Comparison of diagnostic results using the Euler Bernoulli model and the Timoshenko model with fitness functions $\mathbf{J}$ and $\bar{\mathbf{J}}$. Damage case L ($x_c/L = 0.15$, $a/2d = 0.1$). Loading case 3S, noise level 5%. 117

B.1 Basis of cubic B-splines for N=10. 147

List of Tables

4.1 Differences in natural frequencies computed with both cracked beam models (reference: undamaged value obtained via Timoshenko model). 65

4.2 Changes in normalized natural frequencies for selected crack depth ratios (reference: undamaged value from the same model). 66

4.3 Properties of simply supported short beam for validation against FE model. . . . 74

4.4 Comparison of natural frequencies for a short simply supported beam with a mid-span crack.$L/2d = 5$. 77

4.5 Properties of cantilever beam for computation of time responses. 79

4.6 Comparison of relative execution time for adaptive time step procedure. 82

5.1 Definition of damage scenarios 104

5.2 Definition of loading cases for investigations on the influence of excitation method. 105

5.3 Numerical parameters used for generations of simulated experimental data and numerical model responses 105

5.4 Preliminary identifications for definition of GA parameters 107

5.5 Genetic algorithm parameters selected for the identification runs 107

5.6 Comparison of identification results using different excitations 108

5.7 Effect of noise on minimum identifiable crack for loading cases 2S and 3S. 110

5.8 Influence of nonlinearity on identification results. 111

5.9 Comparison between diagnostic results using the Euler-Bernoulli and Timoshenko model with fitness funtions $\mathbf{J}$ and $\bar{\mathbf{J}}$. No noise added. 113

5.10 Comparison between diagnostic results using the Euler-Bernoulli and Timoshenko model with fitness funtions $\mathbf{J}$ and $\bar{\mathbf{J}}$. Noise level: 2%. 114

5.11 Damping coefficients for model uncertainty investigations. 115

5.12 Effect of uncertainties in model damping coefficients on diagnostics 115

Chapter 1

Introduction

1.1 Motivation for Vibration-Based Damage Detection

Over the past few years, the problem of detecting structural damage in mechanical, aeronautical and civil engineering systems has been the subject of numerous research papers and conferences. Traditional nondestructive evaluation (NDE) techniques, such as ultrasonic emission, X-radiography analysis, Eddy current, etc., can detect small-scale flaws, but these methods usually require that the structure/system under investigation be taken out of service for inspection at pre-set time intervals. The inspection procedure can be very expensive and time consuming, especially when it involves components at inaccessible locations. This has motivated the research of new NDE techniques that can be applied to in-service structures, reducing maintenance costs and improving safety as well as system performance. Recent technological advances have renewed interest in damage detection research. Innovative sensing technologies, increased computational power, improvements in signal processing techniques, and the development of new material systems can all be combined to create self-sensing, automatically monitored structural systems with a broad range of potential applications.

The aeronautical industry, a traditional leader in the development of new technologies, has contributed two problems on opposite ends of the spectrum. On one hand, the development of a new generation of aircraft could incorporate automated, real-time monitoring of structural integrity to meet the requirements of increasing performance and reduced operational costs. On the other hand, the challenges of an aging aircraft fleet must also be met. Due to economic factors, both commercial and military aircraft operators are considering the extension of the life spans of some airplanes well beyond their original design lives, hence greatly increasing the needs for reliable maintenance procedures. This requires the development of inspection techniques that could preserve and possibly improve current safety and reliability levels and concurrently reduce downtime and labor-related costs.

Civil infrastructure is also an area with interesting technical challenges, either related to aging bridges and buildings or to the development of structural systems capable of fast integrity assessments in the case of an earthquake. Offshore structural systems are also extremely difficult to be inspected and could benefit from the development of automated structural monitoring techniques. In summary, the demands for new structural health monitoring methods are evident. However, the current level of maturity of this technology is still incipient and numerous basic questions have to be addressed.

One of the most popular approaches in detecting damage is the use of vibration data as a basis for structural health monitoring. Since presumably the presence of damage causes a change in the mass, stiffness and/or damping characteristics of a structure, the vibration responses due to operating loads or applied inspection loads will also change. Vibration-based damage detection can be defined mathematically as a nonlinear inverse problem where the changed vibration responses are known and the parameters that determine location and extent of the damage causing those changes are the variables to be identified.

According to Rytter [92], the problem of damage diagnostics in general can be approached at four different levels:

Level 1 : detecting the existence of damage in the structure;

Level 2 : Level 1 plus determination of the damaged site;

Level 3 : Level 2 plus quantification of severity of damage;

Level 4 : Level 3 plus prediction of remaining service life of the structure.

Strictly speaking, the term damage detection would refer only to Level 1 diagnostic. However, the term has been loosely applied as equivalent to structural damage identification in general, including all four levels of diagnostics. Level 4 can be considered "uncoupled" from the previous three levels in the sense that, once the extent of damage is known, the problem of life prediction can be handled by means of fracture mechanics and fatigue-life analysis. This dissertation will focus on the first three levels of diagnostics.

1.2 No-Model versus Model-Based Diagnostics

Among the vibration-based structural health monitoring techniques one may find two distinct classes of methods: model-based techniques and no-model techniques. Each approach has its own intrinsic advantages and limitations. No-model methods have the advantage of avoiding modeling errors and computational costs involved in numerical simulations, which can pose severe limitations when iterative identification schemes are used. However, most no-model methods developed to date can only provide Level 1 and limited Level 2 damage identification. Furthermore, attempts of Level 2-3 diagnostics by means of no-model methods imply a considerable increase in number of sensors and consequent amount of signal processing. This indicates that, in order to achieve Level 3, a mathematical model of the structure is necessary. The level of model refinement needed to describe small flaws, as in the case of fatigue cracks, can be a considerable restriction. However, the use of a theoretical model can be advantageous in many aspects. For example,

- the use of a mathematical structure describing the dynamic system permits the application

of model-based parameter identification methods, possibly reducing the amount of experimental data required;

- it allows inexpensive off-line simulations of slight variations in the system, such as changes in physical parameters, boundary conditions, external influences, etc. These simulations can provide valuable information for pre-test procedures;

- the model can be used in the test design phase to optimize the number and location of sensors, actuators, and excitation/measurement cycles;

- the model can be used to easily generate extensive amounts of data, as needed for example in the training phase of neural-network-based monitoring schemes.

In addition, modeling errors inherent to theoretical models can be greatly reduced by using well-established model updating techniques. A good compromise between accuracy and simplicity is the most desired characteristic of a model used in any on-line health monitoring procedure.

The next important question now becomes, "What model would be suitable for the method we envision?" Most of the work on dynamics of cracked members deals with the *forward* problem, either quantifying the effects of a certain damage of known extent on the dynamic characteristics of the structure or predicting a nonlinear signature spectrum that would indicate the presence of damage. The computational cost is usually not a concern when dealing with the forward problem. Investigations on solving the *inverse* problem (localizing and quantifying a crack from the responses) are usually based on simplified linear models where the effect of the damage is represented by a local reduction in stiffness. We need a model that explicitly includes crack location and depth as model parameters and that is capable of representing the key characteristics of such a system. Specifically, this refers to the stress/strain concentration around the crack tip and the nonlinear behavior caused by crack closure, usually referred in the literature as "breathing" crack model. An accurate representation of the stress and strain fields due to the presence of a crack could be obtained

with the help of refined, 3D finite element models, which could also include the crack opening-closure feature by means of nonlinear interface elements or imposition of constraint equations. However, such a refined model would be very costly in computational time due to mesh resolution requirements, especially when time responses are to be computed. In addition, since crack depth and location are unknowns to be identified during the diagnosis process, automatic remeshing capabilities would be necessary, making the modeling task even more complicated and time consuming. In order to overcome these limitations, we seek a simplified model that can represent the basic characteristics of a cracked member at an acceptable computational cost.

The family of continuous models of cracked beams seen in recent publications stands as the natural choice to be used in the proposed methodology, since they rely on a description of the damaged structure in terms of partial differential equations. The first published continuous cracked beam model was proposed by Christides and Barr in 1984 [31] and later improved upon by Shen and Pierre [100, 101]; both cases were limited to Euler-Bernoulli beams. The basic idea is to obtain a continuous, one-dimensional mathematical model consisting of partial differential equations derived from a stationary variational principle, the so-called Hu-Washizu-Barr method [14, 56, 116]. The variational process makes it possible to account for the effect of stress/strain concentration in an approximate sense with the inclusion of "crack disturbance functions" into the kinematic assumptions. The resulting equations of motion already captures the locally distributed stiffness reduction due to the presence of damage as a function of crack location and depth.

Published results of damage detection based on modal parameters clearly indicate that a successful diagnosis is closely related to the number of modes included in the process [7]. Since the mathematical model must be as accurate as possible in the frequency range of interest, an Euler-Bernoulli formulation would not be adequate even in the case of slender beams, especially when excitation of higher frequencies is involved. Therefore, the concepts in Refs. [31, 100, 101] are used to derive a cracked beam model using Timoshenko theory. The resulting equations of motion can then be used in an identification procedure similar to

the one proposed by Banks and Inman, Ref. [12], for the computation of the time responses needed for damage diagnosis.

1.3 Modal versus Time Domain Methods

A very important aspect to consider is the choice of dynamic quantities used in the monitoring process. Friswell [40] presents a discussion of damage detection methods in terms of the measured data used, which can basically be in three forms: time series, frequency response functions (FRF's), and modal parameters. Time series are digitalized responses from sensors such as accelerometers, strain gauges, PZT sensors and other measuring devices. Frequency responses are obtained from time series by nonparametric estimation and signal processing techniques, usually through numerical Fourier transform. The FRF's are then used as the data source to the estimation of modal parameters through curve fitting methods of varying complexity level, depending on the amount of data in hand . Time series and FRF's are the main components of a typical modal test, a very well established experimental tool for the dynamic analysis of structures. Some potentially useful information is lost during each step of data reduction. In some cases, modal parameters can be directly estimated from time responses, but the extent of data compression remains the same. For a linear system, it is possible to accomplish intensive data reduction, from time series to a modal model, without significant loss of relevant information in the frequency range of interest.

Friswell also notes that the use of FRF's or modal parameters is equivalent for most linear cases. Although FRF data might contain some information from modes out of range, or from modes not captured during the curve fitting procedure, these advantages all but disappear provided the modal parameter estimation phase is careful and thorough. This is the main reason why the vast majority of technical papers published recently focus on diagnosis methods based on modal parameters such as natural frequencies, mode shapes, modal strain energy, strain mode shapes, etc., which have the appealing advantage of dealing with

a reduced volume of data. However, there are two main reasons why the use of modal parameters may be a serious limitation for the case of crack-type damage: first, the effect of small flaws on modal quantities, such as natural frequency shifts and local changes in the mode shapes, are usually very small and likely to be masked by experimental uncertainties and data reduction; and second, the assumption of linearity inherent in modal methods may introduce errors in the identification procedure. Frequency domain data may provide a quick, qualitative assessment of the presence of cracks, since the nonlinearity introduces peaks due to harmonics of the natural frequencies or combinations of those frequencies and the excitation frequency. This crack-signature analysis is limited to a Level 1 diagnostic, and the extension to Levels 2 and 3 would require complex nonlinear models in the frequency domain.

A promising alternative is the use of time responses in a model-based, iterative parametric identification procedure proposed by Banks, Inman and co-workers [12, 10], proven to be capable of detecting fairly small defects modeled as geometrical imperfections in the cross section of beams. The methodology involves a theoretical model based on a b-spline Galerkin approximation of the differential equations of equilibrium that provides both the accuracy and the simplicity required for a successful damage diagnosis. The use of time responses is less likely to be limited by data reduction problems, since the only differences from raw, analog data are due to the digital data acquisition process. Besides, the nonlinear behavior is also preserved, increasing the chances of a more realistic characterization of crack-type damage.

1.4 Identification via Genetic Algorithm

The most common approach for a model-based diagnosis involves conventional identification techniques such as the extended weighted least-squares implemented in Ref. [12]. A cost function is defined in terms of a metric between the measured and analytical comparison

quantities, and the damage parameters result from a minimization of that metric. The least-square estimation is a gradient-based minimization technique that requires either analytical or numeric evaluation of derivatives of the cost function with respect to the parameters to be estimated. The basic idea is to choose a starting point in the solution space, define a search direction from gradient information and perform a unidimensional minimization in the search direction to find a better solution. The process is iteratively repeated until convergence is achieved.

Damage detection problems result in numerous local minima in the defined objective function, and this introduces serious practical difficulties in finding the correct diagnosis. Under those conditions, convergence to the correct estimates (not known a priori) will be strongly dependent on a good initial guess. This may be acceptable if there is only a very small number of probable damage sites with well defined physical locations. Since this is not the case in general, gradient-based techniques are likely to fail in solving a crack diagnostic problem.

Genetic algorithms (GA's) [46, 55, 76] have recently become popular as an efficient alternative to solve complex design and optimization problems where conventional, gradient-based methods fail. They were developed using ideas borrowed from biological sciences such as genetics and natural evolution. The algorithm does not require the computation of derivatives, and it can be easily parallelized. In addition, it relies on a probabilistic exploration of the entire region of interest, so it is not hurt by a poor initial guess; therefore GA's offer a higher likelihood of identification of the global minimum. The methodology is relatively new, and most of the current applications are on design optimization and task planning problems, with only a few recent publications involving damage detection methods. In the proposed research a GA is introduced as part of the identification procedure in order to overcome the limitations imposed by the multimodal nature of the defined cost function.

1.5 Objectives

The goal of the present research is to investigate a model-based vibration diagnostic methodology that can be applied to cracked beams. To overcome the reported limitations of methods based on modal parameters to identify small defects, time responses are used as the comparison data for crack diagnostic. In the proposed research, a second advantage of using time domain information is the possibility of simulating the nonlinear behavior introduced by crack opening-closing cycles, believed to play an important role in the diagnostic procedure. The effects of the crack nonlinearity on the accuracy of the diagnostic will be quantified. Another important contribution of this work is the development of a new cracked beam continuous model which includes the effects of shear deformation and rotatory inertia, which permits the application of the proposed diagnostic method to short, stubby beam-like structures. The following steps are a breakdown of the proposed work and summarize the contributions:

- Extend the time-domain method developed by Banks to the case of cracked beams, including time responses that account for nonlinearities related to crack closure;
- Develop a continuous model for cracked beams that take into account shear deformation in order to provide better accuracy in a broader frequency range;
- Improve the detection capabilities by using a genetic algorithm for the identification procedure;
- Investigate and compare the effects of different excitations (impulsive, low-frequency sinusoidal and Schroeder-phased multisine pulse), as well as the length of the time response records, on the performance of the diagnostic procedure;
- Quantify the relative advantages and limitations of the linear and nonlinear models in terms of minimum identifiable crack size in the presence of noise, modeling errors, and uncertainties in material properties.

1.6 Overview

Chapter 2 is a literature review including the most relevant technical publications related to the present research. Chapter 3 presents the mathematical derivation of the equations of motion for a cracked beam including the effects of shear deformation by means of a mixed variational approach. A brief review of the continuous cracked Euler-Bernoulli beam model developed by Shen [100] is also presented along with a discussion of its mathematical and numerical limitations and the corresponding proposed solutions. Chapter 4 presents the numerical implementation of the equations derived in Chapter 3 together with validations against numeric and experimental data found in the literature for the case of slender beams. The solution is based on a Galerkin discretization using cubic b-splines as the basis for the admissible functions. To assess the advantages of the proposed model for the case of short beams, for which no literature data was found, a 2D finite element model is constructed and the results are used as reference for a quantitative comparison between the proposed model and the Euler-Bernoulli model. The computation of time responses is also discussed in Chapter 4, including a description of the bilinear model for the crack opening-closure cycles. Responses to impact, sinusoidal and Schroeder multisine inputs are presented with a discussion of the their potential use as excitations in the proposed diagnostic scheme. Chapter 5 describes the proposed model-based time-domain diagnostic procedure using a genetic algorithm for the parameter estimation phase. Simulations of different identification scenarios are presented, including selection of the excitation, investigation of the effects of model uncertainties and noise, and importance of the inclusion of the nonlinear effect. Finally, Chapter 6 presents the summary, conclusions, and contributions of the present research as well as suggestions for future work.

Chapter 2

Review of Literature

2.1 Introductory Remarks

The first systematic investigations on damage detection using vibration information appeared in the 1970s. Doebling [38] attributes the initial developments in this field to the offshore oil industry, while Dimarogonas [37] acknowledges the power generation industry for the first studies on the more specific problem of crack identification. Since the early 1980s the subject of damage detection using vibration data has received enormous attention from the engineering and research communities, with emphasis on (but not limited to) turbomachinery, civil engineering, and aerospace applications. In the 1990s, damage detection has become a recurrent topic for sessions in technical conferences and symposiums such as the SPIE conference [105] and the Structural Health Monitoring Workshop at Stanford University [23, 24], and it was the main theme of the 1997 annual International Modal Analysis Conference, with more than 400 papers presented [103]. The literature related to structural damage diagnostics is therefore quite extensive and involves a myriad of applications ranging from the health assessment of large infrastructure systems to the monitoring of miniature electronic components. An excellent source of information is the on-line damage detection database developed recently by Pappa et al. (2000) [82].

This chapter presents a review of the literature more directly related to the present research, including the publications regarded as cornerstones in the field of structural damage detection. Three main topics that are sometimes overlapping are discussed, but they cover the key aspects of this dissertation. First, a general review of detection methods based on vibration information without any restriction on the type of damaged is presented. Second, a survey of the investigations on vibrations of cracked members is presented. Finally, the development of genetic algorithms and its application to parameter estimation are discussed.

2.2 Vibration-Based Damage Diagnostics

2.2.1 Historical Overview

The early investigations in damage detection from vibration data were published well before the establishment of experimental modal analysis as a mainstream laboratory technique. Computational power and sensor technology were also very limited, which may explain why the first methods found in the literature are based on changes in natural frequencies alone. In his excellent review paper, Doebling [38] refers to Lifshitz and Rotem (1969) as the authors of the assumably first journal article to suggest the use of vibration data for damage diagnostics. Their work did not even refer directly to natural frequency shifts. Instead, they used changes in the dynamic moduli obtained from extensional and torsional stress-strain curves as indicators of damage in the form of delaminations in a composite specimen under dynamic loading.

Over the years, methods for damaged detection incorporated more sophisticated information as they become available both from laboratories and computer simulations. In fact, it was not until the late 1970s that more systematic investigations on natural frequency shifts, many of which including finite element models, appeared in scientific publications, and only in the 1980s did changes in mode shape changes and related quantities start to be considered as

potential damage indicators. In the following sections, the diagnosis methods are categorized and reviewed based upon which dynamic quantity is used in the procedure.

2.2.2 Methods Based on Natural Frequency Shifts

Damage diagnosis based on changes in natural frequencies was the first vibration-based method to appear in the literature, and to date they remain by far the most investigated. For a summary of methods based on natural frequencies only, see the review by Salawu (1997) [94]. Adams et al. (1978) [3] and Cawley and Adams (1979) [21] published what is usually referred as the first systematic attempt to detect damage from changes in natural frequencies. They use the ratio of frequency changes in two different modes as a function of the damage position only, and use this ratio for the localization process. The estimated magnitude of the damage is reported to be inaccurate. The method is based on a sensitivity analysis obtained via finite element model (FEM), requiring good accuracy from both the model and the experimental results. Stubbs and Osegueda (1990) [107, 108] further developed the sensitivity approach to also include better estimates of damage severity using fractional changes of the natural frequencies as damage indicators. Similarly, Armon et al. (1994) introduced a rank-ordering procedure according to fractional eigenfrequency shifts that is intended to overcome the requirements of high accuracy for the sensitivities and provide a method that is more robust with respect to measurement errors and model uncertainties. Friswell et al. (1994) [42] also extend Cawley and Adam's ideas with the introduction of statistical analysis for the identification of the best damage scenario, which can be seen as a forward method. The idea of using fractional changes is present in some form in most of the frequency-based methods found in the literature, including the ones published recently using modern approaches such as neural networks by Luo and Hanagud (1997) [69] and Mahmoud and Kiefa (1999) [70], and genetic algorithms by Friswell et al. (1998) [41].

2.2.3 Methods Based on Mode Shapes

The use of spatial information to improve the detection was first introduced by West in 1984 [118] using the Modal Assurance Criterion (MAC), which correlates mode shapes of the damaged and undamaged structure. Yuen (1985) [122] suggests the use of rotational mode shapes to characterize the presence of damage. Rizos et al. (1990) [89] suggest the use of mode shape information measured at only two locations. Recognizing that displacement mode shapes are fairly insensitive to the presence of local damage, Pandey et al. (1991) [80] suggested the use of curvature mode shapes instead. Chance et al. (1994) [22], Swamidas and Chen (1995) [110, 26], and Yam et al. (1996) [119] proposed the use of strain mode shapes that could be directly obtained from strain gauge measurements.

Simulations have shown that the use of mode shapes can indeed provide Level 2 and 3 diagnostics (see Section 1.1) in the studied situations, but experimentally identified modes lack the necessary measurement accuracy demanded by these procedures. In addition, either a very large number of sensors or a good a priori definition of potential damage sites is required for mode shape identification, posing an additional practical limitation. Hoesrt and Ratcliffe (1997) [53] propose the application of a Laplace operator to enhance the detectability potential of mode shape information. Stubbs et al. (1995) [106] proposed a damage index obtained from integrations of the mode shapes and uses it in a pattern recognition technique. Cornwell et al. (1997) [35] revisit the integral damage index describing it in terms of modal strain energy and extend the approach for plate-like structures. Yoo et al. (1999) [121] compare several damage indicators derived from the MAC and its variations and concludes, based on FE simulations of a cracked plate, that the use of absolute values of the differences of mode shapes is the best damage index.

Even if the stated practical limitations can be overcome, the theoretical benefits of including mode shapes in damage detection are a controversial subject. Some researchers regard mode shapes and related quantities capable of providing the much-needed spatial information not directly available from natural frequencies, thus increasing the chances of achieving Level 2

and 3 diagnostics. Others reply that the mode shapes are affected very little by the presence of local damage and the changes would be virtually indistinguishable from experimental errors typical even in careful mode shape identification. Although seemingly obvious, the best conclusion is that both sides are partially correct and the advantages of using mode shape information will depend on the type of structure under investigation. A complex truss would be a good candidate for the application of mode shape methods, since local damages on joints or individual members may result in large modal displacements in a large region, as in the cases investigated by Kam and Lee (1994) [62], and Kim and Bartkowicz (1997) [64]. On the other hand, attempts to detect cracks in geometrically uniform structures like beams and plates are unlikely to benefit from the use of mode shapes, which have been reported to present very little changes due to that type of damage [19].

2.2.4 Methods Based on FRFs

The peak magnitudes and anti-resonances in FRF's can provide some spatial information for diagnostic. Fritzen et al. (1997) [43] proposed the use of FRFs in a model-based solution to the inverse problem using QR decomposition to reduce the number of candidate damage parameters and improve numerical conditioning. Swamidas and Cheng (1997) [111] used strain FRFs as indicators of fatigue crack initiation and growth in a tubular joint. Lopes et al. (1997) [67] published a detection technique using neural networks in which the training phase is based on numeric FRFs computed from a finite element model previously updated using experimental FRFs from the undamaged structure. The method was experimentally validated by successfully detecting damage in the welded joint of a metallic structure. Perchard and Swamidas (1999) [83] suggest that displacement FRFs and strain FRFs can provide combined information for crack detection both from peak and off-peak regions. Recently, Sampaio et al. (2000) [95] published a comparative study of FRF-based methods and suggested the used of the strain energy obtained directly from FRFs as damage indicator.

2.2.5 Methods Based on Structural Matrices

Another family of methods uses structural matrices to identify damage by determining the degrees of freedom that correspond to the elements in an identified error or perturbation matrix. Mannan and Richardson (1990) [71] proposed the estimation of mass, stiffness, and damping matrices from measured modal data and use the differences to the corresponding undamaged matrices as a direct indication of damage location. Pandey and Biswas [79] use the first three measured natural frequencies and mode shapes to estimate flexibility matrices both from the intact and damaged structure, and they then use the difference between the two as damage indicator. More elaborate matrix-based techniques are derived from model updating methods, available in the literature since the late 1970s, in which the matrices of an analytical model are corrected to match experimental modal data by minimizing the norm of the corresponding perturbation matrices. Kim and Bartkowicz (1993) [63] discuss the influence of noise level, number of damage sites, number of measurement points, and number of modes in different matrix-based detection procedures and conclude that number os measurement points is the most relevant factor for the accuracy of the investigated methods.

In the 1990s, Zimmerman and co-workers have published numerous investigations on detection methodology using structural matrices. They proposed a minimum rank perturbation theory [123, 124] that produces perturbation matrices of the same rank as the number of modes used. Many developments followed from that method, including the use of changes in the damping matrix as damage indicator [102]. More recent publications include damage location using subspace recognition by Lopez and Zimmerman (2000) [68] and a hybrid expansion-reduction method based on linear matrix inequalities by Abdala et al. (2000) [1].

2.2.6 Time-Domain Methods

An alternative to using modal parameters is using time responses directly as the comparison quantity for the diagnostic procedure. One advantage of time-domain techniques is that

they avoid the implicit data reduction of modal analysis methods, which may cause the loss of important information about the structure's dynamics. Another advantage is that time-domain methods are not limited by the assumption of linearity as the modal analysis approach is. The main disadvantage of model-based, time-domain methods is that they may require considerable computational effort for the calculation of time responses. Qian et al. (1990) [86] proposed a method that used an ARMA model to estimate damage parameters from time responses, but he still presented results in terms of equivalent eigenfrequencies. Ostachowicz and Krawczuk (1990) [78] investigated crack identification from the maximum amplitudes of time responses.

Banks et al. (1996) [12] developed a model-based diagnostic procedure via a least-squares, sensitivity-based parameter estimation routine proven to be able to detect small geometric defects. They investigated Euler-Bernoulli beams with damaged in the form of circular holes modeled by a Galerkin method using b-splines. Masri et al. (1996) [73] proposed a neural network based detection scheme that uses time responses both in the training and detection phases. Cattarius and Inman (1997) [20] proposed a time-domain method that uses the beat phenomenon to characterize small differences between the responses of a damaged and undamaged linear structure without referring to a model. Seibold and Weinert (1996) [93] published a probabilistic time-domain method based on parameter estimation using a series of Kalman filters to locate cracks in rotor taking nonlinearities into account. The use of AR and ARMA regression coefficients obtained from time records has been recently investigated by Garcia and Osegueda (2000) [44] and Sohn et al. (2000) [104], while George et al. (2000) [45] propose a method based on nonlinear time-series and bispectral analysis.

2.3 Vibrations of Cracked Structures

We can group the different models of cracked structures in three basic categories [37]: equivalent reduction in local stiffness (here also referred as "smeared" crack models); lumped

flexibility models; and continuous cracked bar and beam models. In addition, we present a section dealing specifically with the crack closure phenomenon in dynamic analysis. The following is a review of the literature on each approach.

2.3.1 "Smeared" Crack Models

This approach usually consists of a finite element model of the structure in which the damage is represented by an equivalent reduction in the stiffness of a particular element or group of elements. The use of this approach to solve the inverse problem (localization and quantification of damage from vibration response) has been investigated by many authors, but is not considered here as an alternative to realistic crack modeling since the correspondence between crack severity and equivalent stiffness reduction is usually arbitrary and strongly dependent on model refinement. Better representations of the effect of a crack over a region may be achieved by developing special finite elements, as in Haisty and Springer (1988) [50] and Gounaris and Dimarogonas (1988) [47]. Ibrahim (1992) [58] proposes an elastoplastic finite element capable of accounting for the plastic deformations at the crack tip. Despite the level of sophistication in the element formulation in these approaches, the determination of the size of element to be used is somewhat arbitrary. An interesting application has been proposed by Friswell et al. [41] in which a smeared crack model is used as a Level 2 diagnostic to select regions where more detailed detection (refined Level 2 plus Level 3) is to be attempted.

2.3.2 Lumped Flexibility Models

This family of methods is based on substructuring concepts. The undamaged portions of the structure are modeled using standard techniques such FEM, component mode synthesis, or partial differential equations, and the crack is represented by lumped springs or by a compliance matrix, usually derived from the expression for the strain energy release rate

or stress intensity factors. The first investigations are attributed to Kirmser (1944) [65] and Thomson (1949) [112]. They represented the effect of a notch by equivalent forces and moments at the location of the geometrical discontinuity. Among the most referred publications in the literature we must cite investigations by Dimarogonas [36], who was arguably the first to propose the derivation of compliance constants from fracture mechanics results for vibration analysis.

Gudmundson (1983) [49] presents a method for modelling a Timoshenko cracked beam using a transfer matrix approach, later extended by Tsai and Wang (1996) [113] to characterize cracks in a nonuniform stationary shaft. Gudmundson's paper has the additional merit of compiling experimental results of his own and from Wedtland (1972) in his comparisons, providing a good source for the validation of new models. Araújo Gomes and Montalvão e Silva (1990,1991) [5, 6] also published investigations based on a lumped method with extensive experimental results for slender, free-free beams with fatigue cracks.

Ostachowicz and Krawczuk (1991) [77] investigated the vibrations of a cantilever beam with two cracks. The more specific applications to rotor dynamics deserved numerous investigations, well summarized by Wauer (1990) [117]. Collins, Plaut and Wauer (1991, 1992) [33, 34] published a method for the longitudinal vibration of a bar that is a combination of the equivalent force concept with the local compliance approach. They derive the local equivalent forces that replace the crack in a continuous model from the compliance expressions obtained by Papadopoulos and Dimarogonas (1986) [81], who investigated the coupling between longitudinal and bending vibrations of a beam when a crack is present. Ibrahim et al. (1987) [4] and Ismail et al. (1990) [60] proposed a lumped model of a cracked beam using an augmented bondgraph technique accounting for nonlinear behavior. Brandon and coworkers, (1995-1999) centered their investigations on crack closure effects using lumped flexibility models. Their work is reviewed in more detail in Section 2.3.4.

2.3.3 Continuous Models

This family of models was developed more recently in an attempt to explicitly incorporate the relevant crack parameters, i.e., location and depth, as part of the equations of motion of the cracked structure. Christides and Barr initially developed models for the transverse vibrations of a symmetric, double-edge cracked Euler-Bernoulli beam [31] and for the torsional vibration of a cracked bar [32]. Both models rely on the characterization of the stress concentration due to the crack by means of a decay function introduced in the kinematic assumptions used in a variational derivation of the equations of motion. The mixed variational theorem used is an extension of the Hu-Washizu stationary principle [56, 116, 87], and it is now referred to in the literature as the Hu-Washizu-Barr [14] principle. Christides and Barr's model was improved and extended in recent years by Shen and Pierre (1990-1998) [100, 101, 98, 99], first by introducing an alternative estimation of the decay parameter from 2D finite element models and later by applying the same ideas to develop a model for beams with a single edge "breathing" crack.

Chondros and Dimarogonas [27, 28, 30, 29] used a similar variational approach, but they derived the so-called crack functions from energy considerations and fracture mechanics concepts. Their approach is an attempt to combine Christides and Barr's ideas of a continuous model with Dimarongonas' previous investigations on using fracture mechanics concepts to determine compliance constants in lumped parameter models. The most appealing advantage of such combination is that no decay parameter would have to be estimated, and therefore the disturbance functions could be based solely on well-known, handbook-type fracture mechanics expressions of stress intensity factors. However, a word of caution is necessary regarding their continuous formulation since several steps of the derivations are obscure. First, pre-assumed mathematical forms of crack disturbance functions result neither from algebraic derivations nor from physical reasoning. Second, one of the key conclusions in Ref. [28] is that only the displacement field needs to be assumed; the stress and strain distributions would cancel out through the derivation of the differential equations of motion. If that

is correct, a mixed formulation would probably not be required and the whole formulation could be simplified drastically. Finally, some key mathematical steps lack the minimum necessary rigor and justifications and could not be reproduced, including the above-mentioned cancellation of the stress/strain functions. For these reasons, it was not possible to reproduce their results to further evaluate the merits of the formulation, and this methodology and its extension were disregarded in this research.

2.3.4 Crack Opening-Closure Models

Both the lumped models and the continuous models provide a description of the structure when a crack is present and open, i.e., they are initially linear models of damaged members. The nonlinear effect originated by the crack opening-closure cycles in dynamic problems is incorporated by combining the damaged and undamaged models by means of a convenient switching strategy. This is commonly referred in the literature as "breathing" crack models. Studies on this nonlinear behavior using perturbation models have been proposed, e.g., by Gudmundson (1982) [48], Tsyfanskii (1994) [114], Plakhtienko and Yasinskii (1995) [84], and Ballo (1997) [9].

A more direct approach is the numeric integration of the combined differential equations of motion in the time domain with iterative check of crack status using different control quantities. Changhe et al. (1989) [25] uses the angle between the instantaneous bending moment and the rotating tangent axis to determine the crack condition in an unbalanced rotor application, accounting for partial opening and closure. When the crack is assumed to be either fully open or fully closed, the resulting system is bilinear, which simplifies the analysis even further. Chu and Shen (1992) propose a modal decomposition in which the modal restoring force is represented by a square wave. Sundermeyer and Weaver (1995) [109] use the bending moment at the cracked section as the control variable. Ruotolo et al. (1996) [91] use the slopes at stations before and after the crack in a transfer matrix model as the indicator of crack status. Rivola and White (1998) [88] propose the use of bispectral

analysis for crack detection using a model in which the nonlinear switch is represented by a square wave representation of the stiffness constants, transforming the problem in a linear time-variant system.

Brandon and coworkers (1995-1999) [2, 15, 16, 17] published what are probably the most detailed investigations on the dynamic crack closure effects. They use component mode synthesis models to obtain a nonlinear signature, basically a forward Level 1 diagnosis. Their model accounts for coupling between longitudinal and transverse vibrations due to the crack and checks both the bending moment and slope at the crack section to perform the transitions. Since the independent calculation of bending and slope can be asynchronous, the model is referred as "almost" bilinear. They also compute crack interface forces and relative longitudinal displacements, which allows for the introduction of crack interface friction forces. The level of detail in the model is reported to make it computationally intensive and therefore no crack identification via solving the inverse problem has been attempted.

2.4 Genetic Algorithms

2.4.1 Historical Overview

The original idea of applying concepts of genetics and natural evolution to solve complex engineering problems is attributed to Holland (1975) [54]. He developed the first genetic algorithms (GA's) in binary form and attempted mathematical investigations on algorithm convergence based on schemata theory. In 1989, Goldberg, one of Holland's former students, published a more organized compilation of GA's theory and applications [46]. Genetic Algorithms gained popularity in the optimization community in the late 1980s and early 1990s, as shown on a survey by Bäck and Schwefel (1993) [8]. Michalewicz's book (1995) [75] discusses GA's in the context of Evolutionary Programming and presents detailed descriptions of the various binary and floating-point genetic operators. Houck et al. (1995) [55], at North

Carolina State University, developed the GA MATLAB toolbox used in the present work.

2.4.2 Diagnostic Methods Using GA's

The most attractive feature of a GA is the efficient handling of multimodal functions that are common in identification problems in general and in model-based damage detection in particular. Larson and Zimmerman (1993) [66] proposed a model refinement technique using GA's for the minimization of a cost function defined from the differences between experimental and numerical eigenvalues and eigenvectors. Mares and Surace (1996) [72] proposed using binary GA's to minimize an objective function for damage detection defined in terms of residual forces. Carlin and Garcia (1996) [18] investigated the optimal tuning of a binary GA for damage detection using simple mass-spring systems. Ruotolo and Surace (1997) [90] applied a binary GA to the problem of identifying multiple cracks, and they presented a comparative study on the use of different objective functions including natural frequencies, displacement mode shapes and curvature information. Friswell et al. (1998) [41] proposed a two-stage diagnostic method that uses a GA and a simplified model to determine the most likely damage sites. They then applied a gradient-based identification to refine the location and determine the extent of damage. Yap and Zimmerman (1998) [120] proposed improvements in the binary encoding to enhance the performance of GA's for the specific problems of damage detection.

2.5 Summary

The present literature survey provides a historical overview of the relevant research in three main branches leading to the topic of this dissertation. More specifically, a methodology is taken from each branch as "seed" for the present work: the ideas from Banks and Inman's time domain damage detection, Shen and Pierre's continuous model of cracked beams, and the recent application of genetic algorithms to structural health monitoring.

Chapter 3

Derivation of Mathematical Model

3.1 Introduction

In this chapter, the equations of motion and corresponding boundary conditions for the transverse vibrations of cracked beams including the effects of shear deformations are derived using the so-called Hu-Washizu-Barr variational principle. The main goal is to obtain a system of partial differential equations that account for the presence of a crack by introducing disturbance functions to the kinematic assumptions, thus modifying the stress and strain fields in the vicinity of the crack. The equations of motion derived are then shown to constitute a self-adjoint differential operator, which will guarantee symmetry and simplify the numerical computation of the matrices during the discretization. In order to provide the background for the comparisons and discussions in Chapter 4, the main results from the derivation of the Euler-Bernoulli cracked beam model developed by Shen [101] are also revisited, along with proposed modifications to overcome the mathematical inconsistencies.

3.2 The Hu-Washizu-Barr Variational Principle

The Hu-Washizu-Barr [14] variational method can be viewed as an extension of the Hellinger-Reissner stationary principle [87, 97]. Stationary methods, also called mixed variational principles, have the advantage of incorporating all the governing equations into a single functional and allowing independent kinematic assumptions of the displacement, strain, and stress fields. The dynamics analogies of these stationary methods are in fact statements of Hamilton's Principle for a continuum, in which stress-strain equations, strain-displacement equations, equilibrium equations, and both essential and natural conditions are included in one single functional. This is achieved by treating the additional relations as constraints and using the method of Lagrange multipliers.

Consider the general expression for the Hamilton's Principle for a continuous elastic body,

$$\delta \int_{t_1}^{t_2} H dt = \delta \int_{t_1}^{t_2} \left[T - (V + U) \right] dt = 0 \; . \tag{3.1}$$

In this expression, T is the kinetic energy, V is the potential energy of applied loads and U is the strain energy. Mathematically, these are defined as

$$T = \int_V (\frac{1}{2} \rho \frac{\partial u_i}{\partial t} . \frac{\partial u_i}{\partial t}) dV \; , \tag{3.2}$$

$$V = - \int_V (B_i u_i) dV - \int_{\mathcal{S}_1} \overline{g_i} u_i d\mathcal{S}_1 \; , \tag{3.3}$$

$$U = \int_V W(\epsilon_{ij}) dV \; , \tag{3.4}$$

where u_i are the displacements, B_i are the body forces, $\bar{g}_i$ are the surface tractions prescribed on surface $\mathcal{S}_1$, and $W(\epsilon_{ij})$ is the strain energy density. We wish to include the linear elastic strain-displacement equations

$$\epsilon_{ij} = \frac{1}{2}(u_{i,j} + u_{j,i}) \tag{3.5}$$

and the displacement boundary conditions defined on the surface $\mathcal{S}_2$

$$u_i = \overline{u_i} \;\; on \; \mathcal{S}_2 \tag{3.6}$$

into the functional. Define the Lagrange multipliers λ_{ij} and μ_i associated with the strain-displacement relations and the displacement boundary conditions, respectively. The extended form for the functional in Hamilton's Principle may now be written as

$$\begin{aligned}\bar{H} &= H + \int_V \left\{ [\epsilon_{ij} - \frac{1}{2}(u_{i,j} + u_{j,i})]\lambda_{ij} \right\} dV + \int_{\mathcal{S}_2} (u_i - \overline{u_i})\, \mu_i d\mathcal{S}_2 \\ &= \int_V \left\{ \frac{1}{2}\rho \dot{u}_i \dot{u}_i + B_i u_i - W(\epsilon_{ij}) + [\epsilon_{ij} - \frac{1}{2}(u_{i,j} + u_{j,i})]\lambda_{ij} \right\} dV + \\ &\quad + \int_{\mathcal{S}_1} \overline{g_i} u_i d\mathcal{S}_1 + \int_{\mathcal{S}_2} (u_i - \overline{u_i})\, \mu_i d\mathcal{S}_2 \end{aligned} \tag{3.7}$$

The first variation of the extended functional is set to zero, i.e.,

$$\delta H = \delta_u H + \delta_\epsilon H + \delta_\lambda H + \delta_\mu H = 0 \ , \tag{3.8}$$

and since the variations are arbitrary, we have

$$\delta_u H = 0, \ \ \delta_\epsilon H = 0, \ \ \delta_\lambda H = 0, \ \ \delta_\mu H = 0 \ , \tag{3.9}$$

both within the body and on its boundary. Variations with respect to the Lagrange multipliers will recover the constraint equations. The term δ_ϵ, corresponding to the variation in strains, leads to

$$\lambda_{ij} - \frac{\partial W}{\partial \epsilon_{ij}} = 0 \ \text{ in } V \ , \tag{3.10}$$

which implies that the Lagrange multipliers λ_{ij} are equal to the stress components σ_{ij}. The variation in the displacement components will produce a term with the form

$$\int_V \frac{1}{2}(\delta u_{i,j} + \delta u_{j,i})\lambda_{ij} dV = \int_V [\sigma_{ij} \delta u_{i,j}] dV \ , \tag{3.11}$$

where symmetry of the stress tensor has been considered. Using the divergence theorem on the last term yields

$$\begin{aligned}\int_V [\sigma_{ij} \delta u_{i,j}] dV &= \int_V [\sigma_{ij} \delta u_i]_{,j} dV - \int_V \sigma_{ij,j} \delta u_i dV = \\ &= \int_{\mathcal{S}} \sigma_{ij} n_j \delta u_i d\mathcal{S} - \int_V \sigma_{ij,j} \delta u_i dV \ , \end{aligned} \tag{3.12}$$

where $\mathcal{S} = \mathcal{S}_1 + \mathcal{S}_2$ is the total surface of the body and n_i is the outward normal. Combining the portion of the first right-hand side term in Eq. (3.12) over $\mathcal{S}_2$ with the term from the variation of the boundary integral over $\mathcal{S}_2$ in Eq. (3.7) and recalling that δu_i is arbitrary, we get

$$\sigma_{ij} n_j - \mu_i = 0 \ , \tag{3.13}$$

which implies that the Lagrange multipliers μ_i correspond to the surface tractions g_i acting on $\mathcal{S}_2$. The Hu-Washizu functional will therefore take the form

$$\bar{H} = \int_V \left\{ \frac{1}{2}\rho \dot{u}_i \dot{u}_i + B_i u_i - W(\epsilon_{ij}) + [\epsilon_{ij} - \frac{1}{2}(u_{i,j} + u_{j,i})]\sigma_{ij} \right\} dV$$
$$+ \int_{\mathcal{S}_1} \overline{g_i} u_i d\mathcal{S}_1 + \int_{\mathcal{S}_2} (u_i - \overline{u_i})\, g_i d\mathcal{S}_2 \ . \tag{3.14}$$

Barr [14] introduced an additional modification to the functional in order to allow independent variations of displacements u_i and velocities p_i. This is useful when deriving approximate solutions in which displacement components are to be introduced, but not the inertial forces associated with them, as in the case of the Euler-Bernoulli theory of beams. Barr extends the Hu-Washizu functional to be

$$J = \int_{t_1}^{t_2} \left\{ \int_V [\rho p_i \dot{u}_i - \hat{T}(p_i) - W(\epsilon_{ij}) + (\epsilon_{ij} - \frac{1}{2}(u_{i,j} + u_{j,i}))\sigma_{ij} + B_i u_i] dV + \right.$$
$$\left. + \int_{\mathcal{S}_1} \overline{g_i} u_i d\mathcal{S}_1 + \int_{\mathcal{S}_2} (u_i - \overline{u_i})\, g_i d\mathcal{S}_2 \right\} dt \ , \tag{3.15}$$

where $\hat{T}(p_i) = \frac{1}{2}\rho p_i p_i$ is the kinetic energy density expressed in terms of velocities as independent variables. When independent variations of displacements u_i, strains ϵ_{ij}, stresses σ_{ij}, and velocities p_i are considered, we now have

$$0 = \delta J = \int_{t_1}^{t_2} \left\{ \int_V \left[\rho p_i \delta \dot{u}_i + (\rho \dot{u}_i - \hat{T}(p_i)_{,p_i})\delta p_i + (\sigma_{ij} - W(\epsilon_{ij})_{,\epsilon_{ij}})\delta \epsilon_{ij} - \sigma_{ij} \delta u_{i,j} + \right.\right.$$
$$\left. + (\epsilon_{ij} - \frac{1}{2}(u_{i,j} + u_{j,i}))\delta \sigma_{ij} + B_i \delta u_i \right] dV + \int_{\mathcal{S}_1} \overline{g_i} \delta u_i d\mathcal{S}_1 +$$
$$\left. + \int_{\mathcal{S}_2} \left[g_i \delta u_i + (u_i - \overline{u_i})\, \delta g_i \right] d\mathcal{S}_2 \right\} dt \ . \tag{3.16}$$

The first term in Eq.(3.16) can be integrated by parts with respect to time, yielding

$$\int_{t_1}^{t_2} \left\{ \int_V \rho p_i \delta \dot{u}_i dV \right\} dt = \int_V \rho p_i \delta u_i dV \Big|_{t_1}^{t_2} - \int_{t_1}^{t_2} \left\{ \int_V \rho \dot{p}_i \delta u_i dV \right\} dt \ . \tag{3.17}$$

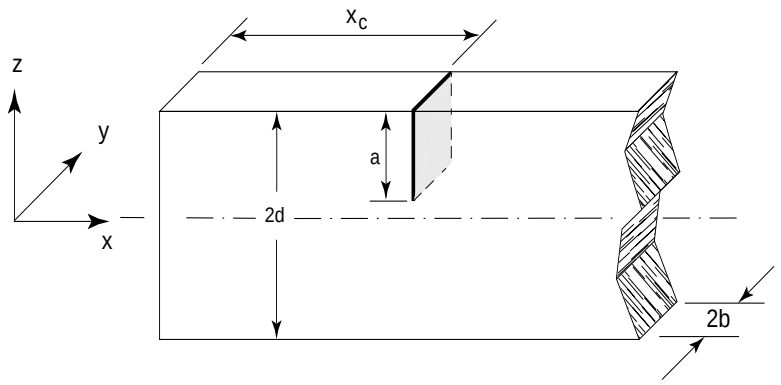

Figure 3.1: Typical geometry of a cracked beam

The first term in the right-hand side of Eq.(3.17) vanishes since the variations δu_i are assumed to be zero at t_1 and t_2 over the entire domain. Next, the term on $\delta u_{i,j}$ is modified using integration by parts and the divergence theorem, as described in Eq.(3.12). Collecting terms and recalling that $\sigma_{ij} n_i = g_i$, we arrive at the final form of the Hu-Washizu-Barr principle,

$$\int_V \{(\sigma_{ij,j} + B_i - \rho \dot{p}_i)\delta u_i + (\sigma_{ij} - W(\epsilon_{ij})_{,\epsilon_{ij}})\delta\epsilon_{ij} + [\epsilon_{ij} - \frac{1}{2}(u_{i,j} + u_{j,i})]\delta\sigma_{ij} +$$
$$+[\rho\dot{u}_i - \hat{T}(p_i)_{,p_i}]\delta p_i\}dV + \int_{\mathcal{S}_1} (\overline{g_i} - g_i)\delta u_i d\mathcal{S}_1 + \int_{\mathcal{S}_2} (u_i - \overline{u_i})\, \delta g_i d\mathcal{S}_2 = 0\ . \qquad (3.18)$$

The overbarred quantities $\overline{g_i}$ and $\overline{u_i}$ are prescribed surface tractions and displacements acting over surfaces $\mathcal{S}_1$ and $\mathcal{S}_2$, respectively. Equation (3.18) is the starting point for the derivation of an approximate model of a cracked beam including shear deformations.

3.3 Kinematic Assumptions

The reduction of the 3-D elastic problem to a simplified, beam-like unidimensional system is achieved by the imposition of convenient kinematic assumptions on the stress, strain, and displacement fields. Figure 3.1 shows an example geometry of a cracked beam with a rectangular cross section. For zero body forces and linear momentum only in the x and z directions, the kinematic assumptions may be summarized as

$$
\begin{aligned}
u_x &= (-z + g(x,z))\psi(x,t) && \text{(3.19-a)}\\
u_y &= 0 && \text{(3.19-b)}\\
u_z &= w(x,t) && \text{(3.19-c)}\\
\epsilon_{xx}(x,z,t) &= (-z + f_1(x,z))S_1(x,t) && \text{(3.19-d)}\\
\epsilon_{xz}(x,z,t) &= f_2(x,z)S_2(x,t) && \text{(3.19-e)}\\
\epsilon_{yy} &= \epsilon_{zz} = -\nu\epsilon_{xx} && \text{(3.19-f)}\\
\epsilon_{xy} &= \epsilon_{yz} = 0 && \text{(3.19-g)}\\
\sigma_{xx}(x,z,t) &= (-z + f_1(x,z))T_1(x,t) && \text{(3.19-h)}\\
\sigma_{xz}(x,z,t) &= f_2(x,z)T_2(x,t) && \text{(3.19-i)}\\
\sigma_{yy} &= \sigma_{zz} = \sigma_{xy} = \sigma_{yz} = 0 && \text{(3.19-j)}\\
p_x &= P_x(x,t),\ p_y = 0,\ p_z = P_z(x,t) && \text{(3.19-k)}\\
B_x &= B_y = B_z = 0\ , && \text{(3.19-l)}
\end{aligned}
$$

where $T_1(x,t)$, $T_2(x,t)$, $S_1(x,t)$, and $S_2(x,t)$ are the unknown unidimensional stress and strain fields, respectively. The two displacement functions to be determined are the transverse displacement w and the cross section rotation ψ. The functions f_1 and f_2 are perturbation functions introduced to account for the stress/strain concentration in the cracked region.

3.3.1 Normal Stress/Strain Disturbance Function

For a rectangular cross section, the disturbance function acting in the normal stress and strain fields is assumed to have the form

$$f_1(x,z) = [z - m_1(z + \frac{a}{2})H(d-a-z)]\exp(-\alpha_1\frac{|x-x_c|}{d})\ . \tag{3.20}$$

Figure 3.2 depicts the distribution of the stress function. The normal stress disturbance function is similar to the one introduced by Shen in Ref. [101] and decays exponentially when we move away from the crack tip. It can be noticed that, in the absence of the crack,

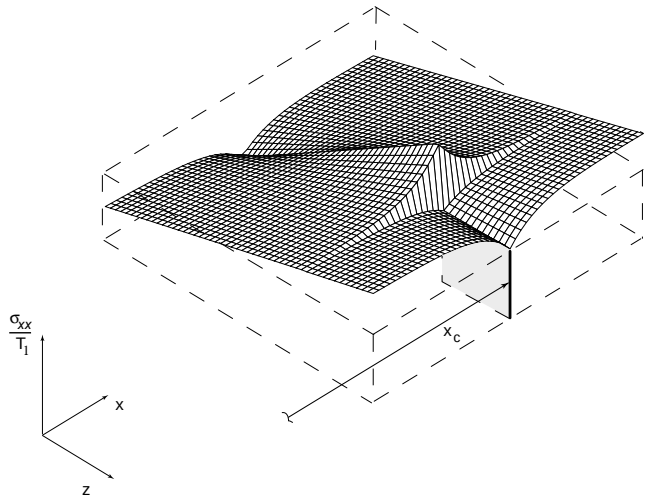

Figure 3.2: Crack function for normal stress disturbance f_1.

the usual linear distribution of stresses and/or strains trough the cross section is obtained. The zero stress condition along the crack faces is also met with the introduction of a Heaviside step function $H(.)$. The decay parameter α_1 was first obtained experimentally by Christides and Barr in Ref. [31] and further adjusted by Shen and Pierre in Ref. [101] by means of a bidimensional finite element model consisting of eight-noded quadrilateral elements with mid-side nodes repositioned to simulate the stress singularity at the crack tip. The identified value was then validated against experimental results.

3.3.2 Shear Stress/Strain Disturbance Function

Function f_2 is the newly introduced shear stress disturbance function which is based on an initially quadratic distribution of the shear stress and is given by

$$f_2(x,z) \;=\; f_0(z) \;+\; [-f_0(z) + m_2 f_r(z) H(d-a-z)] \exp(-\alpha_2 \frac{|x-x_c|}{d}) \;, \tag{3.21}$$

with

$$f_0(z) = 1 - \frac{z^2}{d^2} \tag{3.22}$$

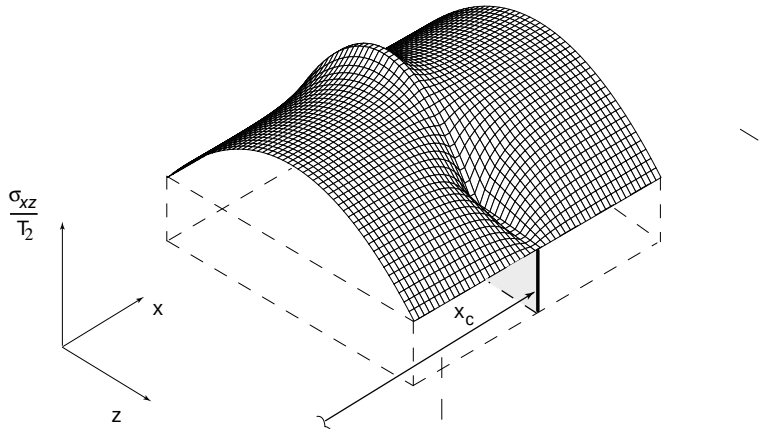

Figure 3.3: Crack function for shear stress disturbance f_2.

and

$$f_r(z) = -\frac{4(z-(d-a))(z+d)}{(a-2d)^2} \,. \tag{3.23}$$

Figure 3.3 illustrates the distribution of the shear stress/strain disturbance function. The same decay characteristics found in the normal stress function are assumed in a first approximation. It is worth noting that, in the absence of a crack, this is a representation of the shear distribution that is more refined than the typical Timoshenko model, which assumes constant shear stress over the cross section adjusted by shear correction factors. In fact, the typical shear correction factor used in Timoshenko models for rectangular cross sections (usually 5/6) is predicted exactly with this quadratic distribution. Constants m_1 and m_2 are computed from normal and shear force continuity conditions and are computed in Section (3.4.7).

3.3.3 Displacement Disturbance Function

Function g is introduced to account for the local variation in the neutral axis in the vicinity of the crack tip, as suggested in Ref. [101], and is kept in the formulation for the sake

completeness. It has a form very similar to the normal stress disturbance function, i.e.,

$$g(x,z) = [z - (z + \frac{a}{2})H(d-a-z)]\exp(-\beta\frac{|x-x_c|}{d}) \ . \tag{3.24}$$

The decay parameter β is obtained in Ref. [101] from a curve fitting to an expression of the form $\frac{1}{\sqrt{r}}$. The inclusion of g in two inconsistent kinematic assumptions in Ref. [101] has the undesired effect of generating a stiffness operator that is not self-adjoint, requiring further simplifications before numerical implementation. In addition, the steep nature of the terms involving g causes numerical difficulties, as discussed in Chapter 4.

3.4 Derivation of the Equations of Motion

The kinematic assumptions in Eq. (3.19) are substituted into Eq. (3.18), and the equations of motion and boundary conditions are obtained after several integrations by parts and convenient simplifications. We will derive the equations of motion for the general case of a single-edge crack, which includes the effects introduced by f_1, f_2, and g. The double-edge, symmetric crack model may be obtained from the final equations by means of the required simplifications and adequate changes in function f_1. The derivation process is described separately for each major term in Eq. (3.18) in the following sections.

3.4.1 Strain-Displacement Term

The strain–displacement term becomes

$$\int_V [\epsilon_{ij} - \frac{1}{2}(u_{i,j} + u_{j,i})]\delta\sigma_{ij}dV =$$

$$= \int_V \{[\epsilon_{xx} - \frac{\partial u_x}{\partial x}]\delta\sigma_{xx} + [\epsilon_{xz} - (\frac{\partial u_x}{\partial z} + \frac{\partial u_z}{\partial x})]\delta\sigma_{xz}\}dV =$$

$$= \int_V \{[(-z+f_1)S_1 - (-z+g)\frac{\partial\psi}{\partial x} - \frac{\partial g}{\partial x}\psi](-z+f_1)\delta T_1 + [f_2 S_2 - (-1+\frac{\partial g}{\partial z})\psi - w']f_2\delta T_2\}dV =$$

$$= \int_V \{[z^2 S_1 - 2zf_1S_1 + f_1^2 S_1 - z^2\psi' + zf_1\psi' + zg\psi' + zg'\psi - gf_1\psi' - g'f_1\psi]\delta T_1 +$$

$$+[f_2^2 S_2 + f_2\psi - f_2\frac{\partial g}{\partial z}\psi - f_2 w')]\delta T_2\}dV =$$
$$= \int_x \{[(I_0 - 2I_1 + I_2)S_1 - (I_0 - I_1 - I_6 + I_7)\psi' - (I_8 - I_6')\psi]\delta T_1$$
$$+[I_3 S_2 - (I_9 - I_4)\psi - w') - I_4 w']\delta T_2\}dx \ , \tag{3.25}$$

where the generalized cross section inertia integrals are defined in Eq. (3.42).

3.4.2 Stress-Strain Energy Density Term

The stress–strain term may be rewritten as

$$\int_V (\sigma_{ij} - W_{,\epsilon_{ij}})\delta\epsilon_{ij}dV =$$
$$= \int_V \{(\sigma_{xx} - W_{,\epsilon_{xx}})\delta\epsilon_{xx} + (\sigma_{xz} - W_{,\epsilon_{xz}})\delta\epsilon_{xz}\}dV \tag{3.26}$$

For isotropic, elastic beams, the strain energy function is expressed as

$$W = \frac{1}{2}\lambda\epsilon_{kk}\epsilon_{ii} + \mu\epsilon_{ij}\epsilon_{ij} \ ,$$

which leads to the derivatives

$$\frac{\partial W}{\partial \epsilon_{xx}} = E\epsilon_{xx} \ , \qquad \frac{\partial W}{\partial \epsilon_{xz}} = G\epsilon_{xz} \ . \tag{3.27}$$

Plugging (3.27) and (3.19) into (3.26) we get

$$\int_x \{(T_1 - ES_1)(I_0 - 2I_1 + I_2)\delta S_1 + (T_2 - GS_2)I_3\delta S_2\}dx \ . \tag{3.28}$$

3.4.3 Velocity-Momentum Term

The velocity-momentum term becomes

$$\int_V [\rho\dot{u}_i - (\frac{1}{2}\rho p_i p_i)_{,p_i}]\delta p_i dV =$$
$$\int_V \{[\rho(-z+g)\dot{\psi} - \rho P_x]\delta P_x + [\rho\dot{w} - \rho P_z]\delta P_z\}dV. \tag{3.29}$$

Since δP_x and δP_z are arbitrary in Eq. (3.29), we may conclude that

$$P_x = (-z+g)\dot{\psi} \ , \qquad P_z = \dot{w} \ . \tag{3.30}$$

3.4.4 Dynamic Equilibrium Term

The first term in Eq. (3.18) is the virtual work done by the dynamic forces. After substituting in Eqs. (3.19), it can be rewritten as

$$\int_V \{(\sigma_{ij,j} + B_i - \rho\dot{p}_i)\delta u_i\} dV =$$

$$\int_V \{[\frac{\partial \sigma_{xx}}{\partial x} + \frac{\partial \sigma_{xz}}{\partial z} - \rho\dot{P}_x](-z+g)\delta\psi + [\frac{\partial \sigma_{xz}}{\partial x} - \rho\dot{P}_z]\delta w\} dV =$$

$$= \int_V \{[-zT_1' + f_1T_1' + f_1'T_1 + \frac{\partial f_2}{\partial z}T_2 - \rho\dot{P}_x](-z+g)\delta\psi +$$

$$+ [f_2'T_2 + f_2T_2' - \rho\dot{P}_z]\delta w\} dV \ . \tag{3.31}$$

Plugging Eqs. (3.30) into Eq. (3.31), collecting terms, and integrating over the cross section, we get

$$\int_x \Big\{ [(I_0 - I_1 - I_6 + I_7)T_1' + (I_{10} - I_1')T_1 + (I_{11} - I_5)T_2 - (I_0 - 2I_6 + I_{12})\rho\ddot{\psi}]\delta\psi +$$

$$+ [I_4'T_2 + I_4T_2' - \rho A\ddot{w}]\delta w\} \, dx \ , \tag{3.32}$$

where the additional generalized inertia integrals are defined in Eq. (3.42).

3.4.5 Differential Equations of Motion

The equations of motion are derived by substituting the intermediate terms back into Eq.(3.18). Since all variations are considered independent, Eq. (3.18) only holds if all terms inside the brackets vanish. Therefore, since δT_1 and δT_2 are arbitrary, Eq. (3.25) implies

$$S_1 = \frac{(I_0 - I_1 - I_6 + I_7)}{(I_0 - 2I_1 + I_2)}\psi' + \frac{(I_8 - I_6')}{(I_0 - 2I_1 + I_2)}\psi \ , \tag{3.33}$$

and

$$S_2 = \frac{(I_9 - I_4)}{I_3}\psi + \frac{I_4}{I_3}w' \ . \tag{3.34}$$

Similarly, for arbitrary δS_1 and δS_2, Eq. (3.28) yields

$$T_1 = ES_1 \ , \qquad T_2 = GS_2 \ . \tag{3.35}$$

Performing all the necessary substitutions into Eq. (3.32), and taking into account Eqs. (3.34), (3.33), (3.35) and (3.30), we get the final expression

$$\int_x \Bigg\{ \Bigg[(I_0 - I_1 - I_6 + I_7) E \frac{\partial}{\partial x} \left(\frac{(I_0 - I_1 - I_6 + I_7)}{(I_0 - 2I_1 + I_2)} \psi' + \frac{(I_8 - I_6')}{(I_0 - 2I_1 + I_2)} \psi \right) +$$

$$(I_{10} - I_1') E \left(\frac{(I_0 - I_1 - I_6 + I_7)}{(I_0 - 2I_1 + I_2)} \psi' + \frac{(I_8 - I_6')}{(I_0 - 2I_1 + I_2)} \psi \right) +$$

$$(I_{11} - I_5) G \left(\frac{(I_9 - I_4)}{I_3} \psi + \frac{I_4}{I_3} w' \right) - (I_0 - 2I_6 + I_{12}) \rho \ddot{\psi} \Bigg] \delta\psi +$$

$$+ \left[I_4' G \left(\frac{(I_9 - I_4)}{I_3} \psi + \frac{I_4}{I_3} w' \right) + I_4 G \frac{\partial}{\partial x} \left(\frac{(I_9 - I_4)}{I_3} \psi + \frac{I_4}{I_3} w' \right) - \rho A \ddot{w} \right] \delta w \Bigg\} dx = 0$$

Now, since δw and $\delta\psi$ are arbitrary, we can finally write the two coupled partial differential equations of motion as

$$\frac{\partial}{\partial x}\left(\frac{I_4^2}{I_3} G(w' - \psi)\right) + \frac{\partial}{\partial x}\left(\frac{I_4 I_9}{I_3} G\psi\right) - \rho A \ddot{w} + q(x,t) = 0 \tag{3.36-a}$$

$$\frac{\partial}{\partial x}(E p_2(x) \psi') + E p_0(x) \psi + G \frac{I_4}{I_3}(I_{11} - I_5) w' - \rho (I_0 - 2I_6 + I_{12}) \ddot{\psi} = 0. \tag{3.36-b}$$

The coefficient functions in Eq.(3.36) are defined as

$$p_2(x) = (I_0 - I_1 - I_6 + I_7) Q_1(x) \tag{3.37}$$

$$p_0(x) = (I_0 - I_1 - I_6 + I_7) Q_2'(x) + (I_{10} - I_1') Q_2(x) + \frac{G}{E} Q_3(x) \quad , \tag{3.38}$$

with

$$Q_1(x) = \frac{(I_0 - I_1 - I_6 + I_7)}{(I_0 - 2I_1 + I_2)} \tag{3.39}$$

$$Q_2(x) = \frac{(I_8 - I_6')}{(I_0 - 2I_1 + I_2)} \tag{3.40}$$

$$Q_3(x) = \frac{(I_9 - I_4)(I_{11} - I_5)}{I_3} \, . \tag{3.41}$$

The generalized inertia integrals are obtained via integration over the cross section of different product combinations involving the crack perturbation functions, and are defined as

$$\begin{aligned}
I_0 &= \int_A z^2 dA \qquad & I_1 &= \int_A z f_1 dA \\
I_2 &= \int_A f_1^2 dA \qquad & I_3 &= \int_A f_2^2 dA \\
I_4 &= \int_A f_2 dA \qquad & I_5 &= \int_A z \frac{\partial f_2}{\partial z} dA \\
I_6 &= \int_A z g dA \qquad & I_7 &= \int_A f_1 g dA \\
I_8 &= \int_A f_1 g' dA \qquad & I_9 &= \int_A f_2 \frac{\partial g}{\partial z} dA \\
I_{10} &= \int_A f_1' g dA \qquad & I_{11} &= \int_A g \frac{\partial f_2}{\partial z} dA \\
I_{12} &= \int_A g^2 dA \ . & &
\end{aligned} \tag{3.42}$$

3.4.6 Boundary Conditions

Over the beam surface, tractions are given by $g_i = \sigma_{ij} n_j$, where n_j are the direction cosines of the external normals. The lateral surfaces of the beam ($z = \pm d$) are assumed to be traction-free, and the effects corresponding to the surface integral over that portion of $\mathcal{S}_1$ are assumed to be accounted for by the transverse load $q(x,t)$ introduced in Equations (3.36). The transversely applied load, as typical in beam theories, is considered a distributed force acting over the resulting unidimensional domain with no distinction between top or bottom surface, and it is a function of the axial coordinate x only.

The resulting unidimensional model still requires boundary conditions over the end surfaces ($x = 0$ and $x = L$) consistent with the derived equations of motion. If displacements are prescribed over the end surfaces, we can rewrite the integral over $\mathcal{S}_2$ as

$$\left[\int_A \left\{(u_x - \overline{u_x})\,\delta\sigma_{xx} + (u_z - \overline{u_z})\,\delta\sigma_{xz}\right\} dA\right]_{x=0}^{x=L}, \tag{3.43}$$

which, after substitutions, leads to

$$\left[\int_A \left\{(-z+g)(\psi - \overline{\psi})(-z+f_1)\delta T_1 + (w - \overline{w})\, f_2 \delta T_2\right\} dA\right]_{x=0}^{x=L} \tag{3.44}$$

Similarly, when tractions are prescribed over the end surfaces, the integral over $\mathcal{S}_1$ becomes

$$\left[\int_A \{(g_x - \overline{g_x})\delta u_x + (g_z - \overline{g_z})\delta u_z\}\, dA\right]_{x=0}^{x=L} \tag{3.45}$$

or

$$\left[\int_A \{((-z + f_1)T_1 - \overline{g_x})(-z + g)\delta\psi + (f_2 T_2 - \overline{g_z})\delta w\}\, dA\right]_{x=0}^{x=L} \tag{3.46}$$

For the typical homogeneous cases, i.e., either prescribed tractions or prescribed displacements equal to zero, Equations (3.44) and (3.46) lead to the boundary conditions over the end surfaces, which can be summarized, as:

$$E(I_0 - I_1 - I_6 + I_7)(Q_1\psi' + Q_2\psi) = 0, \tag{3.47-a}$$

$$\text{or} \qquad \psi = 0\ ; \tag{3.47-b}$$

and

$$GI_4\left(\frac{(I_9 - I_4)}{I_3}\psi + \frac{I_4}{I_3}w'\right) = 0, \tag{3.48-a}$$

$$\text{or} \qquad w = 0\ . \tag{3.48-b}$$

3.4.7 Calculation of Constants m_1 and m_2

The scaling constants in the expression for the crack disturbance functions may be obtained by the additional assumption that the presence of a crack does not introduce jumps in the bending moment and shear force along the axial direction. First, consider that the bending moment carried by the cracked section and by the correspondent uncracked section may be expressed as

$$\int_A (-zT_1(x_c, t)z dA = \int_{A_c} (-z + f_1(x_c, z))T_1(x_c, t)(z + a/2)dA\ , \tag{3.49}$$

where A_c is the cross section at $x = x_c$. At this section, we can write

$$f_1(x_c, z) = z - m_1(z + a/2). \tag{3.50}$$

Substituting Eq. (3.50) into Eq.(3.49) and integrating over the cross section we get

$$m_1 = \frac{I_0}{[I_r + (a/2)I_c]} \tag{3.51}$$

where

$$I_c = \int_{A_c} z dA \ , \qquad I_r = \int_{A_c} z^2 dA \tag{3.52}$$

are the first and second moment of area of the reduced section with respect to z with the origin kept at the centroid of the uncracked section.

Next, consider a similar expression relating the shear forces

$$\int_A f_0(z) T_2(x_c, t) dA = \int_A f_2(x_c, z) T_2(x_c, t) dA \ . \tag{3.53}$$

At $x = x_c$, we have

$$f_2(x_c, z) = m_2 f_r(z) \ , \tag{3.54}$$

which after plugging into Eq.(3.53) and integrating over the cross section, yields the expression for m_2

$$m_2 = \frac{2d}{2d - a} \ . \tag{3.55}$$

3.5 Symmetric Form and Check of Self-Adjointness

The solution of the equations of motion derived requires some sort of numerical discretization, which can be greatly simplified when the differential operator involved is self-adjoint. Once self-adjointness is guaranteed, the matrix representation after discretization will be symmetric and will benefit from the obvious computational advantages. The use of independent kinematic assumptions will not necessarily lead to a self-adjoint operator; in fact, certain conflicts in the assumptions may lead to an operator that is not self-adjoint and will require further simplifications before the numerical implementation, as can be seen in Ref.[101] and discussed in Appendix A. The objective of the present section is two-fold:

confirm the self-adjointness of the derived equations and, in the process, obtain the symmetric form that is most adequate for discretization and allows the utilization of test functions satisfying only the essential boundary conditions.

The self-adjointness is investigated following the approach in Inman, 1989 [59]. First, write the differential eigenvalue problem associated with Eqs.(3.36), (3.47), and (3.48). For zero external forces ($q(x,t) = 0$), assume that solutions for the free vibration problem are harmonic and separable in x and t

$$w(x,t) = W(x)F(t)\ , \qquad \psi = \Psi(x)F(t)\ , \tag{3.56}$$

with

$$\ddot{F}(t) = -\lambda F(t), \qquad \lambda = \omega^2\ . \tag{3.57}$$

To further simplify the notation, we write the resulting eigenvalue problem in the form

$$\mathcal{L}Y = \lambda \mathcal{M} Y\ , \tag{3.58}$$

where

$$Y(x) = [W(x)\ \Psi(x)]^T\ , \tag{3.59}$$

$$\mathcal{L} = -\begin{bmatrix} \mathcal{L}_{11} & \mathcal{L}_{12} \\ \mathcal{L}_{21} & \mathcal{L}_{22} \end{bmatrix}\ , \qquad \mathcal{M} = \begin{bmatrix} \mathcal{M}_{11} & 0 \\ 0 & \mathcal{M}_{22} \end{bmatrix}\ , \tag{3.60}$$

$$\mathcal{L}_{11} = \frac{\partial}{\partial x}(\frac{I_4^2}{I_3}G\frac{\partial(.)}{\partial x}) \qquad \mathcal{L}_{12} = \frac{\partial}{\partial x}(\frac{I_4}{I_3}(I_9 - I_4)G)$$
$$\mathcal{L}_{21} = \frac{I_4}{I_3}(I_{11} - I_5)G\frac{\partial}{\partial x} \qquad \mathcal{L}_{22} = \frac{\partial}{\partial x}(p_2(x)\frac{\partial}{\partial x}) + p_0(x) \tag{3.61}$$

$$\mathcal{M}_{11} = \rho A \qquad \mathcal{M}_{22} = \rho(I_0 - 2I_6 + I_{12})\ . \tag{3.62}$$

The inertia operator $\mathcal{M}$ is diagonal and does not involve any derivatives, which implies that it is implicitly self-adjoint and will be positive definite for positive values of $(I_0 - 2I_6 + I_{12})$, which is guaranteed by the definitions in Eqs.(3.42). The self-adjointness of the system will therefore depend on the properties of the stiffness operator.

An unbounded differential operator $\mathcal{L}$ with domain $D(\mathcal{L})$ has a formal *adjoint* operator $\mathcal{L}^*$ on domain $D(\mathcal{L}^*)$ defined by

$$< \mathcal{L}^* u, v >=< u, \mathcal{L}^* v >, \qquad u \in D(\mathcal{L}), \quad v \in D(\mathcal{L}^*), \tag{3.63}$$

where $< , >$ denotes the Lebesgue integral inner product. The differential operator is said to be *self-adjoint* if $D(\mathcal{L}) = D(\mathcal{L}^*)$ and $\mathcal{L}^* u = \mathcal{L} u$, for all $u \in D(\mathcal{L})$. Therefore, for the stiffness operator in Eqn.3.58, one must show that for any two comparison functions U and V the following relation holds

$$\int_0^L U^T \mathcal{L} V dx = \int_0^L V^T \mathcal{L} U dx \ , \tag{3.64}$$

and U and V are in the same domain. This relation can be demonstrated by developing the right-hand side integral until getting a term that is symmetric with respect to U and V when the same boundary conditions apply to U and V. Writing the first integral in Eq.(3.64) in terms of its components, we get

$$\int_0^L U^T \mathcal{L} V dx = -\int_0^L \{U_W \ \ U_\Psi\} \begin{bmatrix} \mathcal{L}_{11} & \mathcal{L}_{12} \\ \mathcal{L}_{21} & \mathcal{L}_{22} \end{bmatrix} \begin{Bmatrix} V_W \\ V_\Psi \end{Bmatrix} dx =$$

$$= -\int_0^L \{U_W \mathcal{L}_{11} V_W + U_W \mathcal{L}_{12} V_\Psi + U_\Psi \mathcal{L}_{21} V_W + U_\Psi \mathcal{L}_{22} V_\Psi\} \, dx \ . \tag{3.65}$$

First, analyze terms involving the diagonal components in operator $\mathcal{L}$. The term involving $\mathcal{L}_{11}$ can be integrated by parts, yielding

$$\int_0^L U_W \frac{\partial}{\partial x} \left(\frac{I_4^2}{I_3} G \frac{\partial (V_W)}{\partial x} \right) dx = U_W \frac{I_4^2}{I_3} G \frac{\partial (V_W)}{\partial x} \bigg|_0^L - \int_0^L \frac{\partial (U_W)}{\partial x} \frac{I_4^2}{I_3} G \frac{\partial (V_W)}{\partial x} dx \ . \tag{3.66}$$

Similarly, taking into account the definitions in Eqs.(3.37) through (3.41), the term in $\mathcal{L}_{22}$ can be modified through integration by parts as

$$\int_0^L \left[U_\Psi \frac{\partial}{\partial x} (p_2 V'_\Psi) + U_\Psi p_0 V_\Psi \right] dx =$$

$$= U_\Psi E(I_0 - I_1 - I_6 + I_7) \left(Q_1 V'_\Psi + Q_2 V_\Psi \right) \big|_0^L +$$

$$- \int_0^L U'_\Psi E(I_0 - I_1 - I_6 + I_7)\left(Q_1 V'_\Psi + Q_2 V_\Psi\right) dx +$$

$$- \int_0^L U_\Psi E\left[(I_8 - I'_6)(Q_1 V'_\Psi + Q_2 V_\Psi)\right] dx + \int_0^L \left[U_\Psi G Q_3 V_\Psi\right] dx. \tag{3.67}$$

Using the fact that

$$(I_8 - I'_6)Q_1 = (I_0 - I_1 - I_6 + I_7)Q_2 \ , \tag{3.68}$$

the integral terms in Eq.(3.67) can be further simplified to

$$U_\Psi E(I_0 - I_1 - I_6 + I_7)\left(Q_1 V'_\Psi + Q_2 V_\Psi\right)\Big|_0^L - \int_0^L U'_\Psi E(I_0 - I_1 - I_6 + I_7) Q_1 V'_\Psi dx +$$

$$- \int_0^L (U'_\Psi V_\Psi + U_\Psi V'_\Psi) E(I_8 - I'_6) Q_2 dx + \int_0^L U_\Psi [G Q_3 - E(I_8 - I'_6) Q_2] V_\Psi dx. \tag{3.69}$$

Next, address the off-diagonal terms. Through integration by parts, the term in $\mathcal{L}_{12}$ can be rewritten as

$$\begin{aligned} \int_0^L U_W \frac{\partial}{\partial x}\left(\frac{I_4}{I_3}(I_9 - I_4) G V_\Psi\right) dx \;\; &= \;\; U_W \frac{I_4}{I_3}(I_9 - I_4) G V_\Psi \Big|_0^L + \\ &\quad - \int_0^L \frac{\partial (U_W)}{\partial x} \frac{I_4}{I_3}(I_9 - I_4) G V_\Psi dx \ . \end{aligned} \tag{3.70}$$

The term in $\mathcal{L}_{21}$ is left in its original form as

$$\int_0^L U_\Psi \frac{I_4}{I_3}(I_{11} - I_5) G \frac{\partial (V_W)}{\partial x} dx. \tag{3.71}$$

Both equations (3.66) and (3.69) are indeed symmetric forms in U and V. The boundary term in Eq.(3.69) has the same form as the derived natural boundary condition in Eq.(3.47). The boundary terms in Eq.(3.66) and (3.70) combined also match the natural boundary condition in Eq. (3.48). Therefore, the boundary terms vanish provided that U and V satisfy the same boundary conditions, which in turn implies $D(\mathcal{L}) = D(\mathcal{L}^*)$. The only remaining terms are the integrals in Eqs.(3.70) and (3.71). which also combine into a symmetric form provided that

$$(I_{11} - I_5) = -(I_9 - I_4) \ , \tag{3.72}$$

which will now be verified. From Eq.(3.31), the terms that originate $(I_{11} - I_5)$ may be rewritten as

$$\begin{aligned}\int_x (I_{11} - I_5) T_2 \delta\psi dx &= \int_V [(-z+g)\frac{\partial f_2}{\partial z}] T_2 \delta\psi dV = \\ &= \int_x \int_y \left\{ T_2 \delta\psi \int_z (-z+g)\frac{\partial f_2}{\partial z} dz \right\} dxdy, \end{aligned} \tag{3.73}$$

where T_2 and $\delta\psi$ are functions of x only. Integrating by parts with respect to z yields

$$\int_x \int_y \left\{ T_2 \delta\psi \left[(-z+g) f_2 |_{-d}^{d} - \int_z (-1 + \frac{\partial g}{\partial z}) f_2 dz \right] \right\} dxdy =$$

$$= \int_x \int_y \left\{ T_2 \delta\psi \left[(-z+g) f_2 |_{-d}^{d} \right] \right\} dxdy - \int_x (I_9 - I_4) f_2 T_2 \delta\psi dx. \tag{3.74}$$

Since f_2 vanishes at the edges $z = \pm d$, the first term in Eq.(3.74) is equal to zero and therefore Eq. (3.72) holds.

This concludes the check of self-adjointness of the differential operator. The derived symmetric form including the natural boundary conditions permits less strict requirements for the test functions, which now can be chosen from the space of admissible functions, i.e., satisfying only the geometric (essential) boundary conditions.

3.6 Euler-Bernoulli Cracked Beam Model Revisited

In this section, we present the basic assumptions and the main results in the derivation of the equations of motion of cracked Euler-Bernoulli beams developed by Shen and co-workers [100, 101, 98, 99]. The goal of the present summary is to provide reference for the key equations implemented in Chapter 4 and used for comparison with the new model proposed in Sections (3.3) and (3.4). The details of the derivation are omitted, but all the intermediate steps are well described in [100].

3.6.1 Kinematic Assumptions

The basic kinematic assumptions can be summarized as

$$
\begin{aligned}
u_x' &= (-z + g(x,z))w''(x,t) && \text{(3.75-a)}\\
u_y &= 0 && \text{(3.75-b)}\\
u_z &= w(x,t) && \text{(3.75-c)}\\
\epsilon_{xx} &= (-z + f_1(x,z))S_1(x,t) && \text{(3.75-d)}\\
\epsilon_{yy} &= \epsilon_{zz} = -\nu\epsilon_{xx} && \text{(3.75-e)}\\
\epsilon_{xy} &= \epsilon_{yz} = \epsilon_{xz} = 0 && \text{(3.75-f)}\\
\sigma_{xx} &= (-z + f_1(x,z))T_1(x,t) && \text{(3.75-g)}\\
\sigma_{xz} &= \sigma_{xz}(x,z,t) && \text{(3.75-h)}\\
\sigma_{yy} &= \sigma_{zz} = \sigma_{xy} = \sigma_{yz} = 0 && \text{(3.75-i)}\\
p_x &= 0,\ p_y = 0,\ p_z = P_z(x,t) && \text{(3.75-j)}\\
B_x &= B_y = B_z = 0. && \text{(3.75-k)}
\end{aligned}
$$

Although shear effects are not considered, the component σ_{xz} is included by Shen to provide mathematical consistency in the treatment of transverse loading. A very important fact should be pointed out regarding Shen's assumptions: it is the *first derivative* of the axial displacement, u_x', that is assumed to be disturbed by the crack function. However, throughout the variational process, the first variation of the axial displacement is taken as

$$\delta u_x = (-z + g)\delta w' \,, \tag{3.76}$$

which presumes

$$u_x = (-z + g)w' \,, \tag{3.77}$$

which in turn would lead to

$$u_x' = (-z + g)w'' + g'w' \,. \tag{3.78}$$

This apparently minor inconsistency is believed to be the cause of mathematical problems discussed later.

3.6.2 Equations of Motion

Plugging Eqs. (3.75) and (3.76) into (3.18) and going through all the intermediate mathematical steps yields the partial differential equation of motion for free vibrations

$$E(I_0 - I_1 - I_6 + I_7)Q_1 w^{(iv)} + E[2(I_0 - I_1 - I_6 + I_7)Q_1' + (2I_{10} + I_8 - I_6' - 2I_1')Q_1]w''' +$$

$$+E[(I_0 - I_1 - I_6 + I_7)Q_1'' + (2I_{10} + I_8 - I_6' - 2I_1')Q_1' + (I_{10}' - I_1'')Q_1]w'' + \rho A\ddot{w} = 0, \quad (3.79)$$

where the definitions in Eqs.(3.39) and (3.42) still apply.

3.6.3 Boundary Conditions

At the ends of the beam, Shen concludes that the relations to be satisfied for zero prescribed forces and/or displacements are

$$\begin{aligned} E(I_0 - I_1 - I_6 + I_7)Q_1 w'' &= 0, \\ \text{or} \qquad w' &= 0\ ; \end{aligned} \quad (3.80)$$

and

$$\begin{aligned} E[(I_0 - I_1 - I_6 + I_7)(Q_1' w'' + Q_1 w''') + E(I_{10} - I_1')Q_1 w'' &= 0, \\ \text{or} \qquad w &= 0\ . \end{aligned} \quad (3.81)$$

3.6.4 Comments on Shen's Model

There are undeniable merits in Shen's work as the first to address the problem of deriving a continuous model of a cracked beam with a single edge crack. However, a few remarks are in order.

- The stiffness operator in Eq. (3.79) is *not* self-adjoint, as demonstrated in Appendix A. This will generate a stiffness matrix which may be non symmetric, leading to complex eigenvalues that are incompatible with the conservative physical nature of the problem when no damping is present;

- The numerical implementations presented in Ref. [100] are preceded by simplifications which render the stiffness matrix symmetric. The details of these simplifications are neither shown nor referenced in the article;

- The displacement disturbance function g has a very steep nature, which may cause problems in the numerical implementation, as discussed in Chapter 4. In addition, the procedure proposed in [100] for the estimation of the decay parameter β leads to a value that is implicitly dependent on the step of numerical integration, also an undesired characteristic.

3.6.5 Proposed Modification

In order to overcome the limitations found in Shen's model, a modified version of the equation of motion and boundary conditions is proposed. The kinematic assumptions, Eqs. (3.75), are modified to include Eq. (3.77) replacing Eq. (3.75-a) and hence Eqs. (3.76) and (3.78) will now both hold. Only the final equations are presented here, and the details of the derivation are found in Appendix A.

Equation of Motion

The variational process is carried out as usual and the final form of the equation is

$$E(I_0 - I_1 - I_6 + I_7)Q_1 w^{(iv)} + E[(I_0 - I_1 - I_6 + I_7)(2Q_1' + Q_2) + (2I_{10} + I_8 - I_6' - 2I_1')Q_1]w''' +$$

$$+E[(I_0 - I_1 - I_6 + I_7)(Q_1'' + 2Q_2') + (2I_{10} + I_8 - I_6' - 2I_1')(Q_1' + Q_2) + (I_{10}' - I_1'')Q_1]w''$$

$$E[(I_0 - I_1 - I_6 + I_7)Q_2'' + (2I_{10} + I_8 - I_6' - 2I_1')Q_2' + (I_{10}' - I_1'')Q_2]w' + \rho A\ddot{w} = 0, \quad (3.82)$$

which is now self-adjoint and can be rewritten in a more convenient form as

$$E[p_2(x)w(x,t)'']'' + E[p_1(x)w'(x,t))]' + \rho A\ddot{w}(x,t) = 0, \tag{3.83}$$

with p_2 as defined in Equation (3.37) and

$$p_1(x) = E[(I_0 - I_1 - I_6 + I_7)Q_2' + (I_{10}' - I_1'')Q_2] \,. \tag{3.84}$$

Boundary Conditions

The boundary conditions that result from the variational derivation now are expressed as

$$E(I_0 - I_1 - I_6 + I_7)(Q_1 w'' + Q_2 w') = 0 \tag{3.85-a}$$

$$\text{or} \qquad w' = 0 \tag{3.85-b}$$

and

$$E(I_0 - I_1 - I_6 + I_7)(Q_1 w''' + (Q_1' + Q_2)w'' + Q_2' w') + $$

$$+ \; E(I_{10} - I_1')(Q_1 w'' + Q_2 w') = 0 \tag{3.86-a}$$

$$\text{or} \qquad w = 0 \,. \tag{3.86-b}$$

This completes the review of the Euler-Bernoulli models implemented in Chapter 4 and concludes the chapter on mathematical formulation.

Chapter 4

Numerical Implementation

4.1 Introduction

The solution of Eqns. (3.36) or the Euler–Bernoulli models discussed in Chapter 3 requires a numerical discretization in order to reduce the partial differential equations to a set of ordinary differential equations. The Galerkin method discussed here is an attractive option especially when dealing with dynamic systems involving damping. Previous publications by Banks and co-workers show that the approach is very efficient when damping parameters need to be estimated [115], which is often the case in practical applications of model updating, even for undamaged structures. Detection of small geometric defects was also demonstrated successfully with this numerical technique [12]. Finally, proofs of well-posedness and existence of solutions for inverse problems involving second order operators with general damping using spline-based discretizations are available in the literature [13] and they provide the necessary mathematical background for the present work and its possible future extensions.

4.2 Galerkin Discretization Using B-Splines

In order to discretize the equations of motion in Eqn. (3.36), we first consider the undamped case. The introduction of damping is discussed in Section 4.4.2. Rewrite the equations of motion in the general operator form,

$$\mathcal{M}u + \mathcal{L}u = \{Q\} \,, \tag{4.1}$$

with $u = \{w \;\; \psi\}^T$ and $\{Q\} = \{q \;\; 0\}^T$. Assume an N-dimensional, separable series approximation for the components of u given by

$$\begin{aligned} w(x,t) &\simeq w^N(x,t) = \sum_{i=1}^{N} \phi_i(x)\zeta_i(t), \\ \psi(x,t) &\simeq \psi^N(x,t) = \sum_{i=1}^{N} \varphi_i(x)\eta_i(t), \end{aligned} \tag{4.2}$$

where $\phi_i(x)$ and $\varphi_i(x)$ are admissible functions chosen from an appropriate function space. In matrix form, we may write

$$\{u\}^N = [\Phi]\,\{y\}, \tag{4.3}$$

with

$$\{y\} = \{\zeta_1, \zeta_2, ... \, \zeta_N \; \eta_1, \eta_2 ... \eta_N\}^T \,, \tag{4.4}$$

$$[\Phi] = \begin{bmatrix} [\phi] & [0] \\ [0] & [\varphi] \end{bmatrix}_{2\times 2N} \,, \tag{4.5}$$

$$[\phi] = [\phi_1, \phi_2, ..., \phi_N] \,, \tag{4.6}$$

$$[\varphi] = [\varphi_1, \varphi_N, ..., \varphi_N] \,. \tag{4.7}$$

Recalling that the stiffness and mass operators have dimension 2×2, we plug Eq. (4.3) into (4.1), pre-multiply by $[\Phi]^T$ and integrate over the domain to obtain

$$[M]\,\{\ddot{y}\} + [K]\,\{y\} = \{F\}, \tag{4.8}$$

where the resulting mass and stiffness matrices are defined respectively by

$$[M] = \int_0^L [\Phi]^T \, \mathcal{M} \, [\Phi] \, dx \,,$$

$$[K] = \int_0^L [\Phi]^T \mathcal{L} [\Phi] \, dx \ ,$$

and the forcing vector in the discretized space is

$$\{F\} = \int_0^L [\Phi]^T \{Q\} dx \ .$$

The test functions are chosen from the space defined by the span of $\{\hat{b}_i\}_{i=1}^{\hat{N}+3}$, the standard cubic B-splines locally defined over a uniform $\hat{N}$-partition of the unidimensional domain representing the beam. The relationship between $\hat{N}$ and N depends on the boundary conditions to be imposed, with $N = \hat{N} + 3$ corresponding to the free-free case. For all other boundary conditions, the admissible functions are chosen from a subspace of $\{\hat{b}_i\}$ obtained by the appropriate linear combinations of the basis of standard splines. The polynomial definition of the spline functions and the construction of subspaces corresponding to the imposition of boundary conditions are discussed in Appendix B.

Equation (4.8) is the desired discretized version of the equations of motion in Eqn. (3.36) and can now be used in the numerical calculations for model validation and for the computation of time responses needed for the identification procedure.

4.3 Model Validation

4.3.1 Convergence Study

As a first validation of the numerical model implemented, a convergence study is performed by analyzing simply supported beams with aspect ratios $L/2d = 5$ and $L/2d = 20$. The depth of a crack introduced at midspan is increased up to 50% of the beam cross section depth. The natural frequencies are then evaluated for different levels of discretization, i.e., different number of test functions included in the Galerkin approximation. Figure 4.1 illustrates the percent variation of the first four natural frequencies of the long and short undamaged beams, when modeled both by the Euler model, Eq. (3.83), and the "Timoshenko" model,

Eqs. (3.36). In each case, the reference for comparison is the corresponding value obtained using 100 test functions, which was found to be a good estimate of the converged values for all practical purposes. As expected, a relatively small number of test functions is needed for very good convergence of the results in all undamaged cases. As can be noticed, discretization with about 20 test functions is sufficient to produce results within 0.01% of the reference ("converged") values for all natural frequencies.

When a crack is introduced, the minimum number of test functions required for the same level of relative precision increases as the crack depth increases. Figures 4.2 to 4.4 depict the percent variations of the first four natural frequencies of the beams with different crack depth ratios for both models and aspect ratios. The relatively better convergency rates for modes 2 and 4 when compared to modes 1 and 3 can be explained by the fact that the corresponding natural frequencies of the former are very little affected by the presence of a crack, since the midspan point is a modal node of those modes. In general, the clear link between precision and crack depth in the most affected modes can be explained by a careful exam of the nature of the crack disturbance functions discussed in Chapter 3. It can be noticed that the exponential decay characteristics of those functions are not affected by the crack depth variable, but the strength of the concentration on the stress fields, given by parameters m_1 and m_2, are inversely proportional to the crack length a. The region around the crack tip affected by the disturbance functions is therefore larger for deeper cracks, requiring a better discretization to be accurately captured.

Another important aspect can be inferred from Figures 4.2 to 4.4 when comparing the results from the short and slender beams; the convergence is somewhat slower for the long beam, which can be easily explained by looking at the actual size of the subdomain of each test function ("element"). Since the element size is uniform and directly proportional to the length of the beam, this means that for the same value of N the crack tip neighborhood is better represented, i.e., it has a more refined discretization in the shorter beam. To confirm that this is in fact the most relevant parameter that explains the differences, we further compare the results using a normalized discretization index N^*, which is taken equal to N for

the short beam and equal to $N/4$ for the long beam, assuring that for a given N^* the element length in both beams will be the same. Figure 4.2 shows that the normalized convergence plots are in fact very similar for all cases. This indicates that a possible implementation of nonuniform spline discretizations, suggested as future work, can potentially increase the precision of the proposed model without the burden of increasing the size of the matrices in the model.

Another useful comparison can be made by plotting curves of natural frequency versus crack length for different levels of discretization, as shown in Figures 4.6 and 4.7. These plots provide an indication of the accuracy of the models when damage severity is increased. It is apparent that the curves are well characterized with 20 and 50 test functions for the short and slender beams, respectively. The larger differences to the converged curves always occur when deeper cracks are present, and once again the Timoshenko models offer less accurate results than the Euler model with the same level of discretization, especially for the slender beam. In summary, Figures 4.2 to 4.7 indicate that for the same precision level, the Timoshenko model consistently requires a higher level of discretization than the Euler model, which can be considered a numerical disadvantage of the proposed model. This is however clearly compensated by the increased accuracy in the actual values of the natural frequencies, as discussed in later sections.

Finally, as a by-product of the convergency studies, Figures 4.2 to 4.7 can provide estimates of the required level of discretization for a desired level of precision. For instance, a discretization with $N = 30$ can provide results within 0.5% accuracy for crack length ratios up to 40% and within 1% up to 50%. This is particularly important when using such models in the time-domain damage detection scheme proposed in Chapter 5, where the numerical costs involved can be reduced by using a model with the minimum acceptable size.

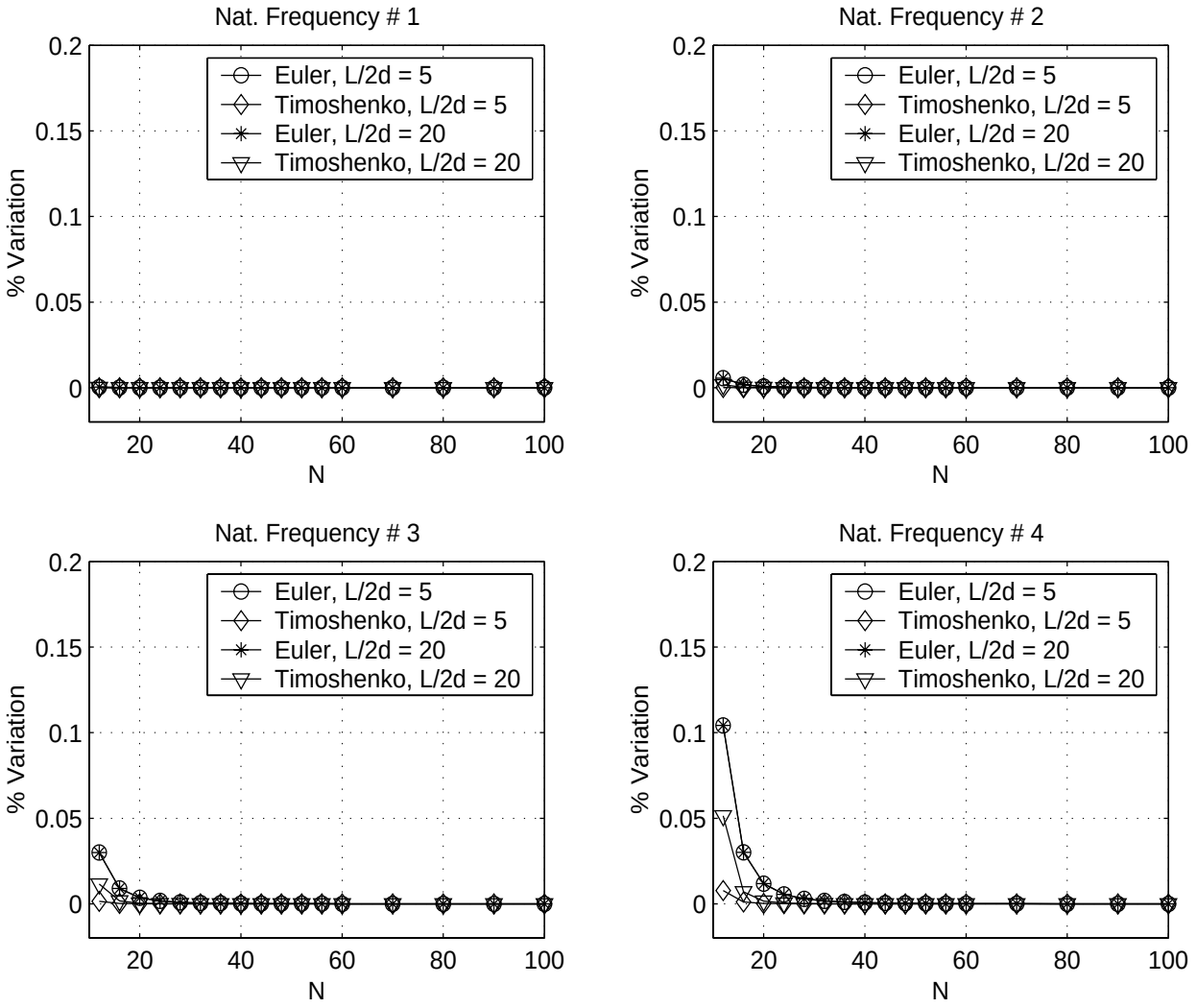

Figure 4.1: Comparison of convergence characteristics of the Euler and Timoshenko models for undamaged short and slender simply supported beams.

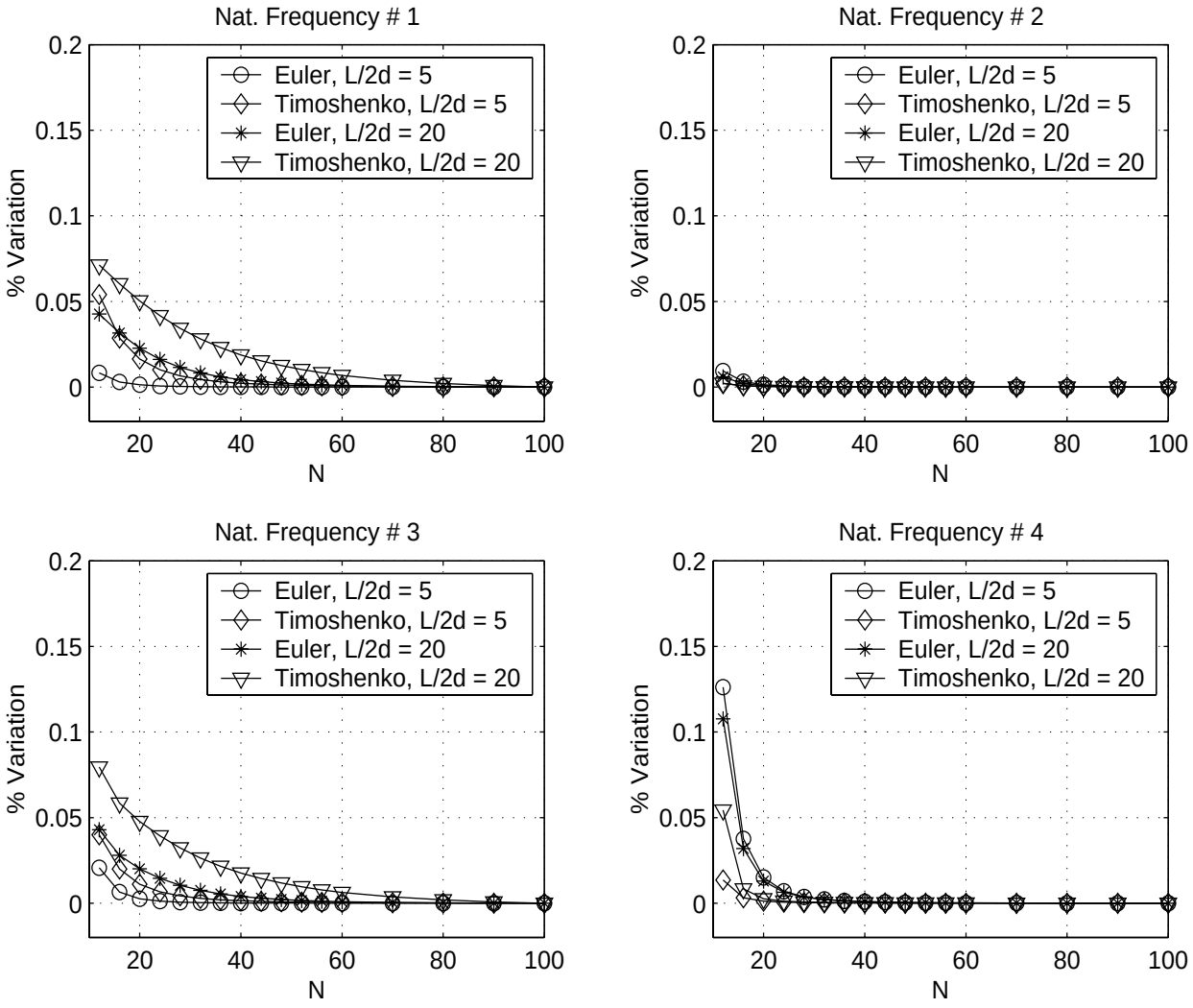

Figure 4.2: Comparison of convergence characteristics of the Euler and Timoshenko cracked beam models. Crack depth ratio $a/2d = 0.1$.

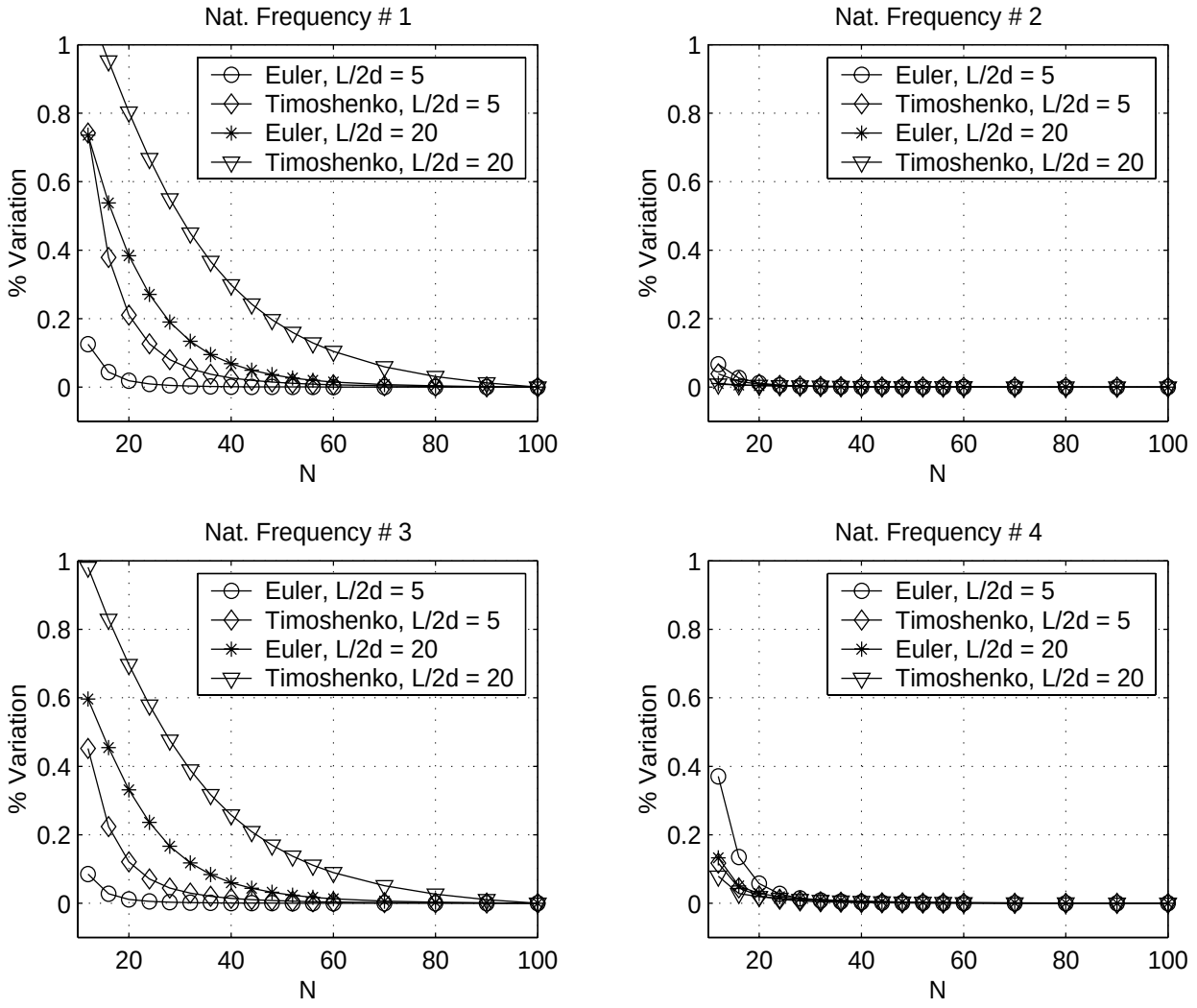

Figure 4.3: Comparison of convergence characteristics of the Euler and Timoshenko cracked beam models. Crack depth ratio $a/2d = 0.3$.

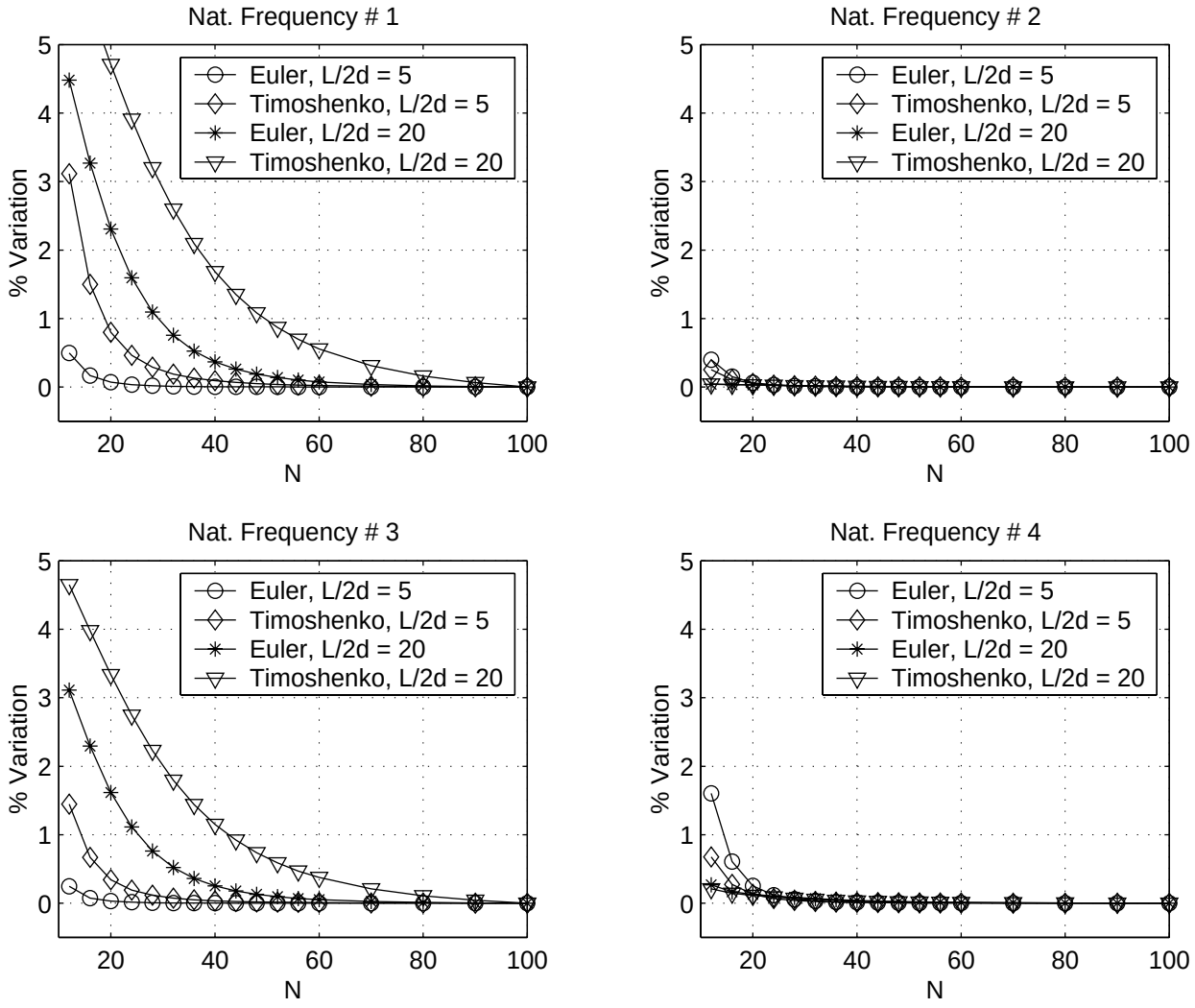

Figure 4.4: Comparison of convergence characteristics of the Euler and Timoshenko cracked beam models. Crack depth ratio $a/2d = 0.5$.

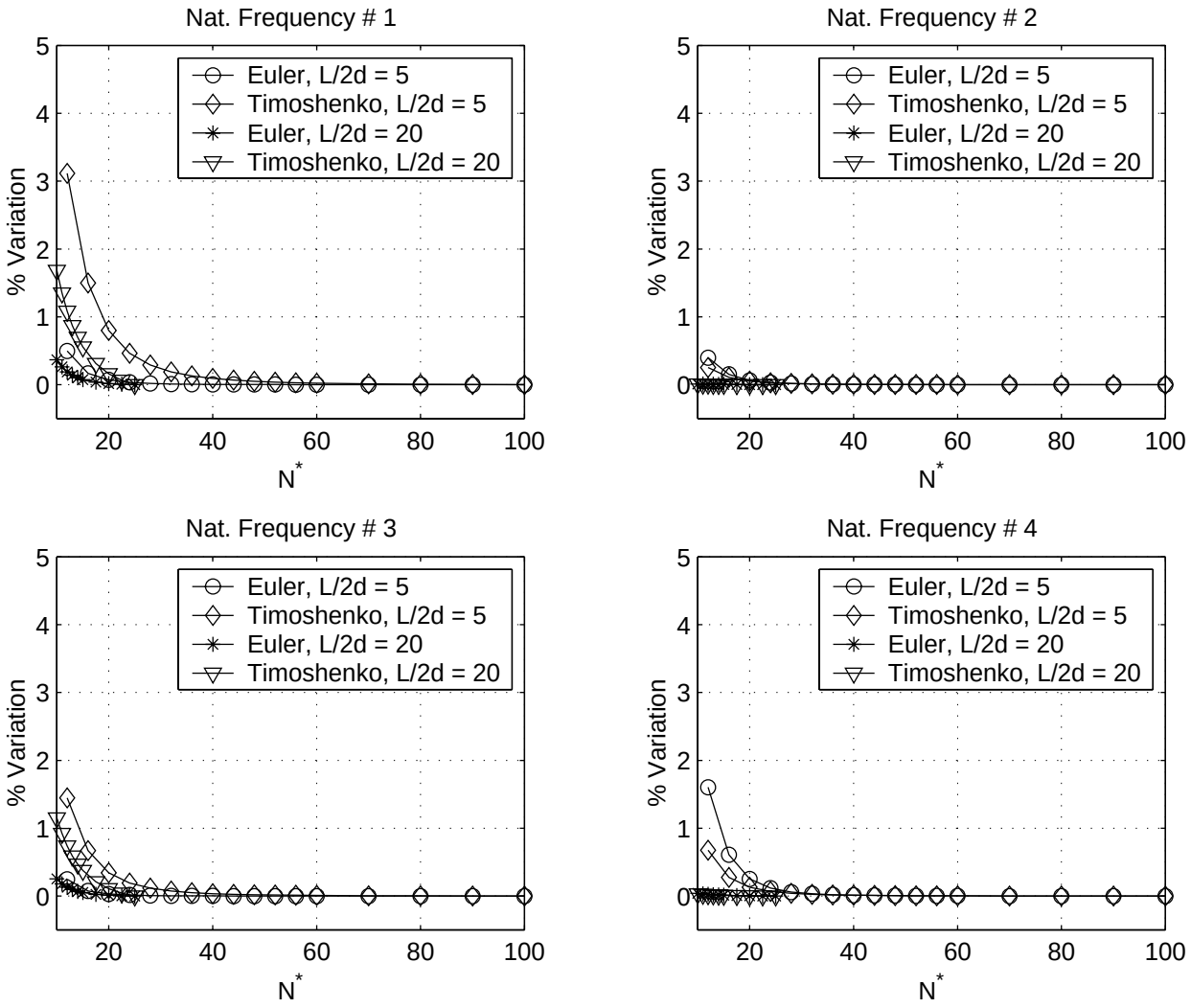

Figure 4.5: Comparison of convergence characteristics of the Euler and Timoshenko cracked beam models. Curves normalized to the same element length. Crack depth ratio $a/2d = 0.5$.

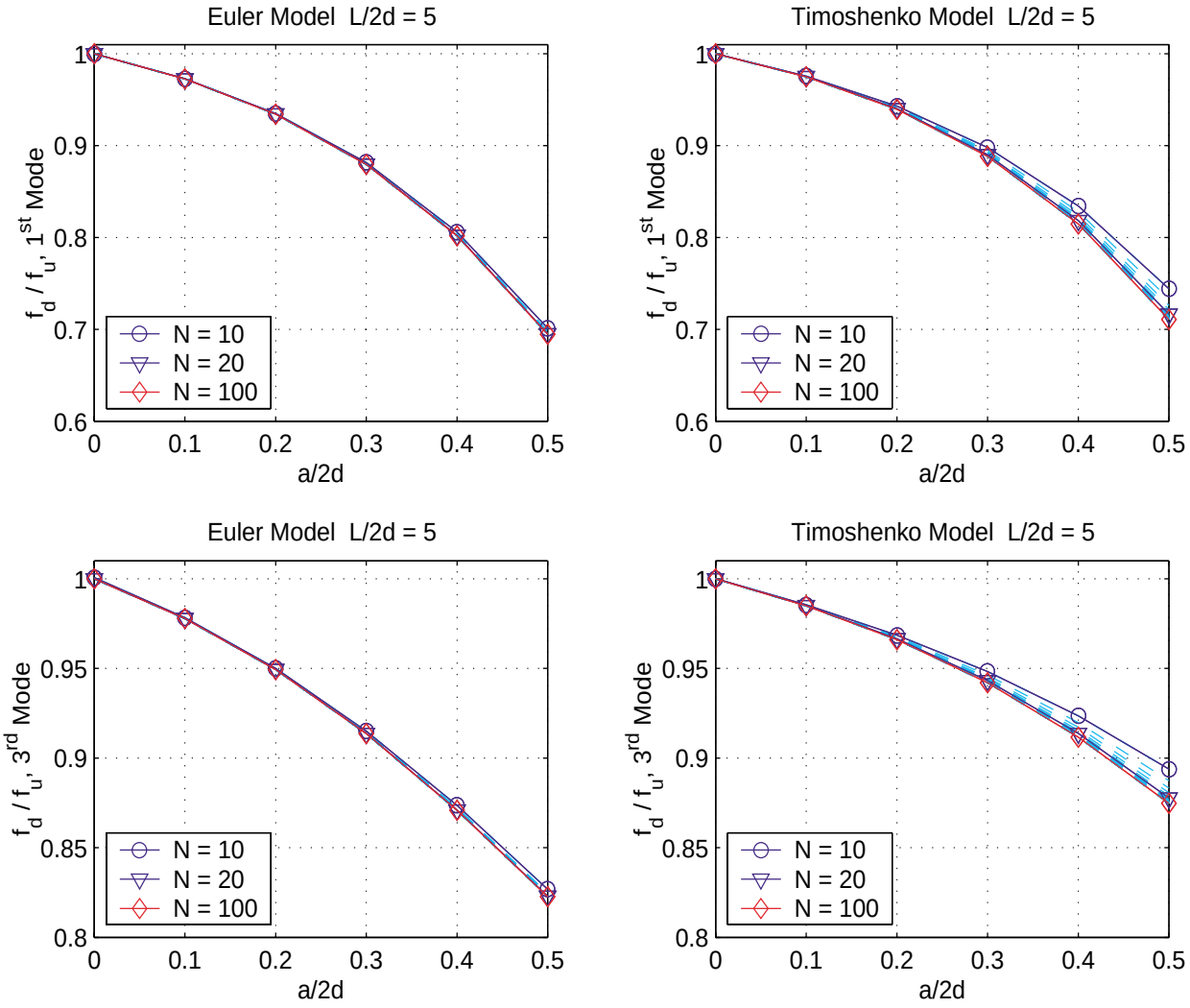

Figure 4.6: Variations of natural frequencies due to increase in crack depth for different levels of discretization of a short, simply-supported beam, $L/2d = 5$.

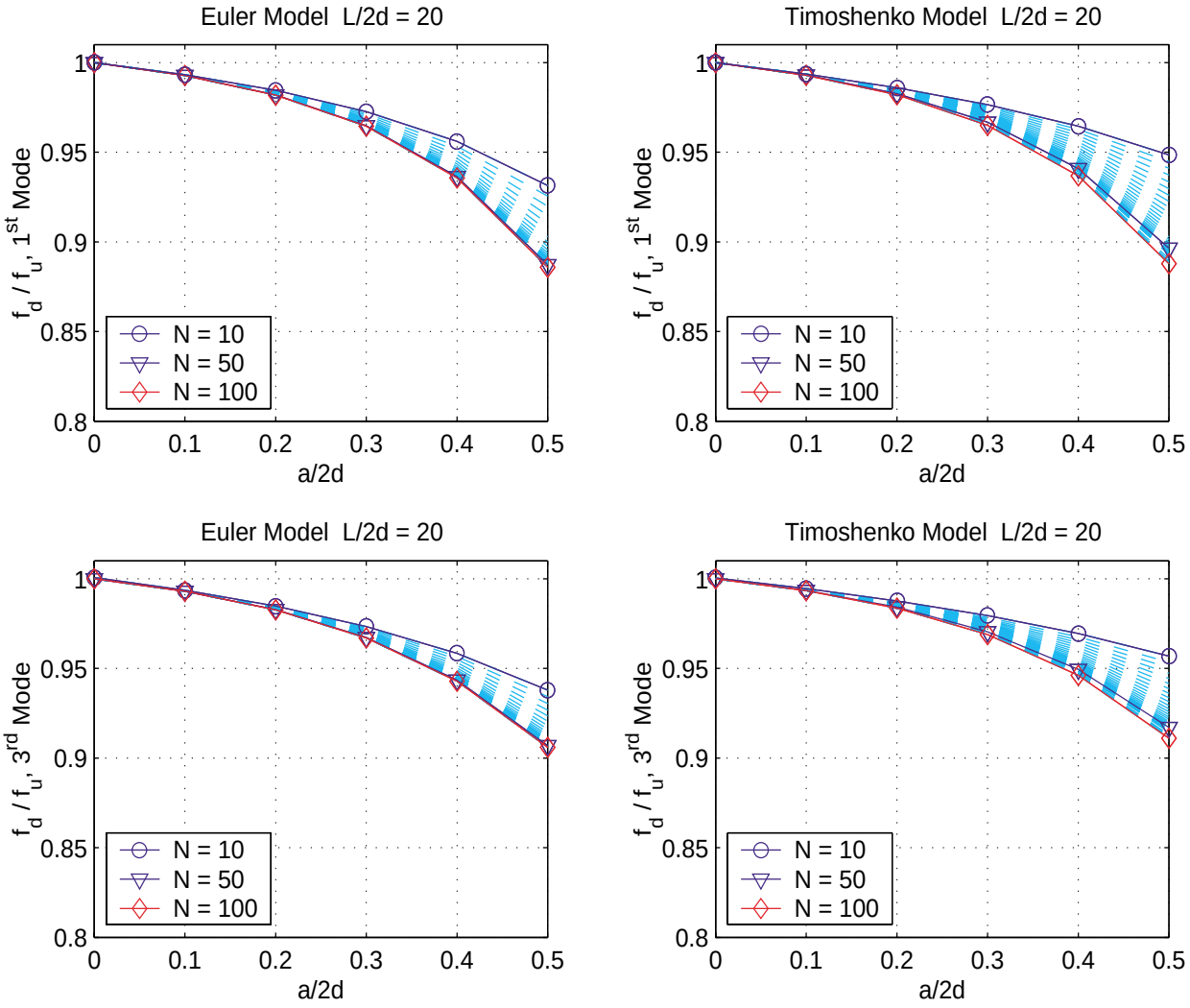

Figure 4.7: Variations of natural frequencies due to increase in crack depth for different levels of discretization of a slender, simply-supported beam, $L/2d = 20$.

4.3.2 Effects of Displacement Disturbance Function $g(x, z)$

The inclusion of the displacement disturbance function $g(x, z)$ as suggested by Shen and Pierre in [101] causes the mathematical problems discussed in Chapter 3, more specifically the lack of self-adjointness of the derived stiffness operator. A possible correction of this mathematical inconsistency was discussed in Section 3.6.5, but the inclusion of the displacement function still implies in higher numerical demands due to the computation of terms involving a very steep function, consequently requiring very small integration steps.

In order to assess the effect of the displacement function on the quality of the model, a series of simulations with and without the inclusion of $g(x, z)$ was investigated, using the same cantilever beam example in [100]. The numerical integrations of the terms in the stiffness matrix are performed using the MATLAB high order quadrature function QUAD8, with relative error set to its default value, 1e-3, recommended for most cases. This function is basically an adaptive integration routine, which automatically refines the integration step based on precision requirements. The same calculations are then repeated with a more refined precision, now set at 1e-7, and the results for different crack locations are summarized in Figures 4.8 to 4.10. It is apparent that with the new precision settings the results with and without g are identical for any practical purposes. More importantly, they are in very good agreement with the results obtained with the lower precision settings when the displacement functions is not included, which indicates that the only effect of the inclusion of function $g(x, z)$ is the need for a more refined integration procedure, with no apparent advantages to the quality of the model. In fact, the more refined precision in the presented simulations increase the integration time by a factor of two or more, which implies in a extremely high price to pay to avoid the occasional numerical imprecisions depicted in Figures 4.8 to 4.10. In short, inclusion of $g(x, z)$ introduces very small contributions to the model at an unreasonable numerical price. Based on these numerical experiments, the effect of the displacement disturbance function $g(x, z)$ was disregarded in the remaining calculations.

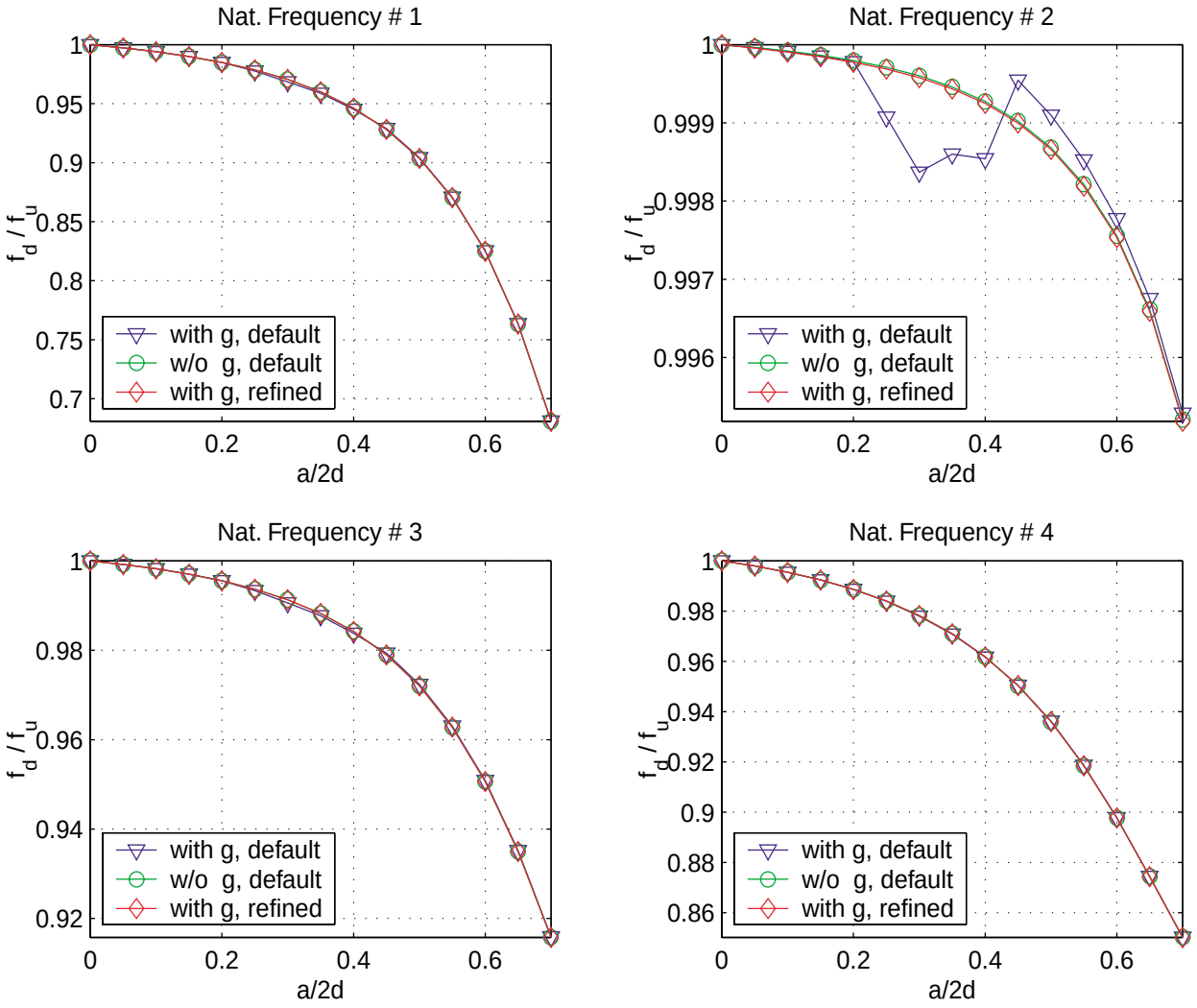

Figure 4.8: Influence of displacement disturbance function g on the natural frequencies of a simply supported slender beam, $L/2d = 24.65$, $x_c/L = 0.2$.

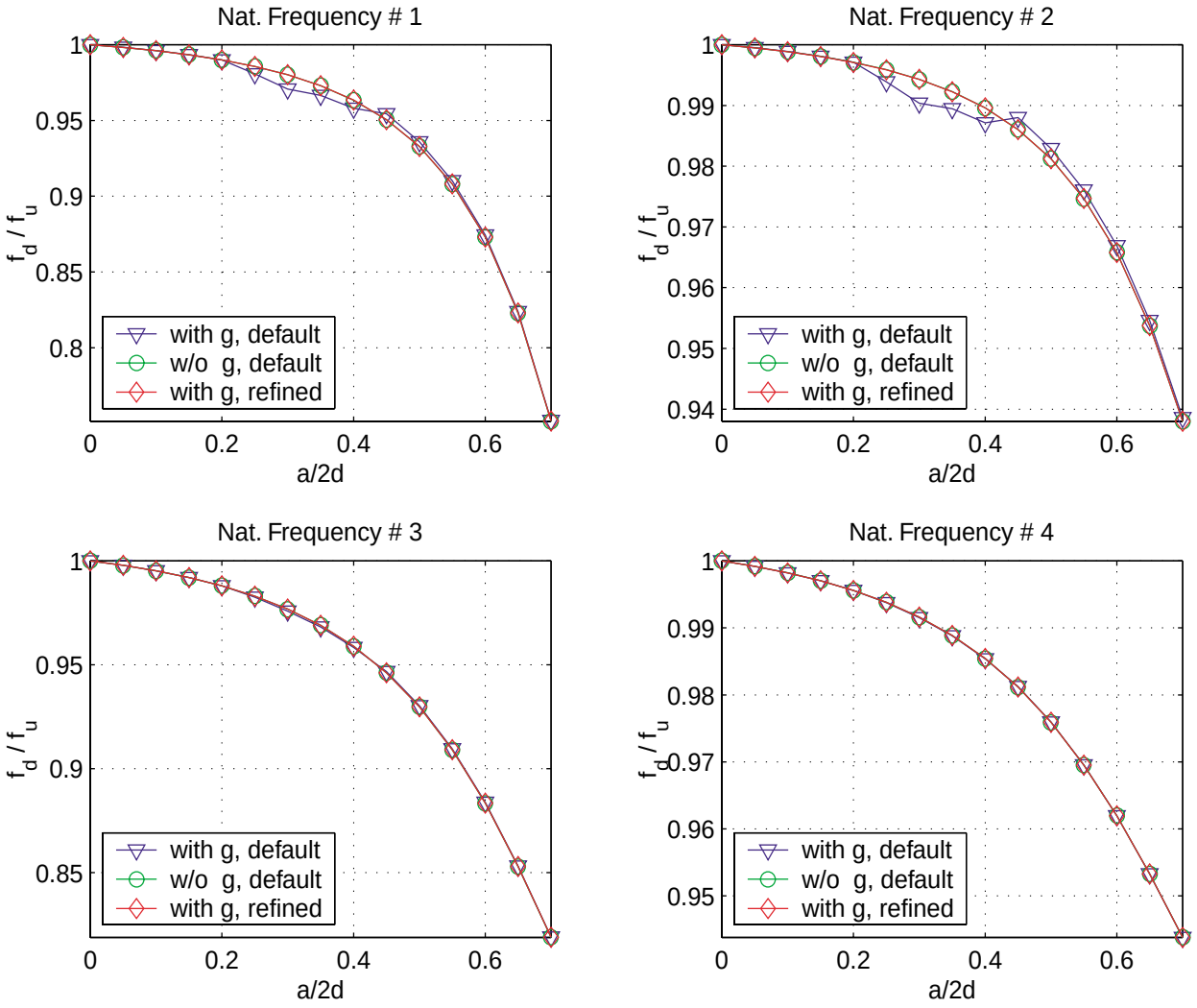

Figure 4.9: Influence of displacement disturbance function g on the natural frequencies of a simply supported slender beam, $L/2d = 24.65$, $x_c/L = 0.3$.

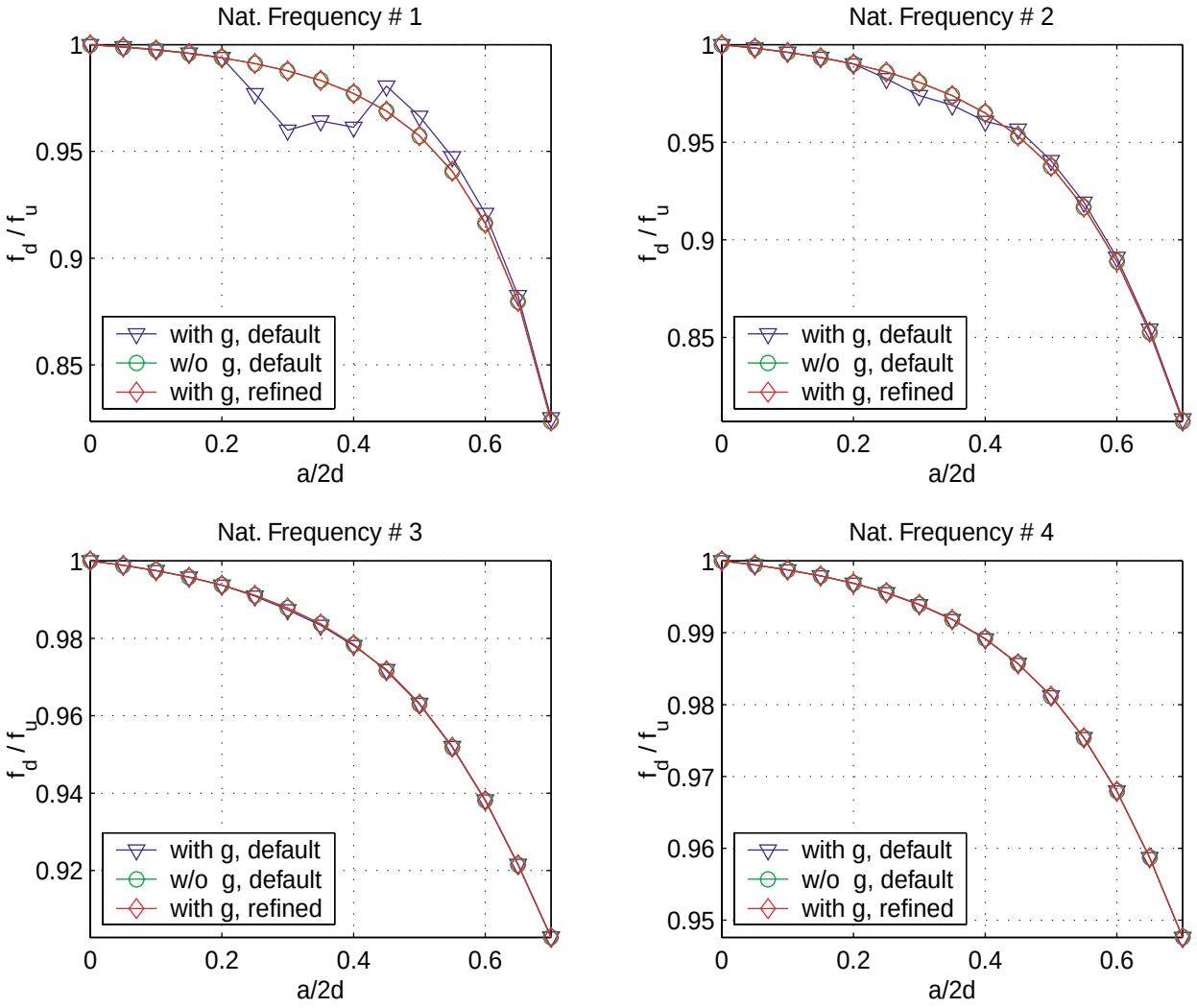

Figure 4.10: Influence of displacement disturbance function g on the natural frequencies of a simply supported slender beam, $L/2d = 24.65$, $x_c/L = 0.4$.

4.3.3 Influence of Aspect Ratio

An important investigation to characterize the potential advantages of the Timoshenko model versus the Euler model is the study of the influence of aspect ratio on the natural frequencies. This effect is well reported in the literature for the case of uniform (undamaged) beams, and we produce here similar comparisons taking into account the effect of the presence of a crack of different depths.

Table 4.1 presents natural frequencies for the first four modes of cracked beams with the maximum and minimum aspect ratios investigated in this study, with both pinned-pinned and clamped-free boundary conditions. The differences increase significantly for the short beam, becoming as high as 95% for the fourth mode with the larger crack depth. Figure 4.11 summarizes the evolution of the differences of the two models when the aspect ratio is continuously decreased. Two important conclusions can be drawn from that figure: first, the differences are larger for the higher modes for all crack depths, which is intuitive and was somewhat expected; and second, the curves for different crack depths, including zero depth (undamaged case) are clearly of the same general trend and are clustered for each natural frequency, which means that the cracked models maintain the same relative merits of the Timoshenko over the Euler formulation as in the uniform beam case.

Another aspect to be analyzed is the variation of the normalized natural frequencies used as damage indicator in many proposed model-based frequency-domain health monitoring methods. One of the main advantages of this normalization is that the absolute values of the natural frequencies are strongly dependent on the accuracy of the model, whereas the normalized relative changes (damaged frequency divided by the correspondent undamaged value) are fairly insensitive to modelling errors. To check whether the Timoshenko model has any advantage over the Euler model when normalized values are used, Figure 4.12 depicts the natural frequency vs. crack length curves for the first four modes of two simply supported cracked beams of different aspect ratios for both the Timoshenko and the Euler models; some selected numerical values are presented in Table 4.2. The curves are almost

coincident for the slender beam, but they show significant differences for the short beam. The curve for the third and fourth natural frequencies are illustrative of a key characteristic, namely the relatively "nonconservative" prediction of the Euler model. Indeed, for the same change in natural frequency, the Euler model underestimates the correspondent crack length when compared to the Timoshenko model, which could lead to significant errors in a frequency domain crack detection procedure. Figure 4.13 depicts the variation of natural frequencies with the crack position for a given crack depth. As expected, the influences are less accentuated at the nodes of the mode shapes and close to the simple supports. The relevant information is the pronounced differences in the predictions of the two models for the short beam. In this case, for a known crack depth, the same change in natural frequencies would lead to very discrepant crack locations depending on the model used.

The last investigation related to aspect ratio is on the influence of the presence of a crack on the mode shapes, which are included as damage indicators in some of the methods found in the literature. As discussed in Chapter 2, the extremely localized changes introduced in the mode shapes by the presence of a crack would require either *a priori* knowledge of the possible damaged site or a large number of sensors installed over the structure, which is clearly confirmed by mode shape investigations for slender beams published in Ref. [100] . The proposed model can be used to assess whether or not the same localized changes occur in short beams. Figure 4.14 shows the variations in the first three displacement modes for a long and a short beam. It is apparent that, although more evident than in the slender beam, the same localized characteristics are present in the short beam, which confirms the expected little advantage of the use of mode shapes in damage detection methods. Another proposed alternative found in the literature is the use of curvature mode shapes or strain mode shapes, both directly related to the rotational mode shapes depicted in Figure 4.15, which certainly show larger changes for a crack of 50% of the beam depth, but still not sufficient for any practical use in crack diagnosis.

Table 4.1: Differences in natural frequencies computed with both cracked beam models (reference: undamaged value obtained via Timoshenko model).

Simply Supported Slender Beam ($L/2d = 20, x_c/L = 0.5$)									
	$a/2d = 0.0$			$a/2d = 0.1$			$a/2d = 0.5$		
	Euler	Timo.	diff %	Euler	Timo.	Diff %	Euler	Timo.	Diff %
f_1	1.00422	1.00000	0.42	0.99702	0.99299	0.41	0.89102	0.89649	-0.61
f_2	1.01670	1.00000	1.67	1.01665	0.99986	1.68	1.01572	0.99869	1.71
f_3	1.03694	1.00000	3.69	1.02970	0.99348	3.65	0.94051	0.91711	2.55
f_4	1.06422	1.00000	6.42	1.06400	0.99952	6.45	1.06029	0.99528	6.53
Simply Supported Short Beam ($L/2d = 4, x_c/L = 0.5$)									
	$a/2d = 0.0$			$a/2d = 0.1$			$a/2d = 0.5$		
	Euler	Timo.	diff %	Euler	Timo.	Diff %	Euler	Timo.	Diff %
f_1	1.09770	1.00000	9.77	1.06132	0.97069	9.34	0.72075	0.68165	5.74
f_2	1.33144	1.00000	33.14	1.32482	0.99239	33.50	1.21910	0.92048	32.44
f_3	1.62927	1.00000	62.93	1.58770	0.98385	61.38	1.31627	0.87447	50.52
f_4	1.95928	1.00000	95.93	1.93819	0.98939	95.90	1.66459	0.90297	84.35
Cantilever Slender Beam ($L/2d = 20, x_c/L = 0.2$)									
	$a/2d = 0.0$			$a/2d = 0.1$			$a/2d = 0.5$		
	Euler	Timo.	diff %	Euler	Timo.	Diff %	Euler	Timo.	Diff %
f_1	1.00199	1.00000	0.20	0.99441	0.99257	0.19	0.88410	0.89151	-0.83
f_2	1.01380	1.00000	1.38	1.01368	0.99981	1.39	1.01182	0.99792	1.39
f_3	1.03241	1.00000	3.24	1.03008	0.99773	3.24	0.99727	0.96867	2.95
f_4	1.05874	1.00000	5.87	1.05267	0.99482	5.82	0.97965	0.93591	4.67
Cantilever Short Beam ($L/2d = 4, x_c/L = 0.2$)									
	$a/2d = 0.0$			$a/2d = 0.1$			$a/2d = 0.5$		
	Euler	Timo.	diff %	Euler	Timo.	Diff %	Euler	Timo.	Diff %
f_1	1.04806	1.00000	4.81	1.01006	0.96531	4.64	0.67028	0.65198	2.81
f_2	1.29837	1.00000	29.84	1.29138	0.99137	30.26	1.18923	0.92029	29.22
f_3	1.58784	1.00000	58.78	1.56702	0.98834	58.55	1.35039	0.90749	48.80
f_4	1.93265	1.00000	93.26	1.89364	0.98954	91.37	1.62767	0.92773	75.45

Table 4.2: Changes in normalized natural frequencies for selected crack depth ratios (reference: undamaged value from the same model).

Simply Supported Slender Beam ($L/2d = 20, x_c/L = 0.5$)									
	$a/2d = 0.1$			$a/2d = 0.3$			$a/2d = 0.5$		
	Euler	Timo.	diff %	Euler	Timo.	Diff %	Euler	Timo.	Diff %
f_1	0.99283	0.99299	-0.02	0.96481	0.96676	-0.20	0.88727	0.89649	-1.03
f_2	0.99995	0.99986	0.01	0.99973	0.99952	0.02	0.99903	0.99869	0.03
f_3	0.99301	0.99348	-0.05	0.96725	0.97038	-0.32	0.90700	0.91711	-1.10
f_4	0.99979	0.99952	0.03	0.99896	0.99829	0.07	0.99630	0.99528	0.10
Simply Supported Short Beam ($L/2d = 4, x_c/L = 0.5$)									
	$a/2d = 0.1$			$a/2d = 0.3$			$a/2d = 0.5$		
	Euler	Timo.	diff %	Euler	Timo.	Diff %	Euler	Timo.	Diff %
f_1	0.96686	0.97069	-0.39	0.85750	0.87216	-1.68	0.65660	0.68165	-3.68
f_2	0.99503	0.99239	0.27	0.97501	0.97109	0.40	0.91563	0.92048	-0.53
f_3	0.97449	0.98385	-0.95	0.90390	0.94104	-3.95	0.80789	0.87447	-7.61
f_4	0.98923	0.98939	-0.02	0.94853	0.96150	-1.35	0.84959	0.90297	-5.91
Cantilever Slender Beam ($L/2d = 20, x_c/L = 0.2$)									
	$a/2d = 0.1$			$a/2d = 0.3$			$a/2d = 0.5$		
	Euler	Timo.	diff %	Euler	Timo.	Diff %	Euler	Timo.	Diff %
f_1	0.99244	0.99257	-0.01	0.96300	0.96491	-0.20	0.88234	0.89151	-1.03
f_2	0.99988	0.99981	0.01	0.99940	0.99926	0.01	0.99805	0.99792	0.01
f_3	0.99774	0.99773	0.00	0.98903	0.98953	-0.05	0.96596	0.96867	-0.28
f_4	0.99427	0.99482	-0.06	0.97323	0.97665	-0.35	0.92530	0.93591	-1.13
Cantilever Short Beam ($L/2d = 4, x_c/L = 0.2$)									
	$a/2d = 0.1$			$a/2d = 0.3$			$a/2d = 0.5$		
	Euler	Timo.	diff %	Euler	Timo.	Diff %	Euler	Timo.	Diff %
f_1	0.96374	0.96531	-0.16	0.84661	0.85358	-0.82	0.63954	0.65198	-1.91
f_2	0.99461	0.99137	0.33	0.97390	0.96940	0.46	0.91594	0.92029	-0.47
f_3	0.98689	0.98834	-0.15	0.94200	0.95859	-1.73	0.85046	0.90749	-6.28
f_4	0.97982	0.98954	-0.98	0.92361	0.96562	-4.35	0.84219	0.92773	-9.22

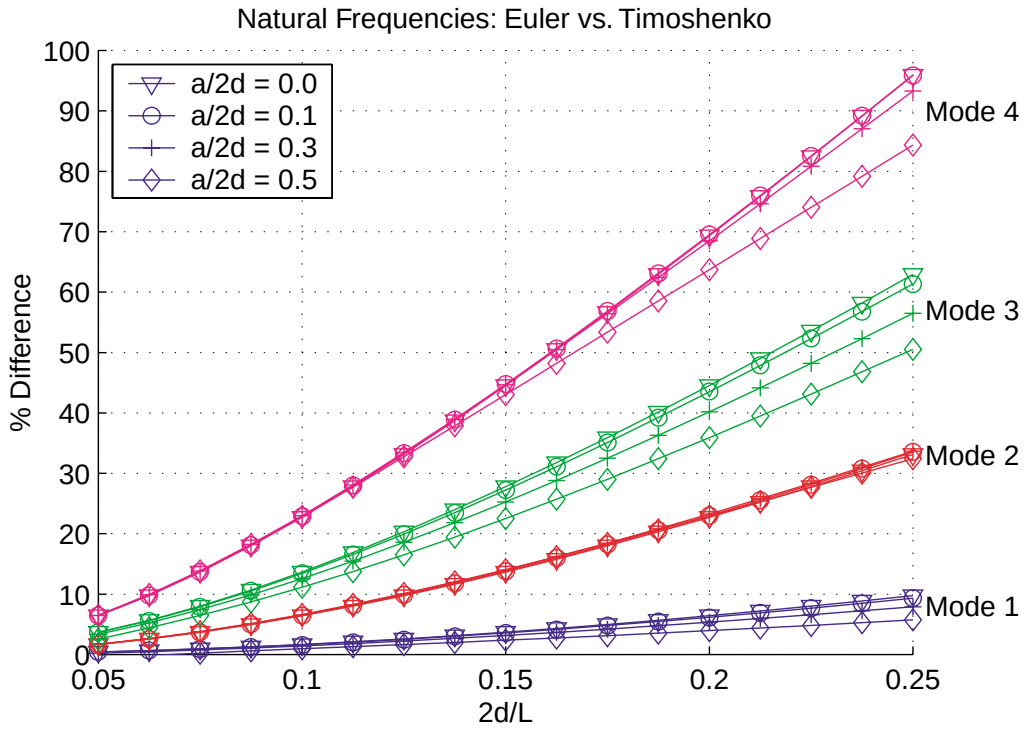

Figure 4.11: Differences in natural frequencies estimated by Euler and Timoshenko models as a function of aspect ratio for a simply supported beam with a midspan crack.

4.3.4 Comparison with data from literature

The validations and investigations performed so far were mainly based on relative comparisons between the Timoshenko and Euler model. In order to further evaluate the quality of the proposed model, comparisons with refined finite element models as well as experimental data from the literature are presented and discussed.

The first example is the simply supported beam with rectangular cross section described in Ref. [101]. Figures 4.16 and 4.17 depict the variation of the first three natural frequencies as a function of crack depth for both models, along with results of the finite element model used as reference. The FE model was implemented in [101] to estimate the value of the decay parameter α, and it consists of a typical 2–D discretization with eight-noded, quadrilateral elements with the midside nodes repositioned at 1/4 of the length along the crack interface

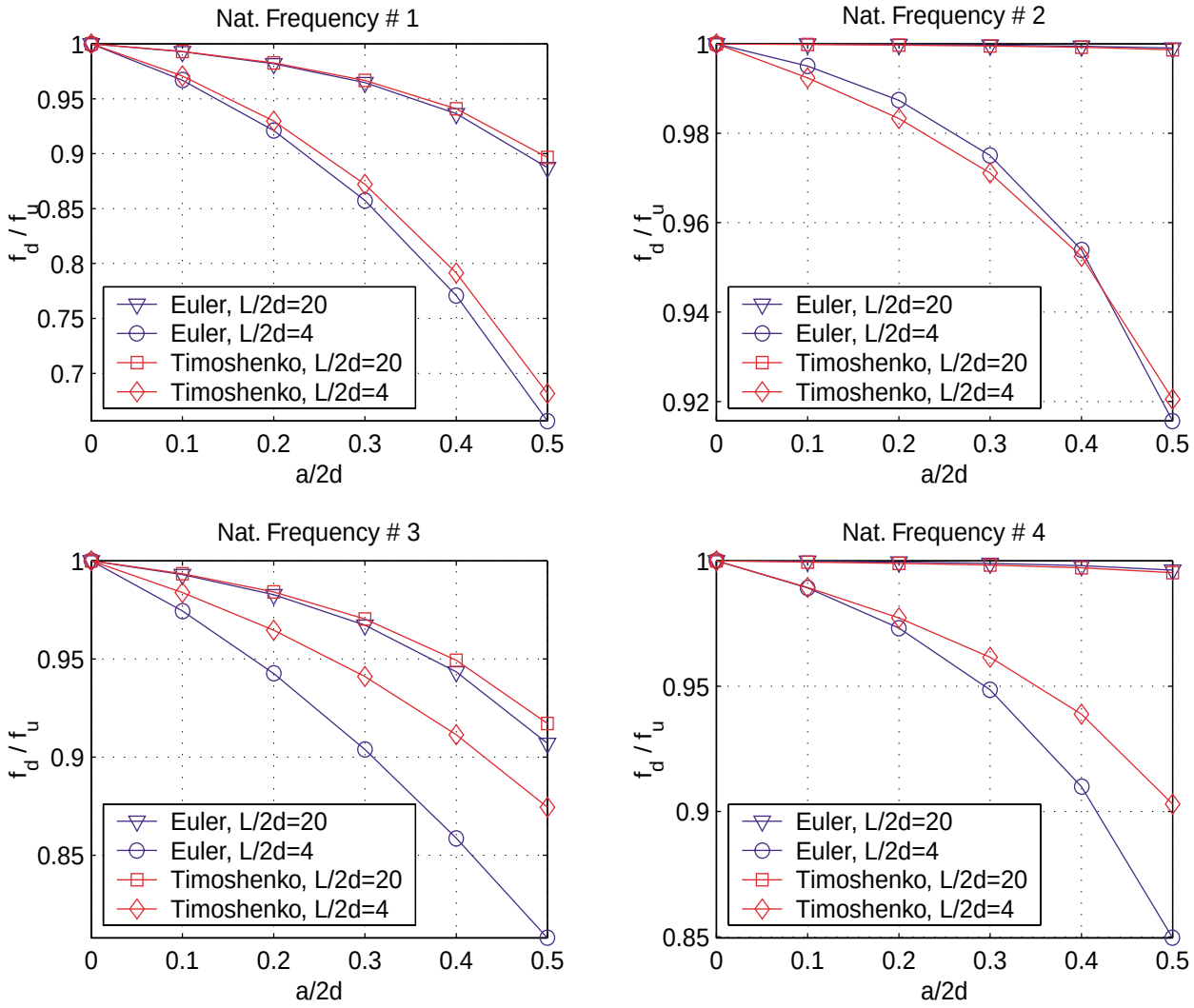

Figure 4.12: Variation of normalized natural frequencies of simply supported beams with respect to crack depth. $x_c/L = 0.5$.

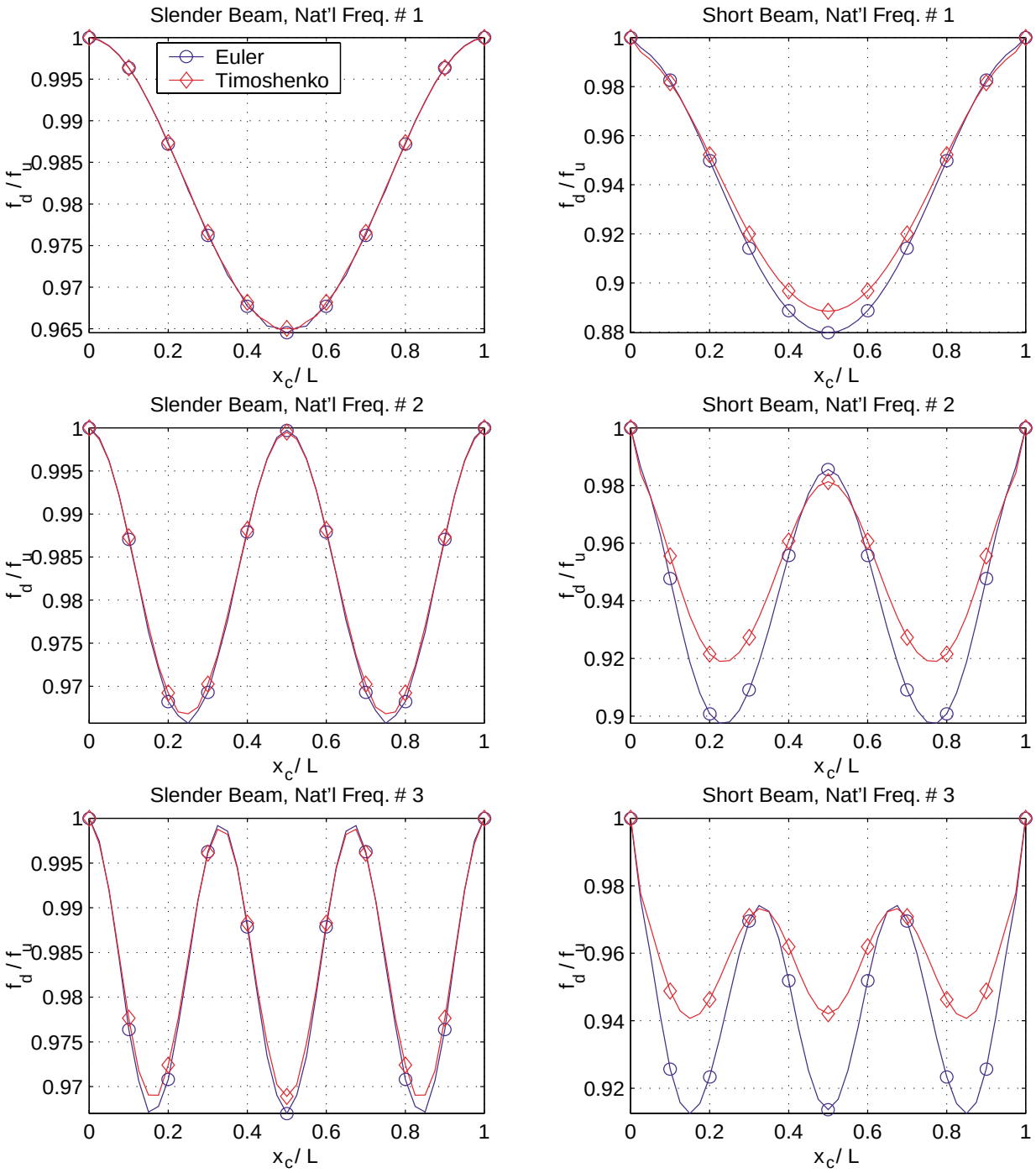

Figure 4.13: Variation of normalized natural frequencies of simply supported beams with respect to crack location. Short beam: $L/2d = 4$; Slender beam: $L/2d = 20$; Crack depth: $a/2d = 0.3$.

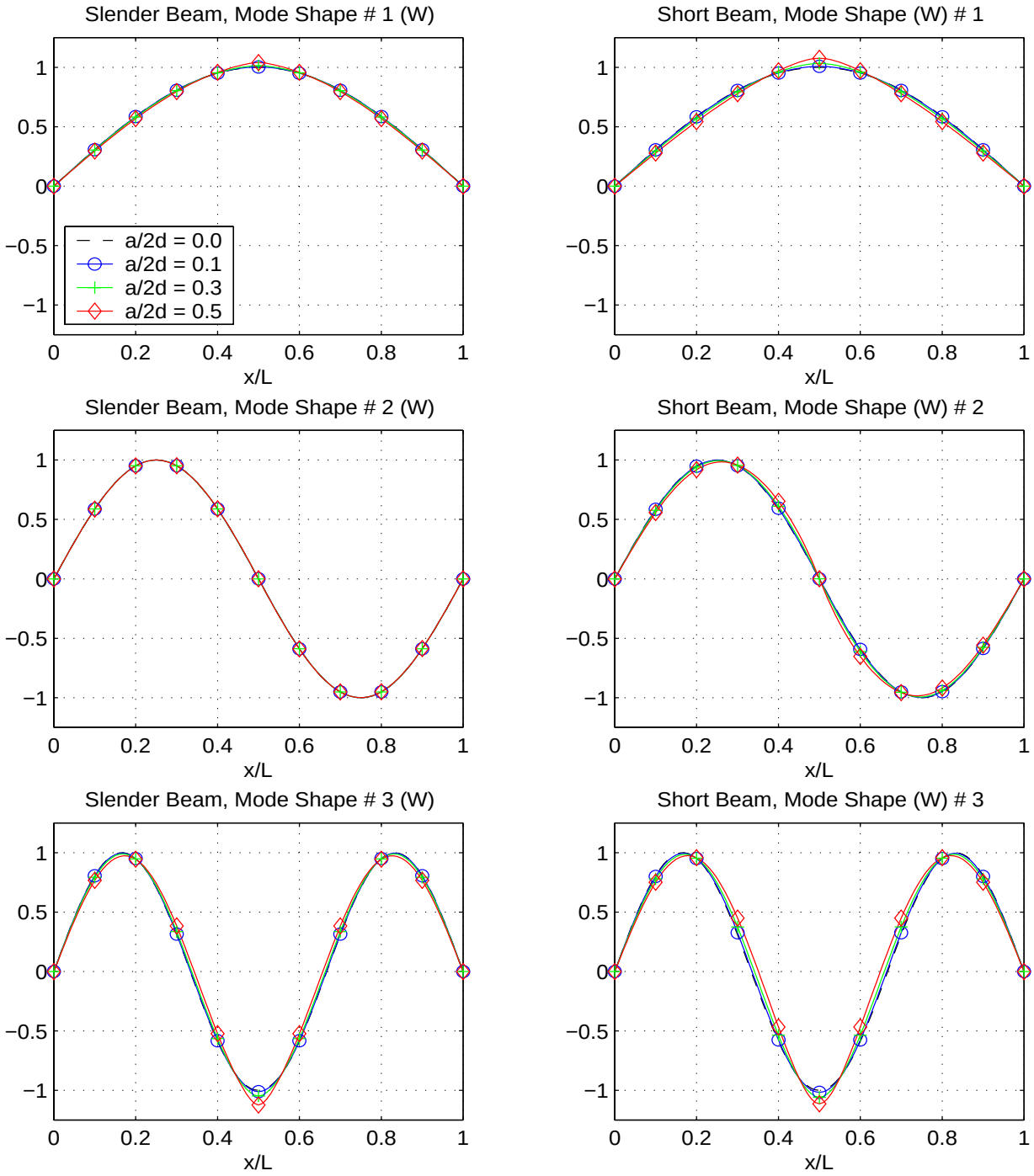

Figure 4.14: Influence of crack depth on displacement mode shapes of a simply supported Timosehnko cracked beam. $x_c/L = 0.5$.

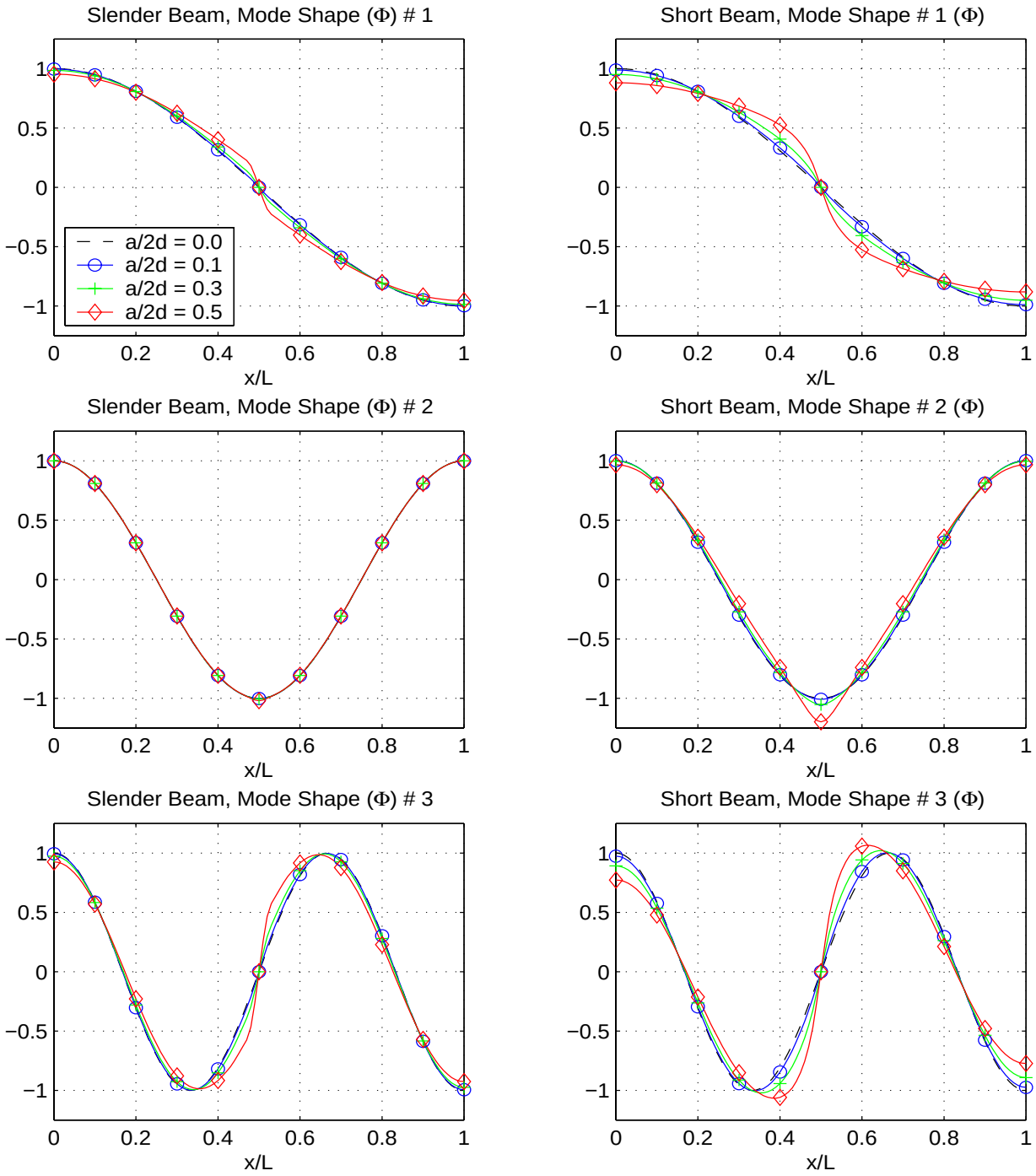

Figure 4.15: Influence of crack depth on rotation mode shapes of a simply supported Timoshenko cracked beam. $x_c/L = 0.5$.

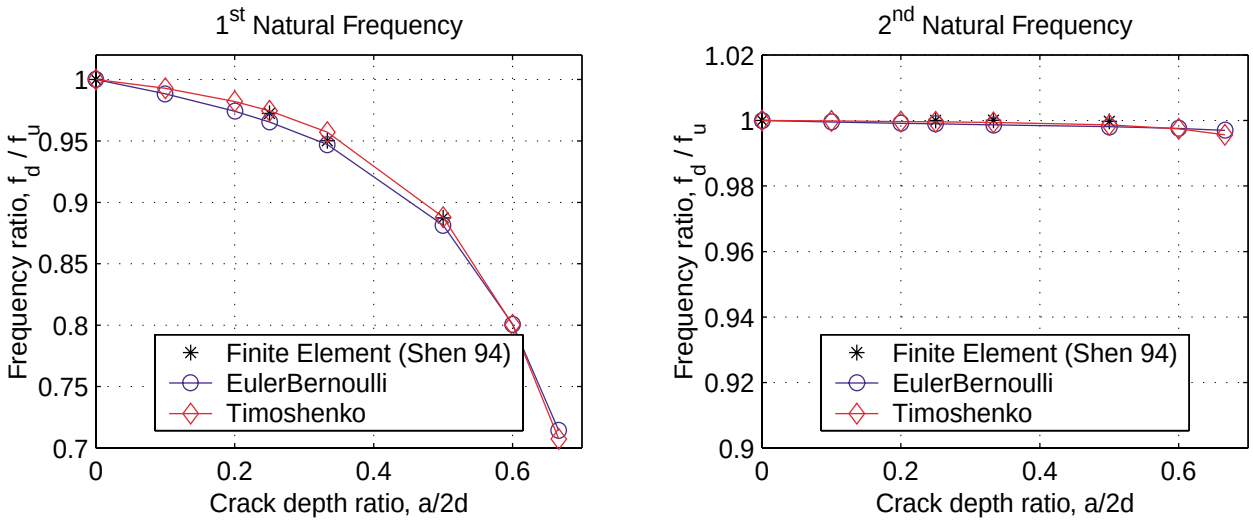

Figure 4.16: Comparison of finite element model and beam theory results for the first and second natural frequencies of a simply supported beam with a midspan crack.$L/2d = 20$. FE results from Reference [101].

to simulate the $1/\sqrt{r}$ singularity. The same value $\alpha_1 = \alpha_2 = 1.276$ was used in the present implementation, and the results are in very good agreement with both the FE model and the Euler-Bernoulli (E-B) model.

Another set of comparisons was performed with experimental results published by Wendtland and reproduced in Reference [101]. Figure 4.18 shows the frequency variation for the first and third natural modes of a cantilever beam obtained by both E-B and Timoshenko models. Once again the agreement with experimental data is satisfactory, but no evident advantages of the Timoshenko model can be inferred since all the available data is from slender beams.

4.3.5 Comparison with Finite Element Model

In order to validate the cracked Timoshenko beam model when applied to short beams, two-dimensional finite element models were created using the commercial FE package ABAQUS. A simply supported beam with aspect ratio of 5 and properties described in Table 4.3 with different crack depths was modeled and the results are discussed in this section.

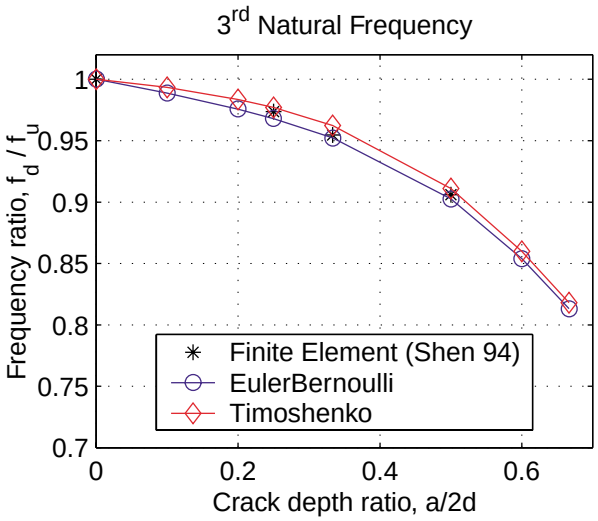

Figure 4.17: Comparison of finite element model and beam theory results for the third natural frequencies of a simply supported beam with a midspan crack. $L/2d = 20$. FE results from Reference [101].

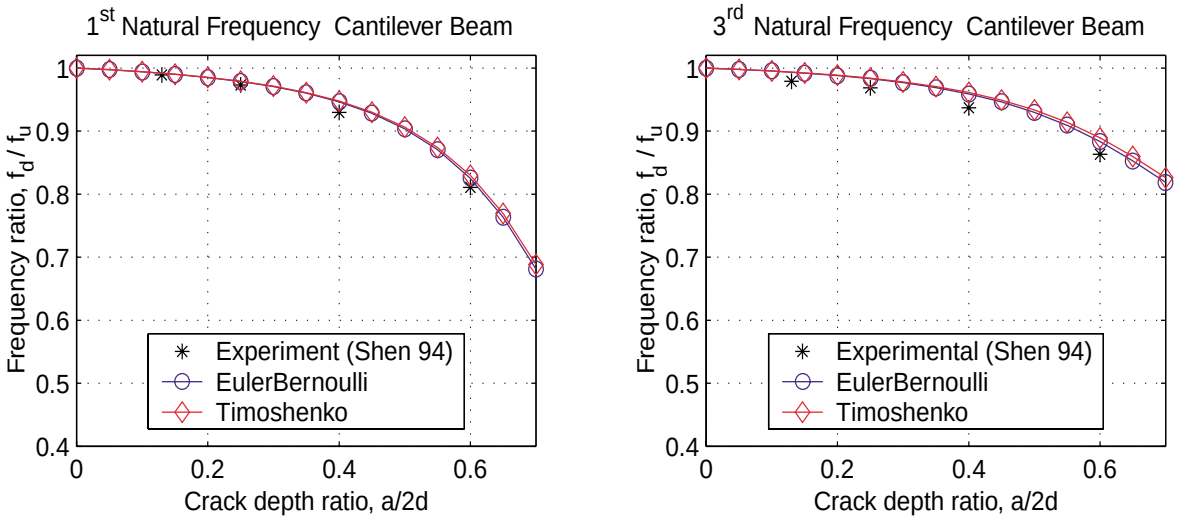

Figure 4.18: Comparison of experimental and beam theory results for the first and third natural frequencies of a simply supported beam with a midspan crack. $L/2d = 25.64$. Experimental results from Reference [101].

Table 4.3: Properties of simply supported short beam for validation against FE model.

Property	Value
Dimensions $L \times 2d \times 2b$ (m)	1.25e-1 $\times$ 2.50e-2 $\times$5.00e-3
Young's Modulus E (GPa)	200
Shear Modulus G (GPa)	76.9
Poisson's Ratio ν	0.3
Density ρ (m/kg^3)	7810

Description of the Finite Element Model

The cracked beams were discretized using 2D, eight-noded quadrilateral, plane stress elements corresponding to the CPS8R reduced integration elements in Ref. [52]. The cracked region was modeled using a focused mesh which creates a progressively refined grid as the crack tip is approached, as illustrated in Figure 4.19. In addition, the mid-side nodes of the elements around the crack tip are moved to 1/4 point of the corresponding side (measured from the crack tip) in order to produce the required stress singularity. These crack tip elements are in fact triangular as a result of collapsing the three nodes of one of the sides of the original quadrilateral, and the coinciding nodes are joined via multipoint constraint equations. This meshing technique is typical in linear fracture mechanics analyses and produces a stress singularity of the form $1/\sqrt{r}$ around the crack tip, as discussed in Ref. [52].

At the simple supports, additional constraints were introduced at the lateral surfaces in order to better approximate the boundary conditions and minimize end effects that are not accounted for in the beam models. Due to possible complex interactions of the stress disturbances induced by the support and the disturbances induced by the crack, the actual point of support in the finite element model that better approximates the simply support condition of the beam model cannot be determined *a priori*. However, it can be assumed to be somewhere between two limiting points: the midpoint of the original cross section, $z = 0$,

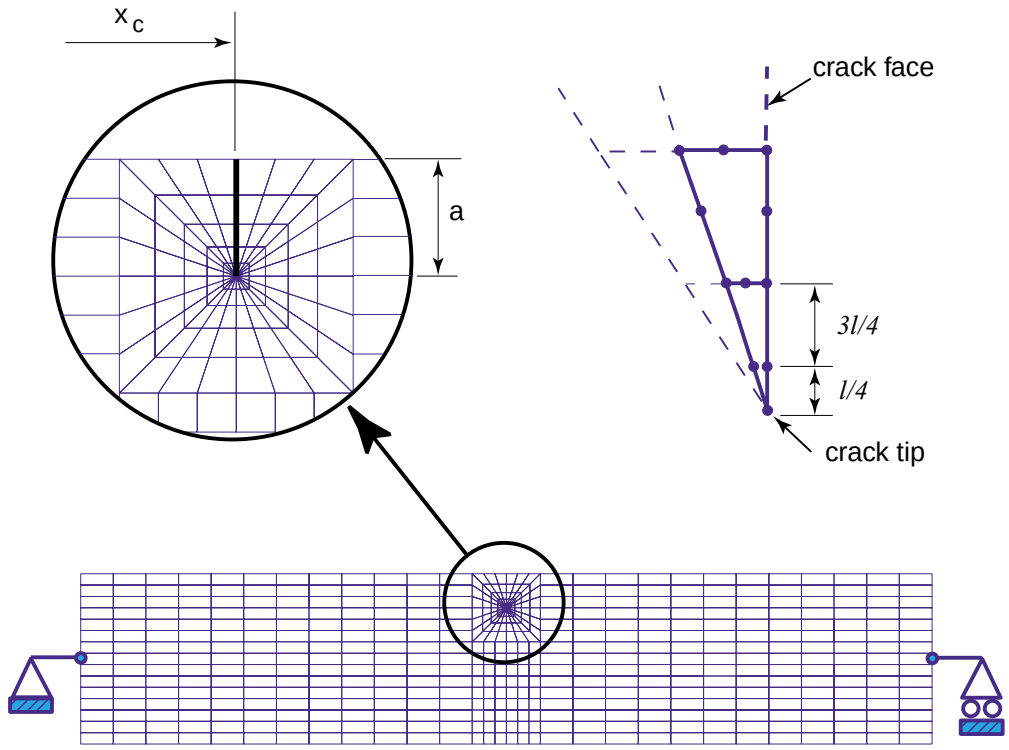

Figure 4.19: Finite element model of a simply supported short beam, with detailed illustration of the mesh at the cracked region. $L/2d = 5$.

which would correspond to the undamaged case; and a point with z coordinate equivalent to the midpoint of the cracked section, $z = -a/2$, which would correspond to a uniform beam of reduced cross section. It should be noted that this discussion is only relevant for short beams, and more evident for higher modes, since in long beams the end effects and the crack disturbances are unlikely to interact and the results obtained from both situations are virtually indistinguishable. For the sake of completeness, finite element results from both support approximations are presented in the following section.

Results

Table 4.4 and Figure 4.20 present the results for the first three natural frequencies for the short beam under simply supported end conditions and a crack at midspan for the finite element, Euler and Timoshenko models. As can be inferred from the plots on the left-hand

side in Figure 4.20, the variations of the normalized natural frequencies of the beam models show good agreement with the finite element results, and significant differences between the Timoshenko and Euler results only become apparent for the third natural frequency. However, when comparing the actual numerical values of the natural frequencies produced by the two beam models, the results from the E-B model are very different from the reference FE results, with discrepancies as large as 40% on the third natural frequency. The advantages of the Timoshenko-type approximation become now very clear, with a much better agreement with the FE model, as shown by the plots on the right-hand side of Figure 4.20.

4.4 Computation of Time Responses

4.4.1 General Procedure

The proposed model was derived in order to be used as a part of a model-based damage diagnosis procedure using time responses. The derived partial differential equations were discretized using a Galerkin approximation with N cubic B-splines as test functions, leading to the equilibrium equations in matrix form

$$[M]\{\ddot{y}\} + [C]\{\dot{y}\} + [K]\{y\} = \{F\} \quad . \tag{4.9}$$

Up to this point, the equations are for a general linear system and can be efficiently solved for the case of a general excitation by standard techniques such as the Duhamel integral after a modal transformation to decouple the system of equations [74, 59]. This will indeed be the method of choice once the current damage state is determined, as discussed in the next sections. For all the examples in this section, we analyze a cantilever beam with properties defined on Table 4.5.

Table 4.4: Comparison of natural frequencies for a short simply supported beam with a mid-span crack.$L/2d = 5$.

1^{st} Natural Frequency (Hz)					
$a/2d$	FE 2D Model	Euler Model	Diff %	Timo Model	Diff %
0.0	3457.2	3671.5	6.20	3449.4	-0.23
0.1	3390.4 3388.2	3571.7	5.35 5.42	3363.4	-0.80 -0.73
0.2	3216.6 3210.9	3430.6	6.65 6.84	3241.0	0.76 0.94
0.3	2959.4 2953.1	3229.6	9.13 9.36	3064.9	3.57 3.79
0.4	2634.4 2632.1	2944.4	11.77 11.87	2811.1	6.71 6.80
0.5	2254.6 2260.5	2550.7	13.13 12.84	2453.3	8.81 8.53
2^{nd} Natural Frequency (Hz)					
$a/2d$	FE 2D Model	Euler Model	Diff %	Timo Model	Diff %
0.0	12045	14686	21.92	11964	-0.67
0.1	12045 12084	14644	21.58 21.19	11905	-1.16 -1.48
0.2	12038 12164	14580	21.11 19.86	11835	-1.69 -2.70
0.3	12016 12219	14474	20.46 18.46	11741	-2.29 -3.91
0.4	11964 12200	14291	19.45 17.14	11595	-3.08 -4.96
0.5	11870 12087	13945	17.48 15.37	11340	-4.47 -6.18
3^{rd} Natural Frequency (Hz)					
$a/2d$	FE 2D Model	Euler Model	Diff %	Timo Model	Diff %
0.0	23115	33043	42.95	22859	-1.11
0.1	22788 22806	32312	41.79 41.68	22514	-1.20 -1.28
0.2	22032 22184	31371	42.39 41.41	22084	0.24 -0.45
0.3	21114 21544	30191	42.99 40.13	21536	2.00 -0.04
0.4	20246 21027	28777	42.14 36.86	20843	2.95 -0.88
0.5	19551 20632	27187	39.06 31.77	20000	2.30 -3.06

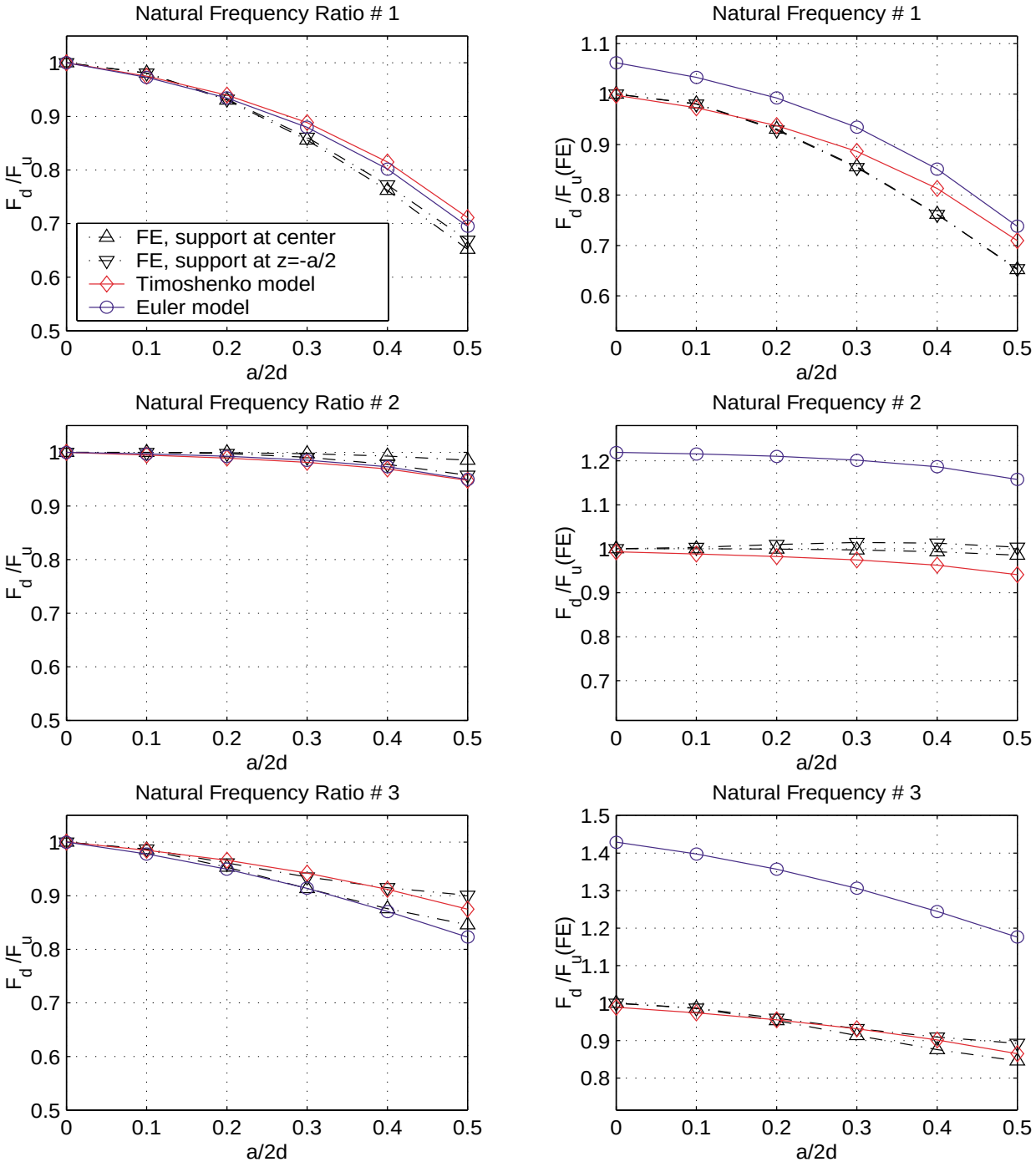

Figure 4.20: Variations of the normalized values of natural frequencies of a short simply supported beam with a midspan crack. $L/2d = 5$. Left-hand-side plots: values normalized by the undamaged natural frequency from the corresponding model; right-hand-side plots: values normalized by the undamaged natural frequency from the 2-D FE model.

Table 4.5: Properties of cantilever beam for computation of time responses.

Property	Value
Dimensions $L \times 2d \times 2b$ (m)	2.5 × 2.5e-1 ×2.5e-2
Young's Modulus E (GPa)	73
Shear Modulus G (GPa)	28
Poisson's Ratio ν	0.3
Density ρ (m/kg^3)	2766
Damping coefficient * c_D (N/m^{2}s)	1e-2
Damping coefficient * γ (N/m^{2}s)	6e5

4.4.2 Damping Model

The effect of fatigue cracks on damping is extremely difficult to characterize and is still an open area of research. Experimental work available in the literature show inconclusive and sometimes contradictory results, and a realistic mathematical model is yet to be proposed [61, 39]. Experimental results by Jones [61] using metallic beams indicate that significant damping changes only occur when severe cracks are present and the structure is approaching failure. Although the detection of that phenomenon is of importance, the present work is concerned with the potential detection of a crack in its early stages, when changes in stiffness are expected to dominate the damage state. For these reasons, crack-induced damping changes are assumed negligible, and the damping operator $\mathcal{C}$ is represented by a simple combination of internal (Kelvin-Voigt) and external (air) damping. We assume that the internal mechanism can be approximated by the time derivative of the stiffness operator, whereas the external damping portion is of viscous nature. This is equivalent to the damping model successfully used for metallic beams with circular holes in [12] and can be written as

$$\mathcal{C} = \left(c_D \frac{\partial}{\partial t} \mathcal{L} + \gamma \frac{\partial}{\partial t} \right) (.) \tag{4.10}$$

The coefficients c_D and γ can be experimentally obtained by a parameter estimation technique also based on time-domain responses, using information exclusively from the undamaged structure, as suggested in [12]. More refined mathematical representations of the damping operator, including a modified Kelvin-Voigt shear model, are proposed by Wang, 1991 in Ref. [115], and its relative merits were discussed based on a uniform composite beam example. A detailed investigation of damping mechanisms is beyond the scope of the present work and therefore we restrict our analysis to the simplified model given by Equation 4.10.

The damping operator in Equation 4.10 is discretized via the same procedure used for the stiffness and mass matrices. This corresponds to a model of general proportional damping, i.e., the resulting discretized damping matrix can be written as a linear combination of the previously computed mass and stiffness matrices, which brings the advantage of permitting a modal decoupling of the equations of each linear subsystem without doubling the order of the system matrices. Extensions of the damping model to include other mechanisms of energy dissipation such as hysteresis due to fatigue damage, or Coulomb friction forces on the crack surfaces, as well as the possible use of damping parameters as additional damage indicators are interesting potential topics for future research.

4.4.3 Representation of Crack Closure

To simulate the nonlinear "breathing" crack, it is assumed that when the crack is closed the stiffness matrix is identical to the undamaged sate. The crack is assumed to remain completely closed until the axial strain in the crack tip region becomes positive (tension). The crack then opens and the damaged stiffness matrix is obtained from the model derived in Chapter 3, which means,

$$[K] = \begin{cases} [K]^{(D)}, \ \epsilon_{xx} > 0 \\ \\ [K]^{(U)}, \ \epsilon_{xx} < 0 \end{cases} \text{(at crack tip).} \tag{4.11}$$

The superscripts (D) and (U) stand for damaged and undamaged states, respectively. It is further assumed that both the mass and damping matrices do not change throughout the

crack-breathing cycles. The resulting nonlinear model can be viewed as bilinear, since it preserves the properties of linear systems within the damage and undamaged states, and all nonlinear characteristics come from the breathing mechanism. Numerous crack closure models have been proposed based on a much more detailed representation of the cracked region to account for partial and incremental closing, interface force computations, etc. The chosen crack closure model has the advantage of capturing the main source of nonlinearity at a relatively low numerical cost. At each time step, the check of crack status is based on the axial strain at the crack tip derived from the current displacement field using the expression

$$\epsilon_{xx}(t)|_{\text{crack tip}} = (-z + f_1)(Q_1\psi' + Q_2\psi)|_{x=x_c;z=d-a} \ , \tag{4.12}$$

which results from the derivation in Chapter 3. The sign of ϵ_{xx} determines the damage state to be used for the next time interval according to Equation (4.11). When a change occurs, the stiffness matrix is updated accordingly and the solution proceeds by taking the current displacements and velocities as initial conditions for the next interval.

4.4.4 Adaptive Time Step Implementation

A crucial issue in the closure model is a precise representation of the instants when stiffness changes, which could be numerically accomplished by a selection of a sufficiently small time step. However, the computational costs involved would not be compatible with the goal of a fast and reliable model to be used as part of a health monitoring method. Since in general those instants cannot be determined beforehand, an adaptive time-step procedure needs to be added to the chosen numerical solution routine. It is important to register that this adaptive scheme is independent from inherently adaptive methods like numerous Runge-Kutta ODE integration procedures of varying orders. Instead, this is an additional adaptive loop, solely aimed on precisely pinpointing the switching instants in the crack opening-closure cycles.

A simple and yet very efficient implementation of the adaptive feature may be accomplished by successive bipartitions of a reference time interval, illustrated by the block diagram in

Table 4.6: Comparison of relative execution time for adaptive time step procedure.

Δt (s)	$\Delta\tau$ (s)	Execution Time
1e-4	1e-4	100 (ref.)
1e-2	1e-4	5.4
1e-2	1e-3	4.9
1e-2	1e-2	1.8

Figure 4.21. The module can be easily added to any chosen time integration routine, preserving all its advantages for the time intervals between crack closure events. Figure 4.22 depicts the free vibration time histories calculated with four different combinations of time interval Δt and refinement tolerance $\Delta\tau$ described in Table 4.6 along with the relative computational costs, taking the most refined, fixed integration step results as reference. The results using the larger fixed time step are clearly erroneous and could lead to completely wrong identification. It can be noticed that the introduction of the adaptive capability leads to very good results with considerable savings in execution time, with no noticeable error propagation even after several cycles of vibration.

4.4.5 Excitations

An important decision to be made when implementing a time-domain diagnostic method is the choice of excitation signal. Some of the issues that have to be considered are relatively obvious, such as repeatability and a frequency bandwidth able to excite a reasonable number of modes. An additional concern related to the proposed methodology is the impact of the selected excitation method on the cost involved in the computation of responses, which have to be performed several times during the identification phase. Impact excitations would meet the broadband requirements with the additional advantage of leading to time records with large portions of easy-to-compute, free vibration responses, but repeatability would be hard

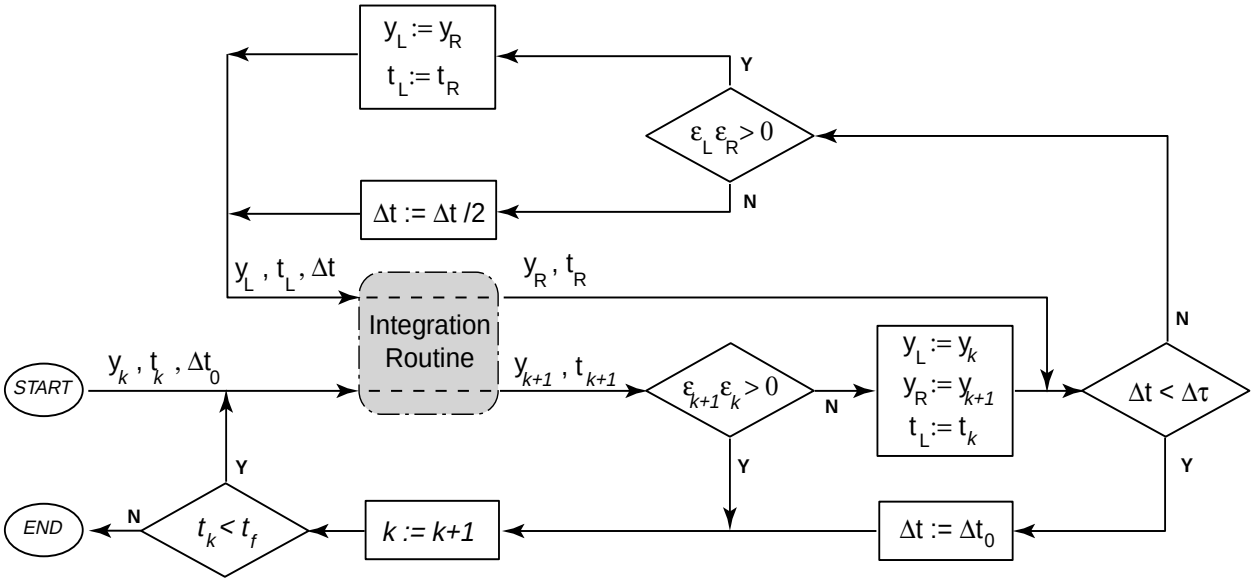

Figure 4.21: Block diagram of the adaptive time step algorithm to identify crack opening/closure instants.

to accomplish. Sinusoidal excitations, on the other hand, have the nice feature of allowing closed form solutions for each linear subinterval, but with limited frequency content.

The use of a single low frequency sinusoidal excitation to characterize the presence of cracks has been proposed by Shen in 1998 [98]. The idea is to analyze the response spectrum looking for peaks at harmonics of the excitation frequency and combinations of the excitation frequency and the system's natural frequencies, which characterizes the nonlinear behavior caused by a crack. Figure 4.23 shows the numerical response of a cracked beam to a low frequency excitation (5 Hz), with the corresponding spectral data shown on Figure 4.24, where we can notice peaks at multiples of the driving frequency and also strong peaks at $f_1 + 5$ and $f_1 - 5$ Hz, confirming Shen's predictions. Similar conclusions can be inferred from free vibration time records after transient excitations such as a short impact, or imposition of nonzero initial conditions, as depicted in Figures 4.25 and 4.26. The power spectrum plots do indeed reveal the existence of nonlinearities, but for crack location and quantification (Level 3) the same restrictions of frequency domain detection procedures discussed in Chapter 1 still apply. In fact, frequency information of the type shown on Figure 4.24 would make difficult,

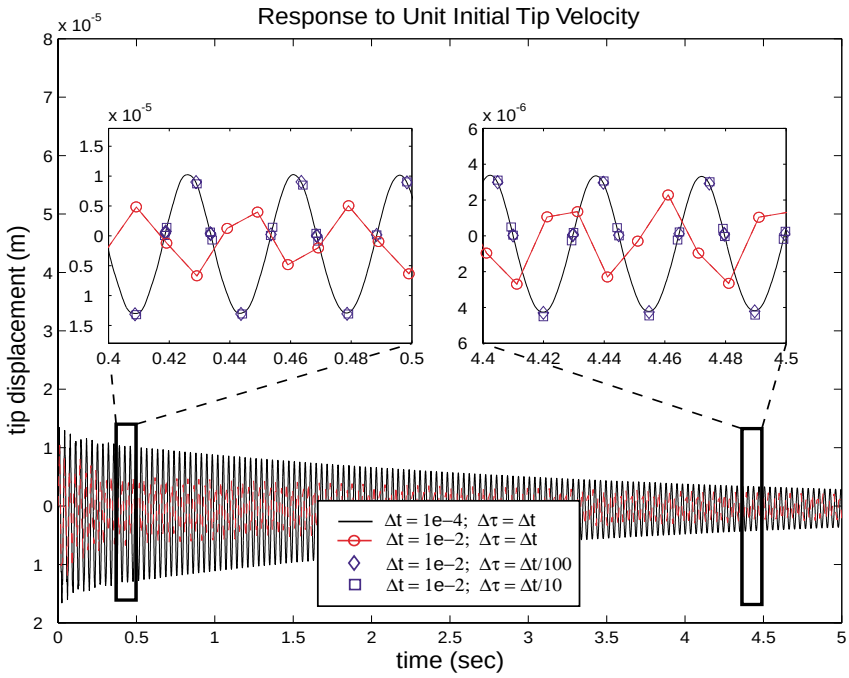

Figure 4.22: Time responses due to initial velocity at tip computed with different combinations of time step and adaptive refinement tolerance.

if at all possible, the application of experimental modal analysis techniques. The alternative approach of taking advantage of those nonlinear signatures as a quick qualitative detection and then using the same available time records in the proposed time domain monitoring method to achieve Level 3 diagnostic is investigated in Chapter 5.

Another option for excitation is the use of multi-sine, Schröeder-phased signals [96], which can be tailored to uniformly excite a desired frequency bandwidth for the experimental data collection and allow fast computation of the corresponding numerical responses. The construction of the excitation signal is performed by a straightforward algorithm that calculates sinusoidal components and phase angles from user-defined bandwidth and spectral resolution, with the requirement of uniform spectral content and minimum amplitude scatter. Figure 4.27 illustrates time records of Schröeder signals and the corresponding frequency spectra for inputs designed to excite a frequency band around the first three natural frequencies of the cantilever beam. The bandwidths are chosen to range from 75% to 105% of the corre-

sponding undamaged beam, therefore increasing the chances of capturing the effects of any possible damage. This is the same strategy proposed in Reference [12] for linear systems and its possible application to the nonlinear problems will also be investigated in Chapter 5.

4.4.6 Numerical Response Results

Figures 4.28 to 4.30 depict time responses of a cantilever beam to Schröeder-phased inputs around the first and second natural frequencies. The undamaged, open-crack and breathing crack responses are compared for the case of crack depth ratios $a/2d = 0.05$, 0.25 and 0.5. It can be noticed that the time responses from the damaged and undamaged structure become distinguishable after a number of vibration cycles. It is also evident that for the results for 5% crack depth ratio, Figure 4.28, the differences are less pronounced and will require a longer time record in order to capture the differences due to small flaws. Another important result is that the linear and nonlinear damaged models differ substantially both in frequency and in amplitude in the more severe damage scenarios, which is an early indication that the use of linear models in the proposed health monitoring technique may lead to considerable inaccuracies in the diagnostic results, as discussed in more details in Chapter 5.

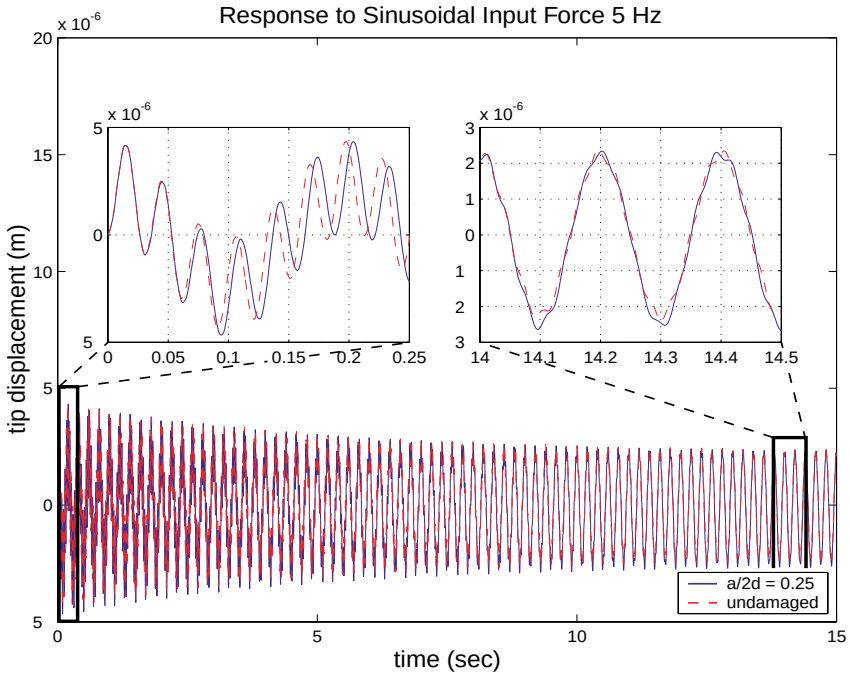

Figure 4.23: Time responses to a 5 Hz sinusoidal excitation at the tip.

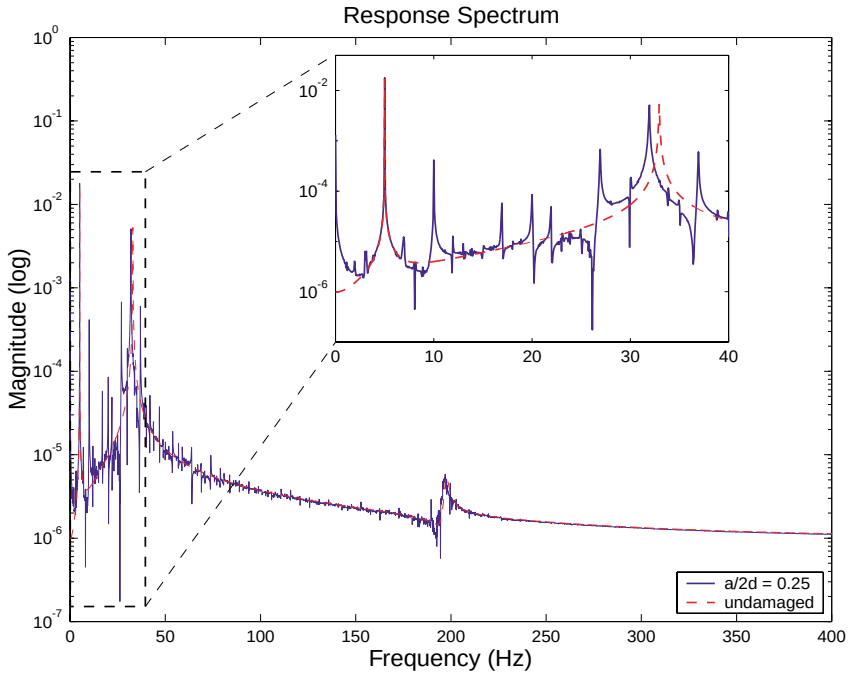

Figure 4.24: Power Spectrum of the responses to a 5 Hz sinusoidal excitation at the tip.

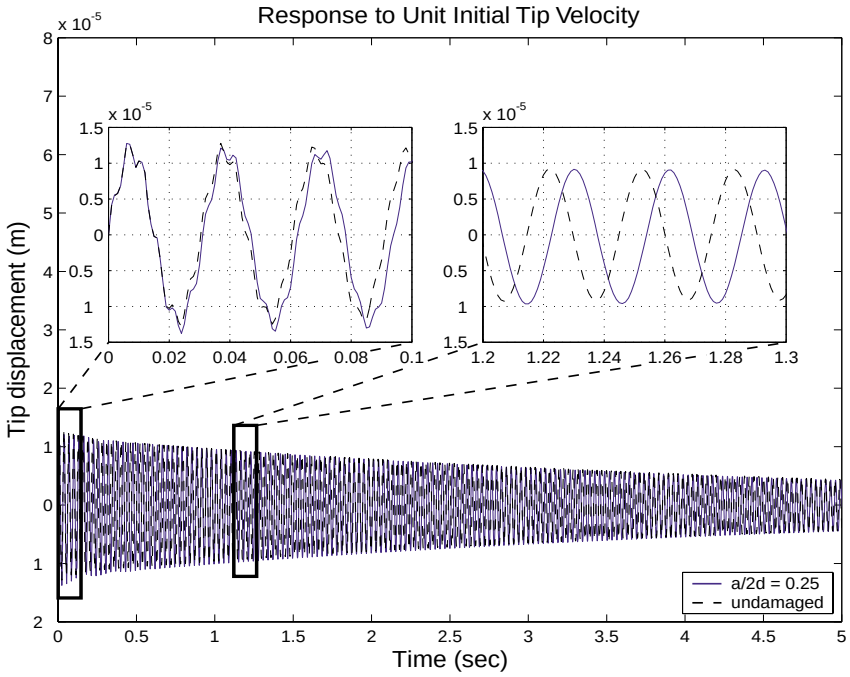

Figure 4.25: Time responses to a unit initial tip velocity.

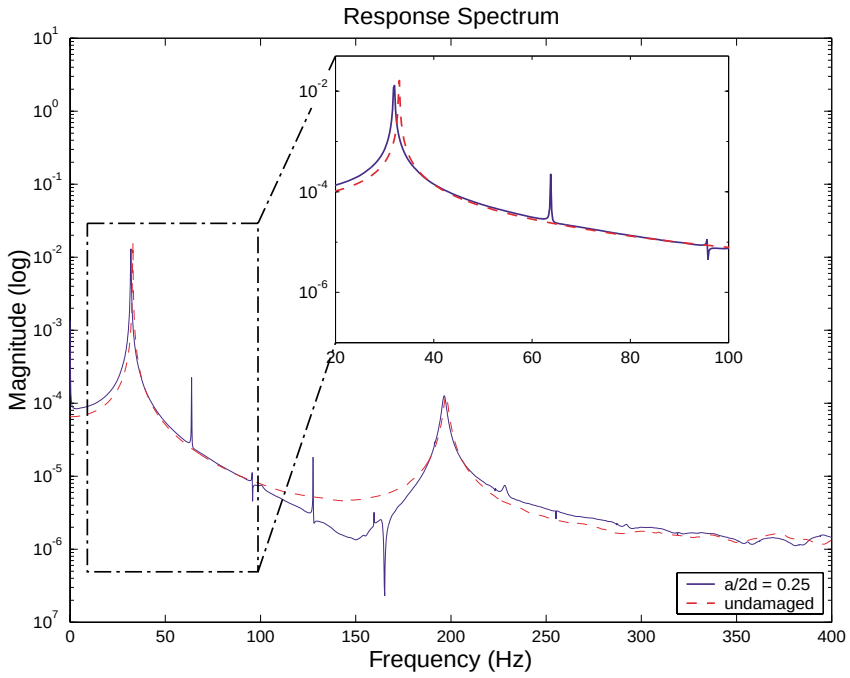

Figure 4.26: Power Spectrum of the responses to a unit initial tip velocity.

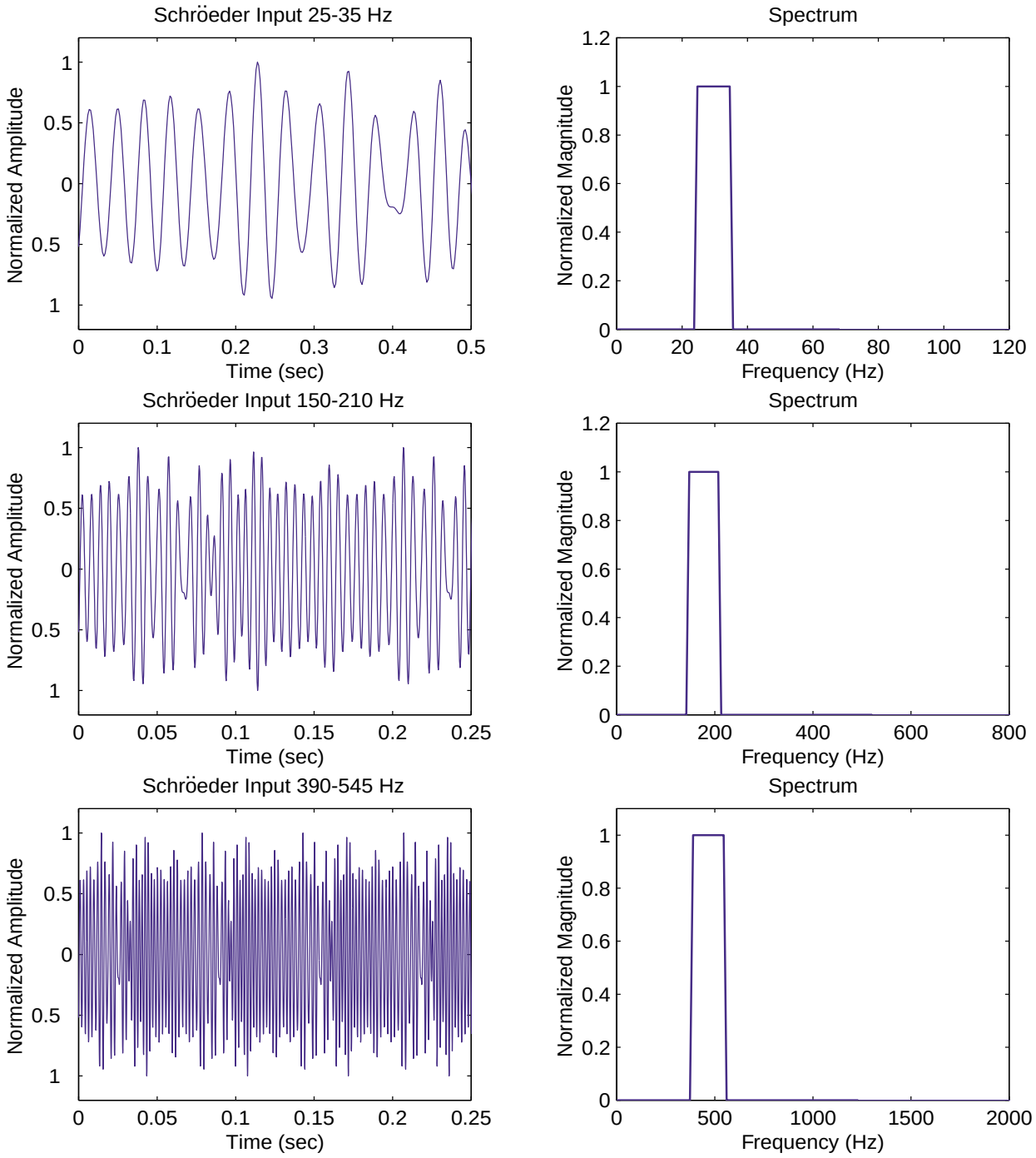

Figure 4.27: Schröeder phased multi-sine excitations.

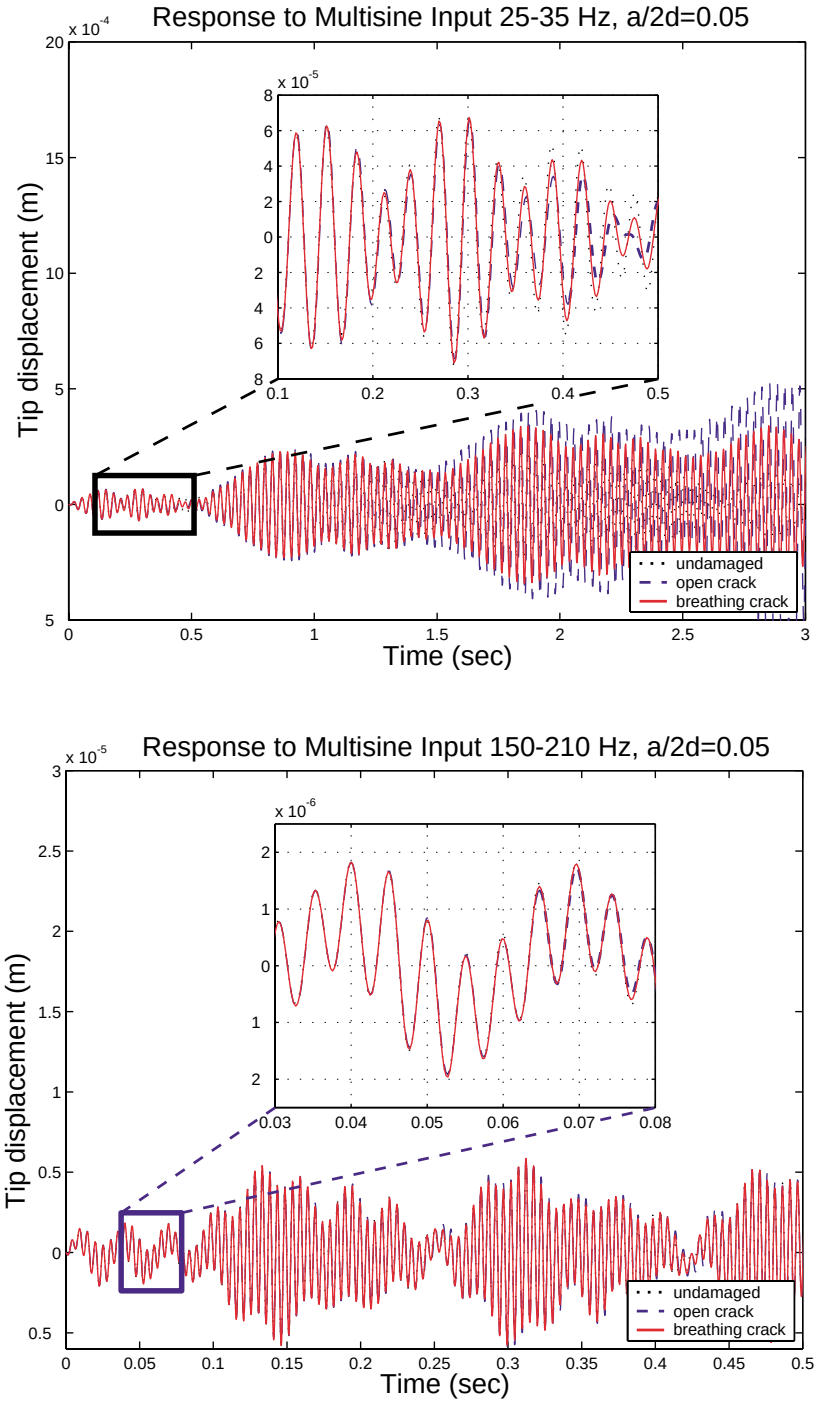

Figure 4.28: Time response to a Schröeder phased input in the vicinity of the first and second natural frequencies. $a/2d = 0.05$.

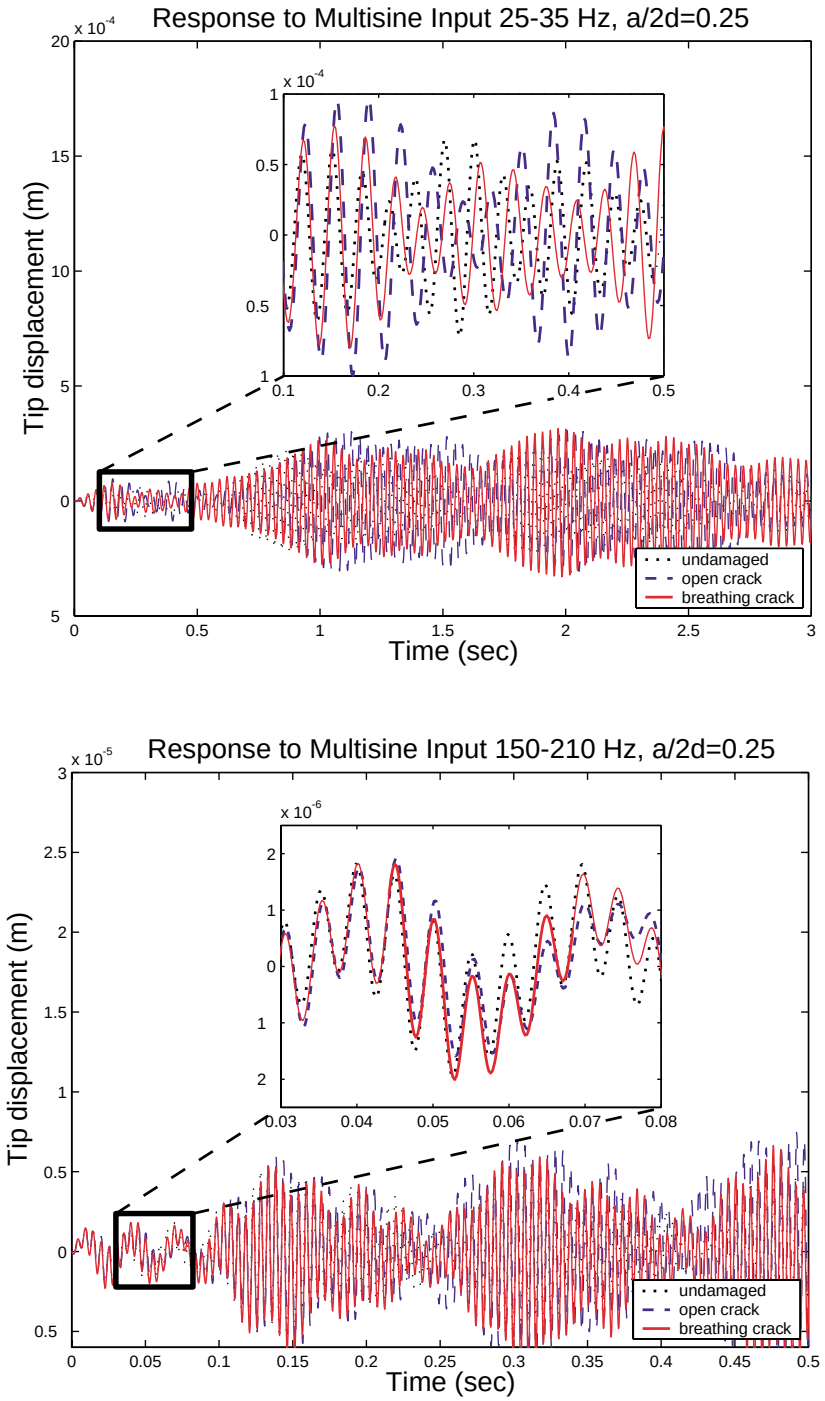

Figure 4.29: Time response to a Schröeder phased input in the vicinity of the first and second natural frequencies. $a/2d = 0.25$.

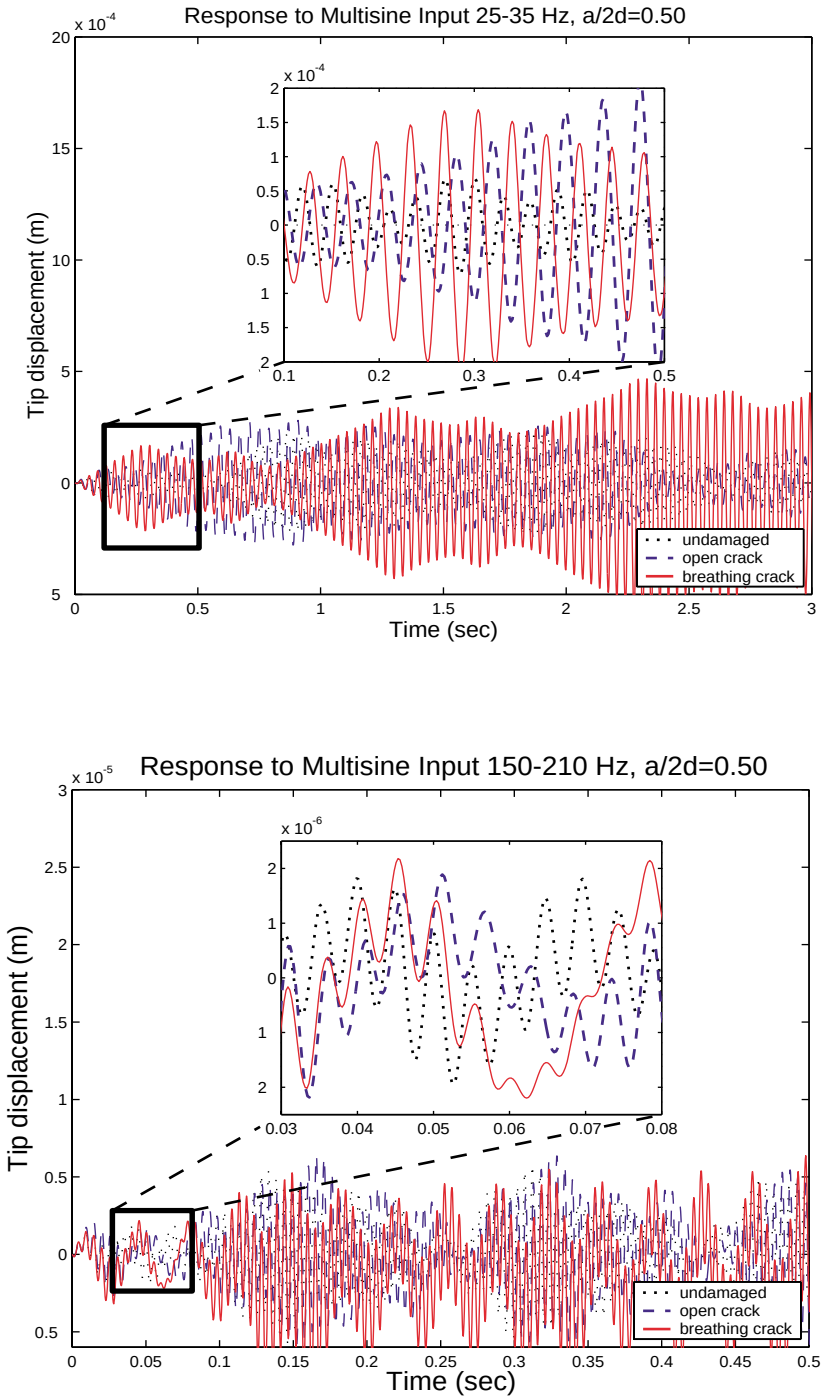

Figure 4.30: Time response to a Schröeder phased input in the vicinity of the first and second natural frequencies. $a/2d = 0.50$.

Chapter 5

Time Domain Crack Diagnostic via Genetic Algorithms

5.1 Introduction

The majority of health monitoring techniques proposed in the literature are based on frequency domain data. As discussed in Chapter 1, certain limitations are inherent to that family of methods, especially when dealing with crack detection problems which involve both small defects and nonlinear behavior. The procedure proposed here aims to overcome those limitations by utilizing time domain information, which presents two important advantages: first, the use of raw data before the extensive data reduction involved in modal tests offer the possibility of a better characterization of small flaws, as discussed in [12]; and second, the use of time domain responses permits a more straightforward inclusion of nonlinear characteristics as part of the identification process via a nonlinear numerical model that captures more closely the behavior of the physical system. Figure 5.1 illustrates the time responses and corresponding power spectra for damped single-degree-of-freedom system under free vibration where the damaged state is represented by a 1% drop in the undamped natural frequency. It is clear that the spectral data do not provide much information for

damage detection since the curves are nearly coincident. In an actual structure, noise and limitations in equipment resolution will only make things even more difficult. On the other hand, the time records, which are obviously not affected by limitations in the data spectral analysis process, have a greater potential of characterizing the presence of damage, provided the time record is long enough to characterize the differences between the responses for the damaged and undamaged states.

The proposed diagnostic technique is based on a parameter identification procedure. More specifically, it is an enhanced nonlinear least-squares estimation of the variables representing damage site and severity. The method consists in minimizing a defined cost function that represent some norm of differences between the measured and numerical responses. Defining a cost function $\mathcal{J}$ similar to the one proposed by Banks and co-authors [12], the identification problem for a beam with a crack of depth a located at x_c can be mathematically stated as

$$MIN\ \mathbf{J}(a, x_c) = \sum_{i=1}^{N_m} c_i \sum_{k=1}^{N_t} \left| w_i^{(x)}(t_k) - w_i^{(n)}(t_k) \right|^2 , \tag{5.1}$$

where $w_i^{(x)}$ and $w_i^{(n)}$ are the N_m experimental and numerical responses, respectively, measured at a total of N_t discrete times t_k. The weights c_i are introduced to account for differences in amplitudes of responses to different excitations.

The minimization process is successfully performed in Ref. [12] by a traditional gradient based method. However, the defined cost function is multimodal, i.e., it presents numerous local minima, which renders the identification procedure extremely dependent on a good initial guess. As a simple example, suppose that the mass and damping properties of a linear damped single-degree-of-freedom system subjected to an initial displacement are known and damage is introduced by a decrease in stiffness, which implies that the spring constant K_d would be the parameter to identify in a diagnosis procedure. If we compute the corresponding cost function defined in Eq. (5.1) for different values of stiffness constants and use time responses of different durations, we get the results depicted in Figure (5.2). It is clear that when the time record length t_f is too long, the cost function has numerous local minima in the vicinity of the exact match of experimental and numerical stiffness. Another important

consequence of using long time records is that the global minimum becomes "narrower", which can be an additional source of trouble for minimization algorithms. In conclusion, the choice of record length must satisfy two conflicting demands: it must be long enough to reveal subtle differences in the responses caused by small flaws, but not so long that it introduces artificial local minima. For a more realistic example, Figure 5.3 illustrates the cost surface for a cracked beam identification problem where the parameters to be identified are the crack location and depth. In summary, traditional gradient based minimization methods have very little chance of success in finding the global minimum and hence identifying the desired damage parameters. In order to overcome those intrinsic limitations of the problem, the use of genetic algorithms is proposed and the fundamentals required to a minimum understanding of the method are discussed briefly in the next section.

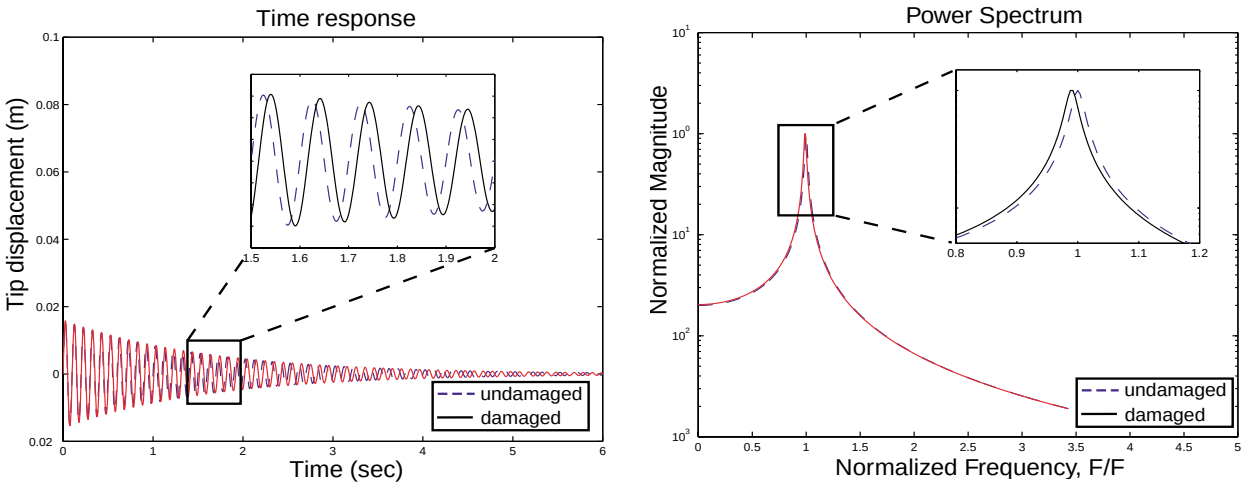

Figure 5.1: Time histories and power spectra for a single-degree-of-freedom system in free vibration. Damage state corresponds to a 1% drop in the undamped natural frequency.

5.2 Basics of Genetic Algorithms

Genetic Algorithms (GA's) are a subset of evolutionary programming techniques, which also encompass neural networks and simulated annealing methods. These techniques were

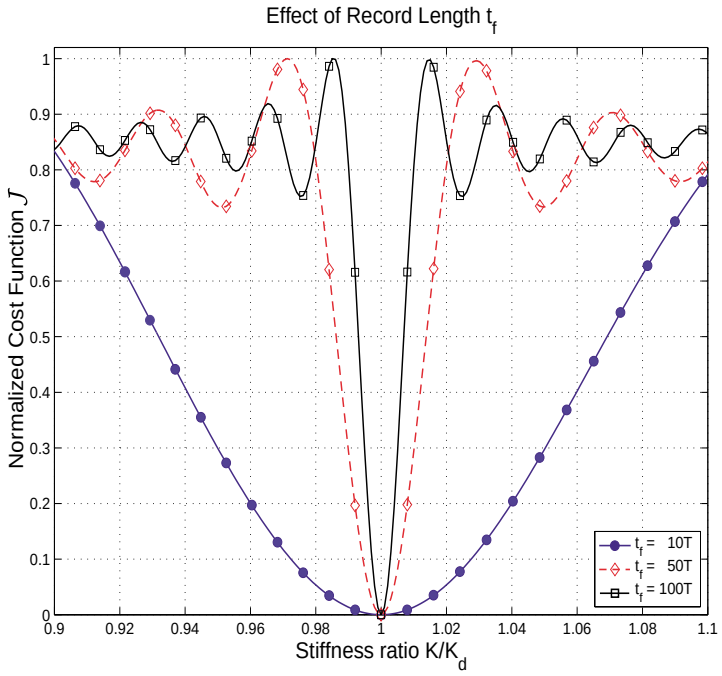

Figure 5.2: Effect of the time record length on the objective function for a SDOF system under free vibration.

inspired on natural processes such as the evolution of biological systems and have been recently used to tackle a variety of engineering problems. More specifically, GA's provide an excellent tool for the minimization of complex, multimodal objective functions and offer many advantages over traditional, gradient based techniques, as highlighted by Haupt [51]:

- GA's do not require the calculation of derivatives, allowing for the treatment of discontinuous and nonsmooth cost functions;
- GA's search the solution space simultaneously from a wide sampling, virtually eliminating any dependence on initial guesses;
- GA's are well suited for parallel computations, ideal when dealing with a large number of parameters;
- The probabilistic transitions involved in the search process provide a much better chance of avoiding local minima and converging to the global minimum.

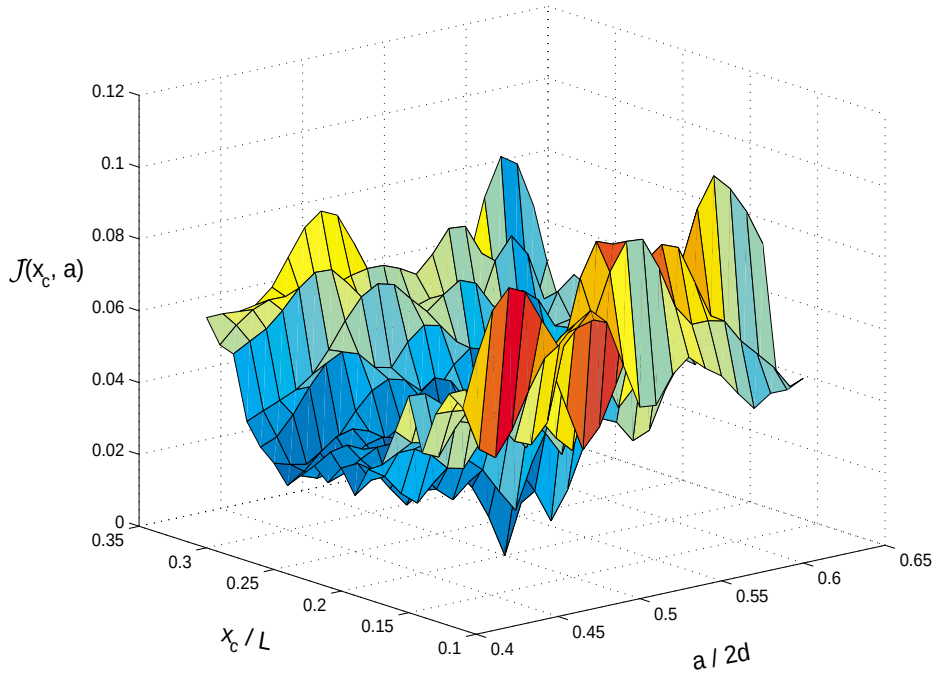

Figure 5.3: Objective function obtained from forced vibration responses of a cracked cantilever beam: one measured point, three narrow band excitations. Crack parameters: $a/2d = 0.5,\ x_c/L = 0.2$.

A block diagram of the steps involved in a typical GA is shown in Figure 5.4, along with a illustrative representation of the basic operators. The nomenclature used by the developers of GA's was borrowed from the theories of genetics and evolution of species, and it provides an intuitive understanding of the philosophy behind the method. The terms used throughout this chapter are defined as follows:

Fitness Function is the equivalent of cost or objective function and is a measure of the quality of a candidate solution. Since GA's are based on the concept of survival of the fittest, the objective function is conveniently modified so that the solution is obtained from a maximization. This is usually accomplished by defining the fitness function as the negative or the inverse of the corresponding cost function.

Chromossomes or Individuals are points in the search space, i.e., a set of allowed values of the parameters to be identified.

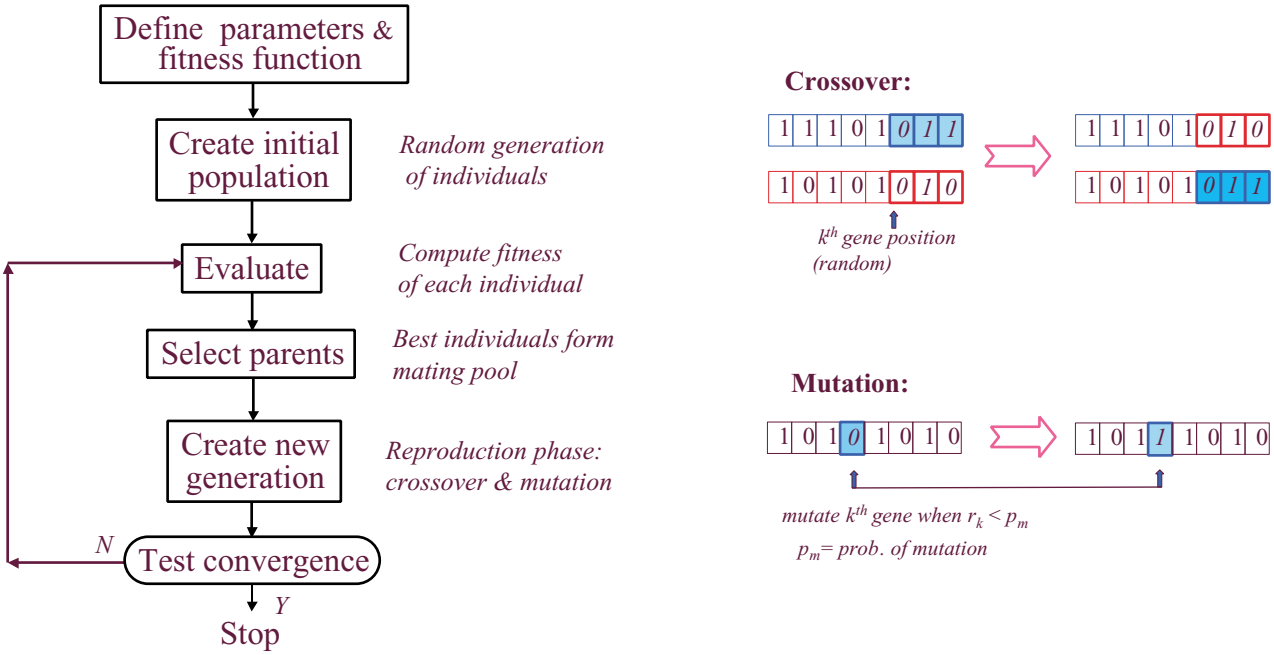

Figure 5.4: Block diagram of a typical genetic algorithm with schematic illustration of the basic genetic operators in binary form.

Population is the set of individuals that is analyzed and modified throughout the maximization process.

Generation is the equivalent to iteration and denotes the successive evolutionary states of the population.

Selection is the driving force of a GA. It is the process that determines which individuals of a given generation will survive to the next and will undergo "reproduction" operations like crossover and mutations to guarantee diversity.

Crossover is the creation of new individuals (offspring) from two selected individuals via exchange of genetic information of the parents.

Mutation is the creation of a new individual from one selected individual by means of a random modification in its genetic content.

There are two basic families of GA's: binary and floating-point. The classification is based on the numerical representation of the independent variables. In the binary family, the variables are coded into sequences of zeros and ones, most of the time as a simple basis transformation of initially real numbers. Binary GA's were the first to be developed, and they are more adequate to problems where the parameters can take on only a finite number of values. It is important to note that in many cases the binary representation is not a mere numerical transformation, but instead an encoding of otherwise discrete, alpha-numeric, or even symbolic variables. For example, a list of warehouses in a transport planning or encrypted words in message decoding are well suited for a binary GA.

Floating-point, or continuous GA's represent individuals by a set of real numbers, each corresponding to the actual value of a parameter. Continuous GA's have the important advantage of permitting greater precision without the corresponding increase of chromosome length that occurs in the binary algorithms. In fact, studies indicate that continuous GA's clearly outperform binary GA's in terms of both computational time and accuracy for optimization and identification problems when all the variables involved are real [55, 75].

In this work, the GA MATLAB package developed by Houck et al. [55] at North Carolina State University was used as the primary tool for the implementation of the proposed diagnostic method. The continuous genetic operators used in the present implementation and the most important parameters involved are revised briefly in the next subsections.

5.2.1 Selection

The process for choosing the fittest members of a population at each generation can be accomplished by methods such as tournament rounds, roulette wheel selection, and ranking methods. The basic idea of most selection methods is to assign a probability of survival P_j to each individual based on its fitness, calculate the cumulative probability $C_i = \sum_{j=1}^{i} P_j$ of the population and use a uniform random number generator in the interval $(0, 1)$ to select the survivors. Individual i is selected if the generated random number $U(0, 1)$ satisfies

$C_{i-1} < U(0,1) \leq C_i$. This ingenious combination of random and fitness-based selection gives the process two equally important properties: the best individuals will always have a greater chance of surviving into the next generation, and any individual has a chance of being selected, which ensures diversity and consequently allows the presence of less fit but potentially good future parents in the population.

The selection method used in this work is the normalized geometric ranking proposed by Michalewicz [75]. The probability P_i of selecting individual i is defined as

$$P_i = q'(1-q)^{r-1}, \tag{5.2}$$

where q is the probability of selecting the best individual, chosen by the user as a measure of the selective pressure of the algorithm, and r is the rank of the individual when the population is ordered according to fitness, i.e., $r = 1$ for the best member and $r = N_p$ for worst, where N_p is the population size. The scaling constant q' is defined as

$$q' = \frac{q}{1-(1-q)^{N_p}} \tag{5.3}$$

and is introduced to ensure that the total cumulative probability of the population is equal to 1. A direct consequence of the probabilistic selection methods is that some chromosomes may be selected more than once, hence mimicking the process of natural selection. The best chromosomes generate more copies, the average ones keep the same relative presence in the population, and the worst are virtually extinct. After the selection step, a mating pool of individuals is available and reproductive operations such as crossover and mutation can now take place in order to complete the generation of the new population, providing the necessary exploration (search) and exploitation (refinement) features of the algorithm.

5.2.2 Crossover Operators

Crossover consists of the generation of new individuals, or offspring, from two selected parents and can be implemented in different mathematical forms. Let's define the representation of

chromosomes as an n-dimensional row vector of real-valued parameters to be identified and denote $X = (x_1, x_2, ..., x_n)$ and $Y = (y_1, y_2, ..., y_n)$ as the selected parents and X' and Y' the corresponding offspring. The crossover operators in a continuous GA are as follows.

Arithmetic Crossover

In this operator, two complementary linear combinations of the parents are created as

$$X' = rX + (1-r)Y \tag{5.4}$$

$$Y' = (1-r)X + rY, \tag{5.5}$$

where r is a uniform random real number $U(0,1)$, which guarantees that the offspring will have all genes within the corresponding parameter bounds (a_i, b_i) .

Simple Crossover

This is the most intuitive crossover operator. The genetic information of two individuals is exchanged after a partition at the k^{th} position of the row vector, where k is a uniform random integer between 1 and n. The mathematical expression of the operator is

$$X' = (x_1, x_2, ..., x_k, y_{k+1}, ..., y_n) \tag{5.6}$$

$$Y' = (y_1, y_2, ..., y_k, x_{k+1}, ..., x_n). \tag{5.7}$$

Despite its simplicity, this operator does not guarantee closure, which means that the offspring may be outside the feasible solution space. To overcome this difficulty, Michalewicz proposes the use of a property of convex spaces that there exists $a \in [0,1]$ such that

$$X' = (x_1, x_2, ..., x_k,\ a \cdot y_{k+1} + (1-a) \cdot x_{k+1}, ..., a \cdot \cdot y_n + (1-a) \cdot x_n) \tag{5.8}$$

$$Y' = (y_1, y_2, ..., y_k,\ a \cdot x_{k+1} + (1-a) \cdot y_{k+1}, ..., a \cdot x_n + (1-a) \cdot y_n) \tag{5.9}$$

is always feasible. The initial value of a is set to 1, which reduces Equation 5.8 to Equation 5.6. If at least one of the offspring is not within bounds, a is reduced by a constant $1/c$,

where c is an integer. In the unlikely case of c unsuccessful attempts, the resulting value of a is zero and the offspring are identical to the parents. Michalewicz remarks that the necessity of the maximum reduction is usually very small and rapidly decreases throughout the evolution process.

Heuristic Crossover

This is a unique crossover operator, since it generates at most a single new individual and it is the only operator to use fitness information to define the direction of a linear extrapolation of the parents. Suppose that X has better fitness than Y. Then, the operator produces

$$X' = X + r(X - Y) \tag{5.10}$$

$$Y' = X', \tag{5.11}$$

where r is the usual uniform random number $U(0, 1)$. The heuristic operator can generate an offspring that is unfeasible, i.e., one or more of the resulting parameters may be outside its corresponding bounds. Unfeasible offspring are automatically discarded and the operation is repeated. If no feasible offspring is obtained after a predetermined finite number of repetitions, the offspring are taken as identical copies of the parents and no new individual is created.

5.2.3 Mutation Operators

Mutation is a unary operator, i.e., one individual produces a single offspring with a random local modification in its genetic code. The three mutation operators are defined as follows.

Uniform Mutation

In this operator, a position k in the row vector is randomly selected and the k^{th} parameter is replaced by a new, randomly generated value within the corresponding bounds,

$$x_i' = \begin{cases} U(a_i, b_i) \ , \text{ if } \ i = k \\ x_i \ , \text{ otherwise.} \end{cases} \tag{5.12}$$

Boundary Mutation

The mutated chromosome has one of its genes randomly selected and replaced by either its upper or lower bound according to the value of a uniform random number $r = U(0, 1)$, i.e.,

$$x_i' = \begin{cases} a_i \ , \text{ if } \ i = k, \ r < 0.5 \\ b_i \ , \text{ if } \ i = k, \ r \geq 0.5 \ . \\ x_i \ , \text{ otherwise.} \end{cases} \tag{5.13}$$

Nonuniform Mutation

The individual suffers a mutation at a randomly selected gene given by

$$x_i' = \begin{cases} x_i + (b_i - x_i) f(G) \ , \text{ if } \ i = k, \ r_1 < 0.5 \\ x_i - (x_i - a_i) f(G) \ , \text{ if } \ i = k, \ r_1 \geq 0.5 \\ x_i \ , \text{ otherwise,} \end{cases} \tag{5.14}$$

with

$$f(G) = r_2 \left(1 - \frac{G}{G_{Max}}\right)^b , \tag{5.15}$$

where G is the number of the current generation, G_{Max} is the maximum number of generations, and b is a shape parameter determining the degree of non-uniformity. The practical effect of this mutation is a broad search at the beginning of the process and a more local search at later stages of the evolution, which provides fine tuning characteristics to the operator.

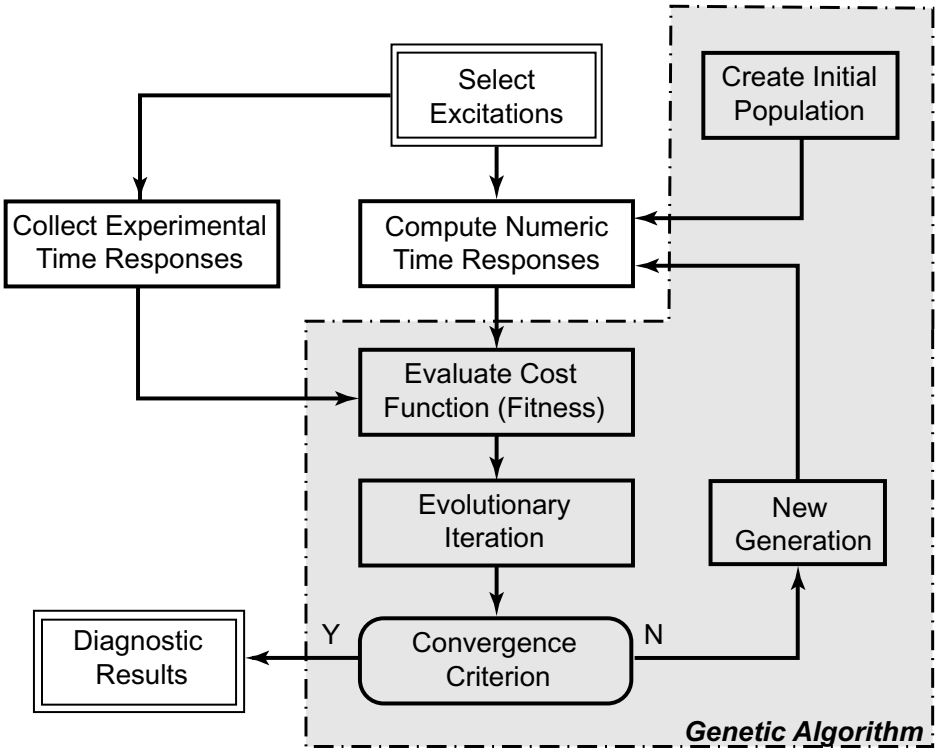

Figure 5.5: Flow chart of the proposed time-domain, model-based crack diagnostic procedure.

5.3 Implementation of the Identification Procedure

Figure 5.5 presents a block diagram of the proposed identification scheme. The first step is the collection of experimental data via measurement of time responses of the damaged structure due to the chosen excitations. Next, an initial population is randomly created, consisting of different combinations of possible crack parameters within defined bounds. For each individual $(a, x_c)_i$, numerical time responses are computed using the model developed in Chapters 3 and 4, and the corresponding fitness is calculated as the negative value of the objective function in Eq. (5.1). The GA is now initialized and successive generations are created through selection and reproduction until a termination criteria is achieved, most commonly based on a maximum number of generations. The process is computationally intensive due the numerous evaluations of time responses, but it has the advantage of allowing straightforward parallelization since the computation of each individual's fitness is completely

independent from others. The entire algorithm is coded in MATLAB programming language, with the cracked beam model and the time response module linked to the GA structure via standard subroutine calls.

5.4 Results

5.4.1 Definition of Test Cases

The structure used in all the investigations in this section is a cantilever beam with aspect ratio $L/2d = 10$ and properties described in Table 4.5. The damage scenarios are defined in Table 5.1 and the loading cases in Table 5.2. Table 5.3 shows the parameters used for the calculation of the simulated experimental records and theoretical time responses used in the diagnostics. The simulated experimental data was generated using more refined parameters, both for model discretization and for time response computations. The calculations were performed using modal superposition for each linear subsystem, with the number of modes also shown in Table 5.3. For the Shröeder excitations, the record length was set to include approximately 25 cycles of vibration of the corresponding natural frequency in the range of excitation. The record length of the response to initial velocity was set to 25 cycles of the first natural frequency of the undamaged structure. For the low frequency sinusoidal input, only the first 10 cycles of excitation were included, since the remaining of the time record reveals very little change due to the damage, as seen on Figure 4.23. All excitations were applied at the tip of the cantilever beam.

Table 5.1: Definition of damage scenarios

Case	**A**	**B**	**C**	**D**	**E**	**F**	**G**	**H**	**I**	**J**	**K**	**L**
x_c/L	0.15	0.15	0.85	0.85	0.15	0.15	0.85	0.85	0.15	0.15	0.15	0.15
$a/2d$	0.05	0.50	0.05	0.50	0.10	0.25	0.10	0.25	0.01	0.02	0.03	0.04

Table 5.2: Definition of loading cases for investigations on the influence of excitation method.

		Frequency Content			
Loading Case	Type of Input	5 Hz	25–35 Hz	150–210 Hz	390–545 Hz
1S	Schröeder	—	X	—	—
2S	Schröeder	—	X	X	—
3S	Schröeder	—	X	X	X
IV	Inicial velocity	—	—	—	—
LF	Low frequency	X	—	—	—

Table 5.3: Numerical parameters used for generations of simulated experimental data and numerical model responses

Parameter	Simulated Test Data	Numerical Responses	Parameter	Simulated Test Data	Numerical Responses
N	50	40	Δt (290–545Hz)	1e-4	1.5e-4
# Modes	10	5	$\Delta\tau$ (290–545Hz)	1e-7	1.5e-5
Δt (25–35Hz)	1.5e-3	2e-3	Δt (IV)	5e-4	1e-3
$\Delta\tau$ (25–35Hz)	1.5e-6	2e-4	$\Delta\tau$ (IV)	5e-7	1e-4
Δt (150–210Hz)	2.5e-4	3.5e-4	Δt (LF)	2e-3	2e-3
$\Delta\tau$ (150–210Hz)	2.5e-7	3.5e-5	$\Delta\tau$ (LF)	2e-6	2e-4

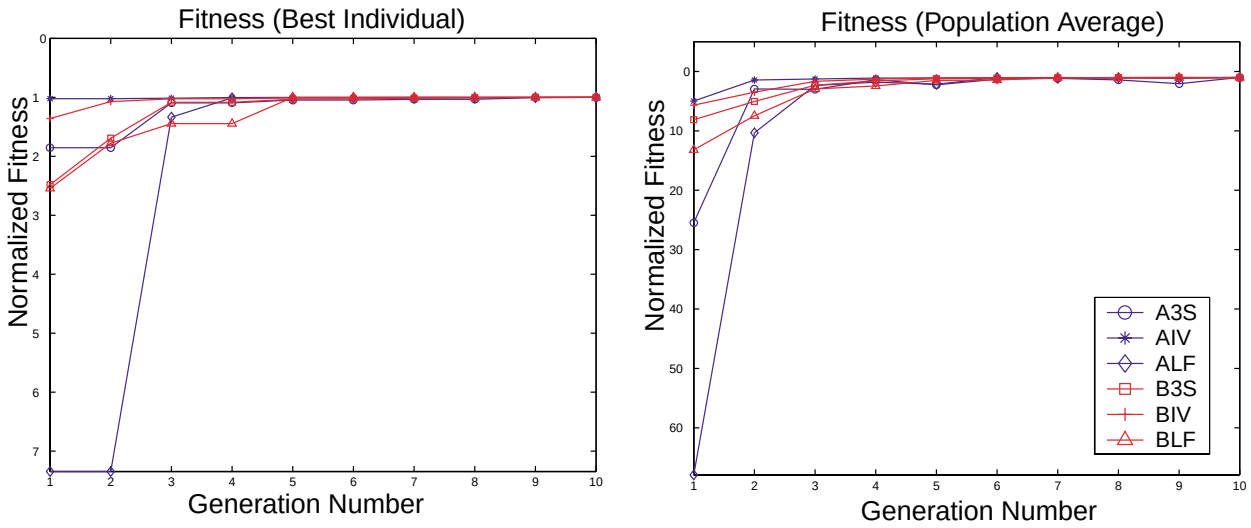

Figure 5.6: Evolution of fitness function for a population of 200 individuals.

5.4.2 GA Parameters

The basic parameters that control the execution of the genetic algorithm are the population size, number of generations, number of selected parents for crossover and mutation, and selection pressure defined by the value of q in Equation 5.2. These parameters can greatly influence the performance of the algorithm, and recommended values are defined in Reference [55] based on the authors' previous experiences applying the GA toolbox to problems in different areas. For the present application, preliminary tests indicated the need of population sizes larger than the default value of 80 individuals, and consequently the mutation and crossover operations were adjusted accordingly. The population size and number of generations were defined after preliminary runs for damage cases A and B, with results shown on Table 5.4. Three initial populations were independently generated such that the individuals of each one are not present in the others. The initial runs with 200 individuals for 10 generations indicated that 5 generations were sufficient for convergence, as depicted in Figure 5.6. In all cases, both the fitness of the best individual and the population average fitness indicate that little was gained by continuing the evolution process. Two new tests were then performed with population sizes of 300 and 400 for 5 generations in order to verify whether

or not the unsuccessful runs would benefit from a larger number of individuals. Although no improvements in the unsuccessful diagnostics were achieved, the computational cost was reduced in as much as 50% and 47%, respectively. Table 5.5 summarizes the values of the GA parameters used in all the remaining in this chapter.

Table 5.4: Preliminary identifications for definition of GA parameters

Pop. Size	200			300			400		
Max. Gen.	10			5			5		
	x_c/L	$a/2d$	Time	x_c/L	$a/2d$	Time	x_c/L	$a/2d$	Time
A3S	0.1400	0.0486	100	0.1400	0.0481	74	0.1612	0.0527	79
AIV	0.3384	0.2499	100	0.3296	0.2329	50	0.3538	0.2484	53
ALF	0.8692	0.0181	100	0.8358	0.0169	63	0.8522	0.3235	65
B3S	0.1398	0.4951	—	0.1390	0.4904	—	0.1623	0.5115	—
BIV	0.2566	0.5237	—	0.0534	0.4890	—	0.0449	0.4852	—
BLS	0.0323	0.4892	—	0.0960	0.4901	—	0.0291	0.4923	—

Table 5.5: Genetic algorithm parameters selected for the identification runs

GA Parameters								
Pop.	Max. #	Selection	Crossover Parameters			Mutation Parameters		
Size	Gen.	Pressure q	Arithmetic	Simple	Heuristic	Uniform	Nonuniform	Boundary
400	5	0.08	10	4	4	8	10	4

5.4.3 Excitation Method

This investigation has the objective of verifying the potential use of three types of excitations: impulse, low frequency sinusoidal and Schröeder-phased multisine inputs. The latter were successfully applied to identify small linear defects [12] and are tested here for a nonlinear system. The use of transient and low frequency sinusoidal excitations has been proposed in the literature for spectral signature analysis that indicates the onset of cracks [98, 16], as discussed in Section 4.4, and the possibility of using the same time records to localize and

quantify the damage is investigated here. Three different combinations of Schröeder inputs (loading cases 1S, 2S and 3S in Table 5.2) are also tested for selected cases. For comparison purposes, a diagnostic is considered satisfactory when results in errors not greater than 20% in any of the two parameters, and at most one parameter with error greater than 15%. The errors of unsuccessful runs are boxed for easy analysis of the tables in this section. The results presented in Table 5.6 indicate that the use of a single impact response, despite the broadband frequency content, was not able to provide successful location for most cases. The same conclusion can be made regarding the low frequency sinusoidal input. As for the Schröeder inputs, consistent identifications only occurred when at least two excitations were used. The effect of noise was not considered and is discussed in the next section.

Table 5.6: Comparison of identification results using different excitations

Load	1S		2S		3S		IV		LF	
Case	x_c/L	$a/2d$	x_c/L	$a/2d$	x_c/L	$a/2d$	x_c/L	$a/2d$	x_c/L	$a/2d$
A	0.2694	0.0749	0.1483	0.0501	0.1612	0.0528	0.3538	0.2484	0.8522	0.3235
B	0.1646	0.5080	0.1626	0.5088	0.1627	0.5115	0.0449	0.4852	0.0291	0.4923
C	0.8926	0.1305	0.9149	0.1822	0.9064	0.1543	0.8704	0.2222	0.9117	0.1822
D	0.8129	0.3777	0.8530	0.5111	0.8388	0.4752	0.7955	0.2319	0.8380	0.4603
E	0.3044	0.1598	0.1442	0.0975	0.1402	0.0961	0.3371	0.2626	0.0652	0.0558
F	0.2008	0.2792	0.1481	0.2492	0.1630	0.2634	0.3769	0.4000	0.2976	0.3405
G	0.8917	0.2140	0.8786	0.1679	0.8641	0.1281	0.8704	0.2222	0.8367	0.0813
H	0.8530	0.2617	0.8512	0.2567	0.8616	0.2767	0.8460	0.1677	0.8574	0.2760

5.4.4 Effect of Noise

To verify whether or not the suggested method was sensitive to the inevitable measurement noise, different levels of normal random noise were added to the simulated experimental responses and the identifications for all crack lengths at a fixed location $x_c/L = 0.15$ were repeated. The advantages of using a third excitation were also investigated. The results presented in Table 5.7 show that the noise level indeed influences the accuracy of the results, but did not prevent successful diagnostics in most cases. The presence of noise affects the

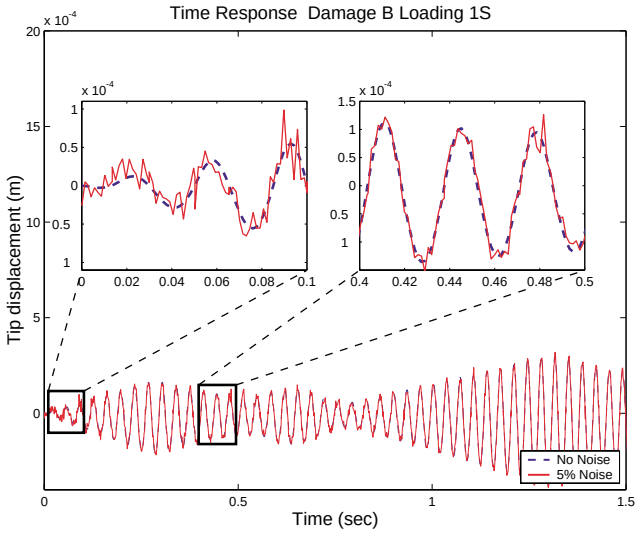

Figure 5.7: Time responses to first Schröeder excitation. Damage case B.

minimum crack size that can be identified, from $a/2d = 0.01$ for the case without noise, up to $a/2d = 0.04$ for 5% noise level. Figure 5.7 depicts time responses for case B1S and 5% noise level. Careful measurements are likely to produce time records of better quality than the one in Figure 5.7, and therefore noise levels above 5% were not tested . The results also show that the use of responses from the 3 Schröeder inputs provide slightly better results in the presence of noise, as can be seen from the tests with 2% and 5% noise levels. Figure 5.4.6 illustrates the diagnostic results for damage case L without noise and with 5% noise. All cracks larger than 5% of the beam depth were correctly identified for all noise levels.

5.4.5 Influence of Nonlinearities

The time responses computed in Chapter 4 show that the crack model used strongly influences the results. More specifically, the linear, open crack model produces larger deviations from the responses of the undamaged structure than the breathing-crack model. This indicates that the inclusion of the nonlinearities has the potential of improving the diagnostic results, and this is quantified in this section. Table 5.8 presents the comparison of identification results for selected damage cases using linear and nonlinear models. The omission

Table 5.7: Effect of noise on minimum identifiable crack for loading cases 2S and 3S.

Noise	0%				1%			
Load	2S		3S		2S		3S	
Damage	x_c/L	$a/2d$	x_c/L	$a/2d$	x_c/L	$a/2d$	x_c/L	$a/2d$
I	0.1607	0.0111	0.1629	0.0115	0.2203	0.0133	0.2311	0.0116
% error	7.16	10.83	8.60	14.68	46.87	32.83	54.08	15.67
J	0.1461	0.0209	0.1375	0.0180	0.1374	0.0176	0.1417	0.0190
% error	-2.57	4.40	-8.32	-9.96	-8.39	-12.14	-5.50	-5.01
K	0.1259	0.0233	0.1375	0.0293	0.1402	0.0301	0.1632	0.0347
% error	-16.09	-22.38	-8.32	-2.19	-6.53	0.47	8.80	15.59
L	0.1683	0.0482	0.1365	0.0381	0.1285	0.0375	0.1411	0.0415
% error	12.18	20.55	-8.98	-4.65	-14.34	-6.28	-5.91	3.71
A	0.1483	0.0501	0.1612	0.0528	0.1498	0.0500	0.1546	0.0516
% error	-1.10	0.21	7.47	5.52	-0.16	-0.03	3.04	3.25
E	0.1442	0.0975	0.1402	0.0961	0.1459	0.0982	0.1528	0.0982
% error	-3.89	-2.48	-6.56	-3.93	-2.74	-1.78	1.89	-1.85
F	0.1481	0.2492	0.1630	0.2634	0.1490	0.2518	0.1602	0.2527
% error	-1.24	-0.32	8.69	5.37	-0.64	0.71	6.79	1.10
B	0.1626	0.5088	0.1627	0.5115	0.1465	0.5002	0.1627	0.5119
% error	8.43	1.77	8.46	2.29	-2.35	0.04	8.46	2.37

Noise	2%				5%			
Load	2S		3S		2S		3S	
Damage	x_c/L	$a/2d$	x_c/L	$a/2d$	x_c/L	$a/2d$	x_c/L	$a/2d$
I	0.2607	0.0158	0.2301	0.0115	0.2660	0.0210	0.2535	0.0134
% error	73.77	57.73	53.40	14.68	77.31	110.41	68.99	34.21
J	0.1372	0.0158	0.1367	0.0184	0.1231	0.0162	0.1595	0.0168
% error	-8.50	-21.12	-8.86	-7.83	-17.97	-18.91	6.34	-15.96
K	0.1491	0.0324	0.1560	0.0320	0.1431	0.0319	0.1812	0.0398
% error	-0.63	8.13	3.99	6.73	-4.58	6.42	20.77	32.74
L	0.1174	0.0358	0.1313	0.0378	0.3417	0.0697	0.1222	0.0443
% error	-21.74	-10.38	-12.45	-5.53	127.82	74.20	-18.56	10.71
A	0.1420	0.0460	0.1545	0.0513	0.1491	0.0470	0.1560	0.0502
% error	-5.30	-7.92	3.02	2.60	-0.63	-5.98	4.01	0.48
E	0.1402	0.0952	0.1519	0.0982	0.1304	0.0925	0.1516	0.1039
% error	-6.54	-4.78	1.24	-1.78	-13.04	-7.51	1.04	3.94
F	0.1482	0.2519	0.1617	0.2590	0.1520	0.2581	0.1609	0.2504
% error	-1.17	0.76	7.80	3.59	1.35	3.25	7.28	0.15
B	0.1498	0.5034	0.1627	0.5119	0.1527	0.5049	0.1618	0.5077
% error	-0.15	0.68	8.46	2.37	1.82	0.97	7.86	1.54

of nonlinear effects results in poorer identification for all cases studied. The crack position obtained from the open crack model does not vary significantly for cracks of moderate to large depths when compared with the breathing crack results, and are even incidentally better in some cases. However, the more important result is the consistent identification of smaller crack depths, which means that the use of a linear model leads to underestimations of the severity of damage. Figure 5.4.6 illustrates the identification results for a crack of 10% depth. One could intuitively expect that the differences in diagnostics using a linear or a nonlinear model would be less pronounced for small cracks, but the identification results indicate otherwise. In fact, the error in crack depth increases as $a/2d$ decreases from 50% to 3%, and although some improvement seems to occur for smaller cracks (%1 and 2%), a much larger error in location is also present in those cases.

Table 5.8: Influence of nonlinearity on identification results.

Model	Open Crack (linear)				Breathing Crack (nonlinear)			
Case	x_c/L	error (%)	$a/2d$	error (%)	x_c/L	error (%)	$a/2d$	error (%)
I3S	0.2181	45.43	0.0065	-34.57	0.1629	8.60	0.0115	14.68
J3S	0.1730	15.33	0.0114	-43.22	0.1375	-8.32	0.0180	-9.96
K3S	0.1361	-9.24	0.0149	-50.45	0.1375	-8.32	0.0293	-2.19
L3S	0.1414	-5.73	0.0207	-48.33	0.1365	-8.98	0.0381	-4.65
A3S	0.1661	10.73	0.0291	-41.72	0.1612	7.47	0.0528	5.52
E3S	0.1478	-1.47	0.0588	-41.24	0.1402	-6.56	0.0961	-3.93
F3S	0.1556	3.75	0.1657	-33.70	0.1630	8.69	0.2634	5.37
B3S	0.1593	6.18	0.3863	-22.74	0.1627	8.46	0.5115	2.29

5.4.6 Effect of Model Uncertainties

The use of a good numerical model is an obvious pre-requisite for the application of any model-based, damage detection methods. Model updating methods currently available can

greatly improve the accuracy of the analytical model in reproducing the experimental behavior of structural systems. For the time domain method proposed in Reference [12], Banks et al. apply a model updating step prior to the damage diagnostic procedure in order to fine tune the mass and stiffness properties, resulting in a numerical model that reproduces the first three natural frequencies of the undamaged structure with very good accuracy. In Reference [100], Shen and Pierre show that the Euler-Bernoulli model accurately predicts the relative changes in natural frequencies up to the third mode of a beam with same aspect ratio as the one in the present simulations, $L/2d = 10$. This could relax the requirements for model accuracy in frequency domain methods, but might not be recommended when time responses are used. To investigate the robustness of the proposed methodology to modelling errors, two sources of uncertainty are considered:

- Uncertainties due to the use of the Euler-Bernoulli model instead of the Timoshenko-theory model;
- Uncertainties in the damping coefficients, usually very difficult to estimate and susceptible to large variations due to environmental conditions.

In the first case, a modified version of the objective function was also used in addition to the one defined in Equation (5.1). The proposed modified cost function is built from differences of time responses from the damaged and intact beam as

$$\bar{\mathbf{J}}(a, x_c) = \sum_{i=1}^{N_m} c_i \sum_{k=1}^{N_t} \left| \left(w_i^{(x)}(t_k) - \bar{w}_i^{(x)}(t_k) \right) - \left(w_i^{(n)}(t_k) - \bar{w}_i^{(n)}(t_k) \right) \right|^2, \tag{5.16}$$

where the barred quantities are measured or calculated from the undamaged structure. The idea behind this modified cost function is similar to the use of relative changes in natural frequency methods, i.e., by using the differences between damaged and undamaged data one might expect that only the changes due to the presence of damage would be taken into account and the model uncertainties would be left out of the diagnostic.

Table 5.9 compares the identification results using Shen's model with the ones obtained with the Timoshenko model. The diagnostics using the E-B model are inaccurate both in terms of crack location and depth when **J** is used. The use of the modified cost function $\bar{\mathbf{J}}$ improved the diagnostic significantly, producing results similar to the ones obtained with the Timoshenko model. However, when the modified fitness function is applied to responses contaminated with 2% noise, the results obtained with the two models deteriorate, as shown in Table 5.10 and illustrated by Figures 5.10 and 5.11. This indicates that the cost function based on differences is much more sensitive to the presence of noise and might lead to erroneous diagnostics in practical cases. For the investigations on damping uncertainties, only fitness function **J**, Eq. (5.1) is used.

Table 5.9: Comparison between diagnostic results using the Euler-Bernoulli and Timoshenko model with fitness funtions **J** and $\bar{\mathbf{J}}$. No noise added.

	Euler, **J**		Euler, $\bar{\mathbf{J}}$		Timoshenko, **J**		Timoshenko, $\bar{\mathbf{J}}$	
Case	x_c/L	$a/2d$	x_c/L	$a/2d$	x_c/L	$a/2d$	x_c/L	$a/2d$
A3S	0.6958	0.4450	0.1785	0.0517	0.1612	0.0527	0.1459	0.0483
% error	339	790	19.0	3.40	7.47	5.40	-2.73	-3.40
E3S	0.7021	0.4521	0.1870	0.1051	0.1402	0.0961	0.1514	0.0894
% error	368	352	24.7	5.1	-6.56	-3.93	0.93	-10.6
F3S	0.6751	0.4497	0.1765	0.2878	0.1630	0.2634	0.1609	0.2535
% error	350	79.9	17.7	15.1	8.69	5.37	7.27	1.40
B3S	0.1095	0.4927	0.1691	0.5190	0.1623	0.5115	0.1625	0.5063
% error	-27.0	-1.46	12.7	3.8	8.20	2.30	8.33	1.26

Table 5.10 describes the different combinations of uncertainties in damping coefficient investigated. Since damping coefficients are usually the physical parameters more difficult to estimate and more susceptible to variations due to changes in environmental conditions, the cases studied simulate large errors in the values of c_D and γ. The maximum value of c_D was chosen such that only underdamped modes were used in the calculation of the responses.

Table 5.10: Comparison between diagnostic results using the Euler-Bernoulli and Timoshenko model with fitness funtions $\mathbf{J}$ and $\bar{\mathbf{J}}$. Noise level: 2%.

	Euler, $\mathbf{J}$		Euler, $\bar{\mathbf{J}}$		Timoshenko, $\mathbf{J}$		Timoshenko, $\bar{\mathbf{J}}$	
Case	x_c/L	$a/2d$	x_c/L	$a/2d$	x_c/L	$a/2d$	x_c/L	$a/2d$
A3S	0.6958	0.4450	0.9409	0.4512	0.1545	0.0513	0.2326	0.1032
% error	339	790	527	802	3.00	2.60	55.1	106
E3S	0.7021	0.4521	0.1328	0.0854	0.1519	0.0982	0.2021	0.0808
% error	368	352	-11.5	-14.6	1.27	-1.80	34.7	-19.2
F3S	0.6799	0.4543	0.1564	0.2312	0.1617	0.2590	0.2259	0.2356
% error	353	81.7	4.27	-7.52	7.80	3.60	50.6	-5.7
B3S	0.1096	0.4951	0.1657	0.5260	0.1627	0.5119	0.1642	0.5256
% error	-26.9	-0.98	10.5	5.20	8.46	2.38	9.47	5.12

The identification results are presented in Table 5.11. The uncertainties in the air damping coefficient γ did not affect the results significantly even for an overestimation of one order of magnitude. This was somewhat expected, since the contributions of Kevin-Voight damping to the total system damping are much larger. When the effect of errors in c_D are studied, cracks as small as 5% depth were still correctly identified for model errors of -50% and 100%. When the damping was underestimated by one order of magnitude, a 10% crack depth was still identifiable. Overestimation of one order of magnitude in c_D, however, produced much worse results and no consistent identification was possible.

Table 5.11: Damping coefficients for model uncertainty investigations.

	Damping Case				
Coefficient	D1	D2	D3	D4	D5
Kevin-Voight damping	$c_D/2$	$c_D * 2$	c_D	$c_D/10$	$c_D * 10$
Air (viscous) damping	γ	γ	$\gamma * 10$	γ	γ

Table 5.12: Effect of uncertainties in model damping coefficients on diagnostics

Damping	D1		D2		D3		D4		D5	
Damage	x_c/L	$a/2d$	x_c/L	$a/2d$	x_c/L	$a/2d$	x_c/L	$a/2d$	x_c/L	$a/2d$
I3S	0.4759	0.0459	0.8280	0.1321	0.1629	0.0115	0.4329	0.0775	0.4241	0.1235
% error	217.3	358.5	452.0	1221	8.60	14.68	188.6	675.4	182.8	1135
J3S	0.4325	0.0557	0.8746	0.1772	0.1386	0.0180	0.4325	0.0690	0.4219	0.1273
% error	188.4	178.7	483.1	786.1	-7.60	-9.90	188.3	245.2	181.3	536.7
K3S	0.4546	0.0526	0.3007	0.0523	0.1398	0.0284	0.4329	0.0885	0.4207	0.1518
% error	203.0	75.26	100.5	74.47	-6.79	-5.18	188.6	194.9	180.5	405.9
L3S	0.4326	0.0586	0.2532	0.0626	0.1365	0.0380	0.4329	0.0845	0.4191	0.1568
% error	188.4	46.39	68.78	56.41	-8.98	-5.07	188.6	111.4	179.4	292.0
A3S	0.1586	0.0528	0.1342	0.0520	0.1521	0.0511	0.4328	0.0857	0.4207	0.1664
% error	5.75	5.50	-10.51	3.92	1.41	2.25	188.5	71.41	180.5	232.8
E3S	0.1409	0.0971	0.1357	0.0982	0.1396	0.0974	0.1423	0.1011	0.0569	0.1020
% error	-6.07	-2.85	-9.55	-1.77	-6.91	-2.62	-5.10	1.14	-62.10	2.00
F3S	0.1523	0.2491	0.1507	0.2538	0.1615	0.2560	0.1412	0.2503	0.1006	0.2523
% error	1.54	-0.36	0.48	1.50	7.69	2.42	-5.84	0.13	-32.94	0.93
B3S	0.1391	0.4912	0.1517	0.5062	0.1627	0.5120	0.1354	0.4917	0.1267	0.5089
% error	-7.28	-1.77	1.14	1.24	8.46	2.40	-9.71	-1.65	-15.53	1.79

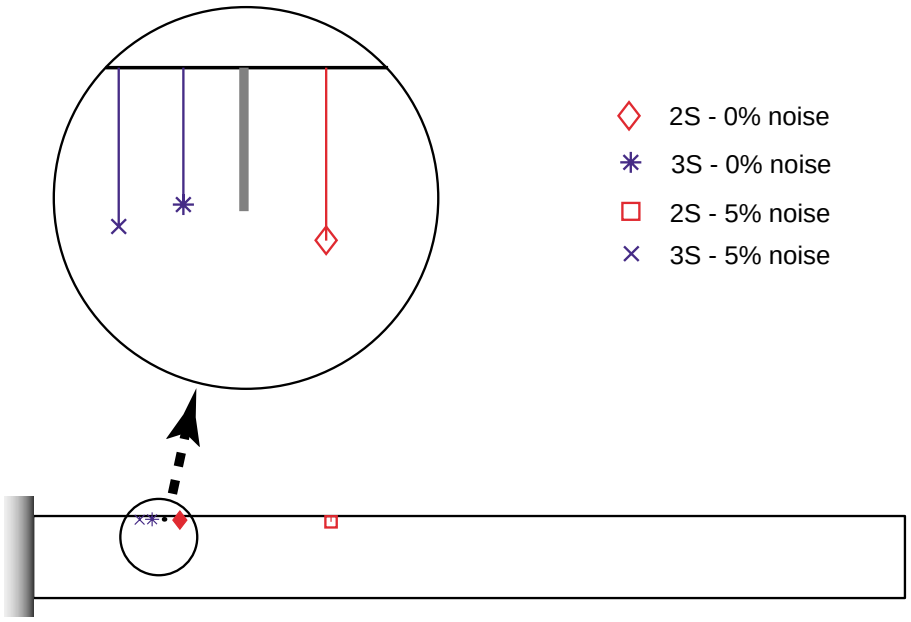

Figure 5.8: Effect of noise on diagnostic results. Damage case L ($x_c/L = 0.15$, $a/2d = 0.04$). Loading cases 2S and 3S.

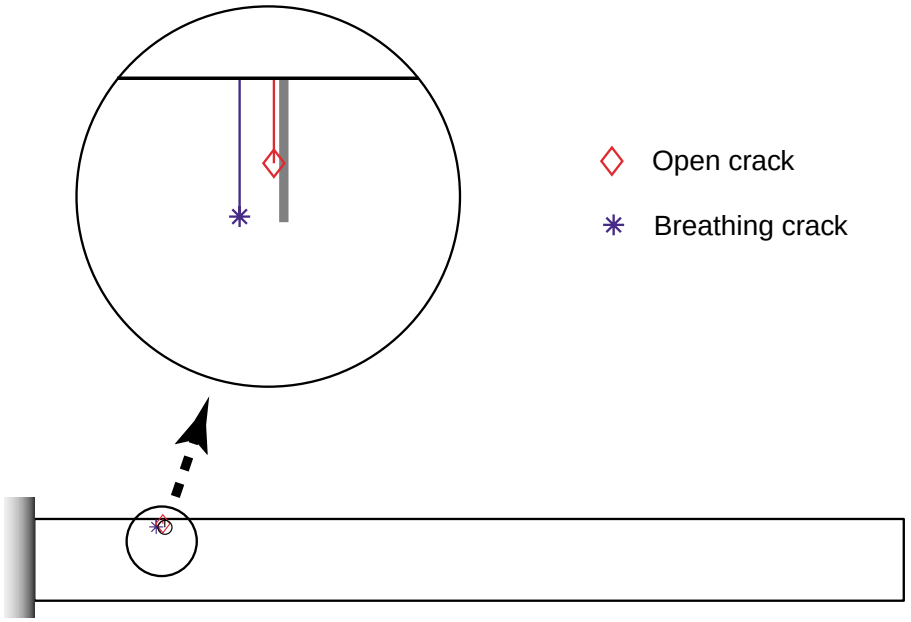

Figure 5.9: Comparison of diagnostic results using the open crack model and the breathing crack model. Damage case L ($x_c/L = 0.15$, $a/2d = 0.1$). Loading case 3S.

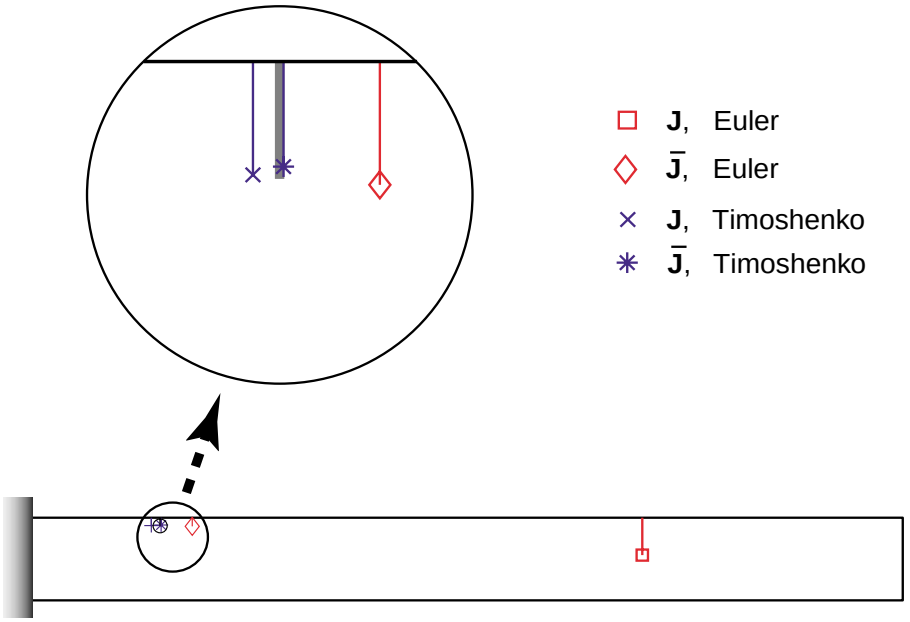

Figure 5.10: Comparison of diagnostic results using the Euler Bernoulli model and the Timoshenko model with fitness functions $\mathbf{J}$ and $\bar{\mathbf{J}}$. Damage case L ($x_c/L = 0.15$, $a/2d = 0.1$). Loading case 3S, no noise added.

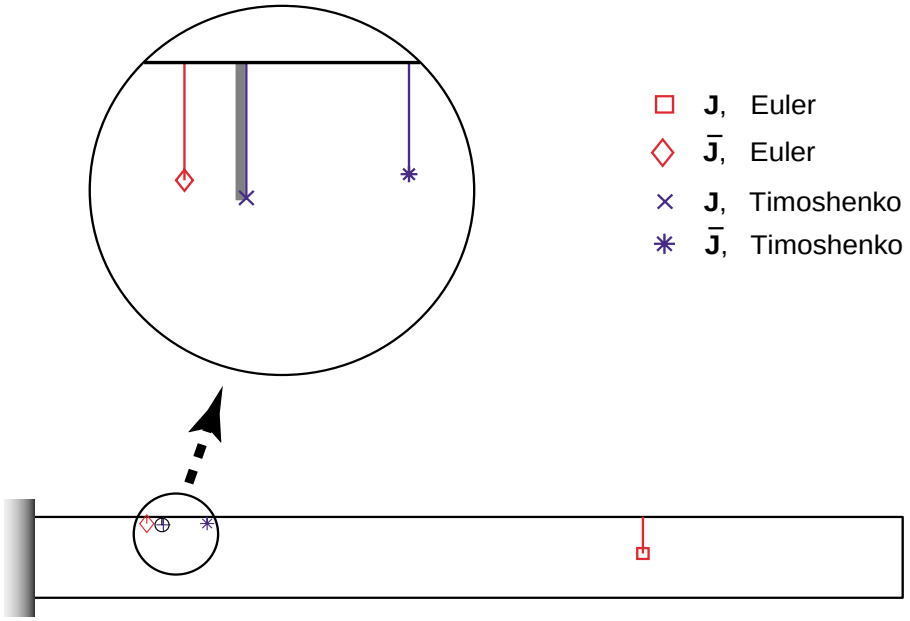

Figure 5.11: Comparison of diagnostic results using the Euler Bernoulli model and the Timoshenko model with fitness functions $\mathbf{J}$ and $\bar{\mathbf{J}}$. Damage case L ($x_c/L = 0.15$, $a/2d = 0.1$). Loading case 3S, noise level 5%.

Chapter 6

Conclusions, Contributions and Future Work

6.1 Conclusions

The overall objective of this work was the investigation of a time-domain, model-based damage diagnostic methodology applied to cracked beams. Most of the methods developed to date are based on frequency domain information such as frequency response functions (FRF's) and modal parameters. The use of time domain records minimizes the loss of information due to the data reduction involved in frequency domain methods and permit a straightforward treatment of the nonlinear behavior of cracked structural members. The results of this work are summarized according to the subgoals defined in Section 1.5.

1. Extension of Banks and Inman's method to crack problems;
2. Derivation of a continuous cracked beam model including shear deformation;
3. Addition of a genetic algorithm to tackle the multimodal nature of the objective function defined in the identification problem;

4. Comparison of excitation methods for the generation of the time responses;
5. Quantification of the advantages and limitations of the method by investigating the effects of
    - presence of noise;
    - inclusion of nonlinearities in the model;
    - use of the Timoshenko model versus the Euler-Bernoulli model;
    - uncertainties in physical parameters.

Item 1

The identification proposed by Banks and Inman is based on a model of the damaged structure in terms of partial differential equations (PDE's) with varying coefficients due to a geometric representation of the flaw. They validated the method for beams with small circular holes and suggested similar implementations for other damage geometries. The application of this idea to cracks, as reported in References [11, 10] was based on a representation of the damage by rectangular slots in a bi-dimensional plate models and were applied successfully only to structures with relatively wide cuts. Preliminary investigations in the present work attempted to model cracks as very narrow slots. This required extremely refined discretizations and, even when convergence was achieved, the results did not correlate well to experimental and numerical data from the literature. The geometric representation of flaws was abandoned and replaced by continuous cracked models. The selected models preserved the idea of representing damaged structures in terms of PDE's with varying coefficients, which now were obtained from a mixed variational formulation. The same B-spline Galerkin discretization could be readily applied, preserving the mathematical framework that guarantees the well-posedeness of the inverse problem. The next step in the extension of Banks' method to crack problems was the inclusion of the nonlinear crack-breathing feature to the numerical model. This was achieved by a bilinear representation of the stiffness operator

controlled by the sign of the normal strain at the cracked region. The implementation of the proposed extension led to the results discussed in more details in the following items.

Item 2

The first choice to replace the geometrical description of flaws used in Banks' and Inman's method was the continuous cracked beam model developed by Shen and Pierre [100]. The family of continuous models are derived from a mixed variational formulation that permits the assumption of independent stress, strain and displacement field, allowing for an approximate representation of the stress concentration due to the crack. Initial implementations of the model occasionally generated complex eigenvalues from the real mass and stiffness matrix resulting from the discretization of the PDE's. The source of the problem was the lack of symmetry in the stiffness matrix, which in turn was linked to the non-self-adjointness of the differential stiffness operator. The mathematical inconsistency was identified and a solution was proposed, as derived in Appendix A.

The proposed identification methodology requires the excitation of several modes of the structure to provide accurate diagnostics. This would limit the use of Shen's model to slender beams, since it is based on the Euler-Bernoulli (E-B) theory. To permit the application of the method to short beam-like structures, a new continuous cracked beam model was developed, including the effects of shear deformations and rotatory inertia. A shear stress/strain disturbance function was proposed in addition to the normal stress and axial displacement functions in Shen's model. The derivation resulted in the coupled PDE's in Section 3.4.5, which reduce to the Timoshenko model when no crack is present, and for that reason the model is referred to as Timoshenko cracked beam model.

When implementing the E-B and Timoshenko model for validation, a second limitation of Shen's model was revealed. Due to the steep nature of the displacement disturbance function, the numerical calculation of the stiffness matrix demanded very small integration steps to provide the necessary accuracy. The results in section 4.3.2 demonstrate that very little is

gained from the inclusion of the displacement function in the Timoshenko model. Almost identical results are produced with and without g when the integration precision is increased. When a less strict but still adequate precision is used, the results from the model including g present large numerical errors, whereas the model without g consistently reproduces the results from the more refined case. The displacement disturbance function was therefore disregarded for the remaining calculations.

The resulting PDE's of the cracked Timoshenko model were validated via comparisons of natural frequencies in open-crack state. The results show very good agreement with both FEM and experimental results found in the literature for the case of slender beams. The E-B and Timoshenko models produce very similar curves of relative natural frequency variations (normalized by the corresponding "undamaged" value), but the actual values differ significantly even for second and third natural frequencies of long beams. Mode shapes were also calculated and proved to be fairly insensitive to the presence of a crack. In a more detailed study of the effects of aspect ratio $AR = L/2d$, it was found that the differences in the variation of natural frequencies of cracked beams with respect to AR produced by the two models followed a trend very similar to the undamaged case, regardless of the crack depth. To confirm the better predictions of the cracked Timoshenko beam model, a short beam was modeled by 2–D finite elements in a mesh typical of fracture mechanics applications and the results were compared with both beam models. The Timoshenko model produced much better results than the E-B model, especially for frequencies above the first natural mode. This is particularly important for the accurate computation of time responses due to excitations in relatively higher frequencies, even when dealing with slender beams.

Item 3

Genetic algorithms (GA's) have recently become a powerful tool to solve complex optimization problems. The solution of the identification problem involves the minimization of a function defined from an appropriate measure of the "distance" between numerical and ex-

perimental data. This cost function usually presents multiple minima, a known difficulty for the more popular gradient-based minimization techniques. The proposed time-domain method introduces an extra complexity related to record length of the time responses, as discussed in Section 5.1. It was demonstrated that relatively long time records can artificially introduce numerous local minima and render a narrower global minimum. On the other hand, time records too short would not reveal the presence of damage. Preliminary attempts to identify damage using gradient based least squares estimations proved useless. The inclusion of GA's into the identification procedure was therefore a natural choice, since the principal strength of these algorithms is the ability to deal with multimodal objective functions. The results of the investigations in this work confirmed the adequacy of that choice. Due to the need of large initial populations, the computational cost in GA-based identifications is relatively high, but the intrinsic parallel nature of GA's can potentially reduce the computational time and provide fast diagnostics.

Item 4

The selection of the excitation method was addresses in section 5.4.3. The use of low frequency excitations and free vibration responses have both been suggested in the literature as good choices for a qualitative assessment of the presence of a crack by means of a spectral analysis. The time responses due to those excitations were investigated in the proposed time domain methodology to verify whether or not damage location and quantification could also be identified. The diagnostic results indicate that neither method can consistently provide accurate diagnosis. Multiple Schöeder-phased multisine inputs with designed bandwidths around the natural frequencies of the undamaged structure were shown to provide the best results. The inclusion of two and three responses produced similar results, but three excitations were shown to provide results that were less sensitive to the presence of noise.

Item 5

The robustness of the proposed methodology was verified by means of simulations of several damage scenarios in different uncertainty conditions, discussed in Sections 5.4.4 to 5.4.6. The main conclusions are summarized as follows.

Noise: Measurement of time responses are likely to include noise originated from several sources, such as electric equipment, spurious vibration sources, defective sensors, etc. Different levels of normal random noise were added to the simulated experimental records and the identification results were compared. The method proved robust to the presence of measurement noise; cracks as small as 2% of the beam depth were correctly identified even in the presence of 2% noise, and as small as 4% depth for 5% noise level.

Inclusion of nonlinearity: A very important result of this research is the quantification of the effect of nonlinearities on the diagnostic. It was demonstrated that the use of a linear model may produce very inaccurate results. For small cracks, both position and depth were erroneously identified. For crack depths above 3%, the damage location was accurately identified, but the crack depth was consistently underestimated, implying potentially unsafe diagnostics. The use of a linear model is therefore not recommended for crack diagnostics in the time domain.

E-B vs. Timoshenko model: The effect of model uncertainties due to the use of an E-B model instead of the Timoshenko model was also addressed. It was found that diagnostics with E-B model failed in all cases when the objective function proposed in Ref. [12] was used. A modified version of the cost function based on the differences between damaged and undamaged records was proposed in an attempt to factor out the model uncertainties. The identification results with the E-B showed very impressive improvement, but in general they were worse than the corresponding diagnostics with the Timoshenko model. However, the modified cost function proved considerably more sensitive to the presence of noise, and even previously successful identifications with the Timoshenko model and the original cost function could not be reproduced. In conclusion, the use of the E-B model requires modi-

fications that should only be applied when very clean measurements can be made. Despite the additional computational cost, the Timoshenko model is strongly recommended.

Damping uncertainties: The physical parameters more likely to present large uncertainties are the damping coefficients. Small variations in damping did not influence the results, and therefore simulations with errors of up to one order of magnitude in damping coefficients were performed. For -50% and 100% variations in the Kevin-Voight coefficient, cracks of 5% depth were still correctly quantified, but smaller cracks were completely misdiagnosed. Even with a damping coefficient one order of magnitude smaller than the correct value, a 10% depth crack was still detected. This robustness to changes in damping is a direct consequence of the use of forced response records, were the influences of damping are not as important as in free vibration responses.

6.2 Contributions

The mathematical derivations and numerical simulations in this research resulted in the following contributions:

- Extended Banks and Inman's time domain identification approach to the case of cracked structures by introducing a nonlinear model;
- Identified mathematical inconsistency in Shen's cracked Euler-Bernoulli model that renders a stiffness differential operator that is not self-adjoint and proposed corrections to the equations;
- Demonstrated numerical precision problems in Shen's model due to the steep nature of the crack displacement disturbance function and showed that the benefits on including it in the formulation are negligible;
- Developed a new cracked beam model that takes into account shear and rotatory inertia

effects and demonstrated, via FE simulations, the advantages of the new approach when modeling short beams;

- Revealed the effect of time record length on the multimodal nature of the objective function in the time-domain identification procedure and proposed the use of genetic algorithms to overcome those difficulties;
- Showed the advantages of using narrowband multisine excitations to generate the time responses and revealed the inadequacy of impact or low frequency sinusoidal inputs for time domain crack diagnostic;
- Demonstrated the importance of using the Timoshenko formulation and including the crack opening-closure behavior in the numerical model for the diagnostic procedure.

6.3 Future Work

The results of the present work indicate the following potential topics for future research:

- Incorporate disturbance functions for different cross-section geometries to the model;
- Extend the continuous cracked approach to plate-like structures;
- Investigate the possible benefits of using higher order stress/strain distributions in the representation of the disturbances caused by the presence of a crack;
- Develop a continuous model that captures the coupling between longitudinal, torsional and transverse vibrations reported by some authors and investigate the use of coupling effects for damage diagnostics;
- Include more elaborate damping models and investigate the potential use of damping parameters as damage indicators;

- Perform sensitivity analysis of the crack model with respect the decay parameters and investigate the possibility of computing those parameters directly from fracture mechanics expressions;
- Extend the proposed model to the case of multiple cracks and extend the identification methodology to deal with multisite damage cases;
- Incorporate statistical analysis to the identification procedure to address the problem of possible false positive and false negative diagnostics
- Investigate the importance of crack partial opening-closure;
- Investigate the inclusion of an offset strain level to the crack opening-closure switch in order to simulate the effects of permanent deformations at the crack tip region on the responses;
- Implement the proposed diagnostic technique experimentally in order to identify the possible limitations and propose modifications and/or improvements for the practical application of the method.

6.4 Closing Remarks

Despite the unquestionable advances in vibration-based damage detection methods in recent years, the state-of-the-art of this technology has not achieved real-life-application status. Very few industry-level solutions have been reported, such as qualitative nonlinear signature analysis in rotors [37] and the inspection of the space shuttle based on modal analysis [57]. Although in both cases only the presence of damage is identified (Level 1 diagnostic), those applications are a good example of the great potential of this new technology. The practical advantages of having reliable Level 2 and 3 diagnostics from easy-to-measure dynamic responses are still attracting the attention of the academic and scientific community, but many fundamental questions are yet to be answered. The development of new sensing technology

and the ever increasing computational power continue to open the doors to new approaches considered impractical just a few years ago, and will certainly affect the future research on vibration-based damage diagnostic. The present work addresses some of the issues that must be investigated, such as identification of small flaws, inclusion of nonlinearities, and existence of multiple local minima in the solution of the inverse problem, and proposes solutions that might help the pursuit for reliable technologies for monitoring structural integrity .

Bibliography

[1] Abdala, M., Grigoriadis, K., and Zimmerman, D. C. Lmi hybrid expansion-reduction damage detection method. In *Proceedings of the 18th International Modal Analysis Conference* (2000), pp. 1537–1542.

[2] Abraham, O. N. L., and Brandon, J. A. the modelling of the opening and closure of a crack. *Trans. ASME Journal of Vibrations and Acoustics 117* (July 1995), 370–377.

[3] Adams, R. D., Cawley, P., Pye, C. J., and Stone, B. J. A vibrational technique for non-destructively assessing the integrity of structures. *Journal of Mechanical Engineering Science 20* (1978), 93–100.

[4] Akgun, M., and Ju, F. D. Diagnosis of multiple cracks on a beam structure. *the International Journal of Analytical and Experimental Modal Analysis*, 2 (April 1987), 76–82.

[5] Araújo Gomes, A. J. M., and Montalvão e Silva, J. M. On the use of modal analysis for crack identification. In *Proceedings of the 8th International Modal Analysis Conference* (1990), pp. 1108–1115.

[6] Araújo Gomes, A. J. M., and Montalvão e Silva, J. M. Theoretical and experimental data on crack depth effects in the dynamic behavior of free-free beams. In *Proceedings of the 9th International Modal Analysis Conference* (1991), pp. 274–283.

[7] Armon, D., Ben-Haim, Y., and Braun, S. Crack detection in beams by rank-ordering of eigenfrequency shifts. *Mechanical Systems and Signal Processing 8*, 1 (1994), 81–91.

[8] Bäck, T., and Schwefel, H.-P. An overview of evolutionary algorithms for parameter optimization. *Evolutionary Computation 1*, 1 (1993), 1–23.

[9] Ballo, I. Non-linear effects of vibration of a continuous transverse cracked slender shaft. *Journal of Sound and Vibration 217*, 2 (1998), 321–333.

[10] Banks, H. T., and Emeric, P. Detection of non-symmetrical damage in smart plate-like structures. *Journal of Intelligent Material Systems and Structures 9* (October 1998), 818–828.

[11] Banks, H. T., Emeric, P., and Plancke, L. Modeling of non-symmetrical damage in plate-like structures. Tech. Rep. CRSC-TR97-12, Center for Research in Scientific Computation, North Carolina State University, 1997.

[12] Banks, H. T., Inman, D. J., Leo, D. J., and Wang, Y. An experimentally validated damage detection theory in smart structures. *Journal of Sound and Vibration 191*, 5 (1996), 859–880.

[13] Banks, H. T., and Kunisch, K. *Estimation Techniques for Distributed Parameter Systems*. Birkhäuser, 1989.

[14] Barr, A. D. S. An extension of the Hu-Washizu variational principle in linear elasticity for dynamic problems. *Trans. ASME J. Appl. Mechs. 33*, 2 (1966), 465.

[15] Brandon, J. A. Some insights into the dynamics of defective structures. *Proc. Istn Mech Engrs 212*, C (1998), 441–454.

[16] Brandon, J. A. Towards a nonlinear identification methodology for mechanical signature analysis. *Key Engineering Materials 167-168* (1999), 265–272.

[17] Brandon, J. A., and Abraham, O. N. L. Counter-intuitive quasi-periodic motion in the autonomous vibration of cracked Timoshenko beams. *Journal of Sound and Vibrations 185*, 3 (1995), 415–430.

[18] Carlin, R. A., and Garcia, E. Parameter optimization of a genetic algorithm for structural damage detection. In *Proceedings of the 14th International Modal Analysis Conference* (1996).

[19] Carneiro, S. H. S., and Inman, D. J. A continuous model of a cracked Timoshenko beam for damage detection. In *Proceedings of the 18th International Modal Analysis Conference* (February 2000), pp. 194–200.

[20] Cattarius, J., and Inman, D. J. Time domain analysis for damage detection in smart structures. *Mechanical Systems and Signal Processing 11*, 3 (1997), 409–423.

[21] Cawley, P., and Adams, R. D. the location of defects in structures from measurements of natural frequencies. *Journal of Strain Analysis 14*, 2 (1979), 49–57.

[22] Chance, J., Tomlinson, G. R., and Worden, K. A simplified approach to the numerical and experimental modeling of the dynamics of a cracked beam. In *Proceedings of the 12th International Modal Analysis Conference* (1994), pp. 778–785.

[23] Chang, F.-K., Ed. *Proceedings of the 1st International Workshop on Structural Health Monitoring* (September 1997).

[24] Chang, F.-K., Ed. *Proceedings of the 2nd International Workshop on Structural Health Monitoring* (September 1999).

[25] Changhe, L., Bernasconi, O., and Xenophontidis, N. A generalized approach to the dynamics of cracked shafts. *Journal of Vibration, Acoustics, Stress and Reliability in Design 111* (July 1989), 257–263.

[26] Chen, Y., and Swamidas, A. S. J. Modal updating for crack detection in plated t-joints. In *Proceedings of the 15th International Modal Analysis Conference* (1997), vol. 2, pp. 1332–1338.

[27] Chondros, T. G., and Dimarogonas, A. D. Vibrations of a cracked cantilever beam. *Trans. ASME Journal of Vibration, Acoustics 120* (July 1998).

[28] Chondros, T. G., Dimarogonas, A. D., and Yao, J. A continuous cracked beam vibration theory. *Journal of Sound and Vibration 215*, 1 (July 1998), 17–34.

[29] Chondros, T. G., Dimarogonas, A. D., and Yao, J. Longitudinal vibration of a bar with a breathing crack. *Engineering Fracture Mechanics 61* (1998), 503–518.

[30] Chondros, T. G., Dimarogonas, A. D., and Yao, J. Longitudinal vibration of a continuous cracked bar. *Engineering Fracture Mechanics 61* (1998), 593–606.

[31] Christides, S., and Barr, A. D. S. One-dimensional theory of cracked Bernoulli-Euler beams. *International Journal of Mechanical Sciences 26*, 11/12 (1984), 639–648.

[32] Christides, S., and Barr, A. D. S. Torsional vibration of cracked beams of non-circular cross-section. *International Journal of Mechanical Sciences 28* (1986), 473–490.

[33] Collins, K. R., Plaut, R. H., and Wauer, J. Detection of cracks in rotating timoshenko beams using axial impulses. *Journal of Vibration and Acoustics 113* (January 1991), 74–78.

[34] Collins, K. R., Plaut, R. H., and Wauer, J. Free and forced longitudinal vibrations of a cantilevered bar with a crack. *Journal of Vibration and Acoustics 114* (April 1992), 171–177.

[35] Cornwell, P., Doebling, S. W., and Farrar, C. R. Application of the strain energy damage detection method to plate-like structures. In *Proceedings of the 15th International Modal Analysis Conference* (1997), vol. 2, pp. 1312–1318.

[36] Dimarogonas, A. D. *Vibration Engineering.* West Publishers, 1976.

[37] Dimarogonas, A. D. Vibration of cracked structures: a state of the art review. *Engineering Fracture Mechanics 55*, 5 (1996), 831–857.

[38] Doebling, S. W., Farrar, C. R., and Prime, M. B. A summary review of vibration-based damage identification methods. *the Shock and Vibration Digest 30*, 2 (March 1998).

[39] Figueroa, M. B. G. Crack characterization using theoretical and experimental vibrations. Master's thesis, University of Puerto Rico, 1998.

[40] Friswell, M. I., and Penny, J. E. T. the practical limits of damage detection and location using vibration data. In *11th VPI&SU Symposium on Structural Dynamics and Control* (May 1997), pp. 31–40.

[41] Friswell, M. I., Penny, J. E. T., and Garvey, S. D. A combined genetic and eigensensitivity algorithm for the location of damage in structures. *Computers and Structures 69* (1998), 547–556.

[42] Friswell, M. I., Penny, J. E. T., and Wilson, D. A. L. Using vibration data and statistical measures to locate damage in structures. *the International Journal of Analytical and Experimental Modal Analysis 9*, 4 (October 1994), 239–254.

[43] Fritzen, C. P., Jennewein, D., and Kiefer, T. Damage detection based on vibration measurements and inaccurate models. In *Proceedings of DETC'97* (1997).

[44] Garcia, G. V., and Osegueda, R. Combining damage index method and arma method to improve damage detection. In *Proceedings of the 18th International Modal Analysis Conference* (2000), pp. 668–673.

[45] George, D., Hunter, N., Farrar, C., and Deen, R. Identifying damage sensitive features using nonlinear time-series and bispectral analysis. In *Proceedings of the 18th International Modal Analysis Conference* (2000), pp. 1537–1542.

[46] Goldberg, D. E. *Genetic Algorithms in Search, Optimization and Machine Learning.* Addison-Wesley, 1989.

[47] Gounaris, G., and Dimarogonas, A. D. A finite element of a cracked prismatic beam for structural analysis. *Computers and Structures 28*, 3 (1988), 309–313.

[48] Gudmundson, P. Eigenfrequency changes of structures due to cracks, notches or other geometrical changes. *J. Mech. Phys. Solids 30*, 5 (1982), 339–353.

[49] Gudmundson, P. the dynamic behavior of slender structures with cross-sectional cracks. *J. Mech. Phys. Solids 31*, 4 (1983), 329–345.

[50] Haisty, B. S., and Springer, W. T. A general beam element for use in damage assessment of complex structures. *Journal of Vibration, Acoustics, Stress and Reliability in Design 110* (July 1988), 389–394.

[51] Haupt, R. L., and Haupt, S. E. *Practical Genetic Algorithms.* John Wiley & Sons, 1998.

[52] Hibbit, Karlsson and Sorensen, Inc. *ABAQUS User's Manual, Version5.7.*

[53] Hoerst, B. C., and Ratcliffe, C. P. Damage detection in beams using laplacian operators on experimental modal data. In *Proceedings of the 15th International Modal Analysis Conference* (1997), pp. 1305–1311.

[54] Holand, J. H. *Adaptation in Natural and Artificial Systems.* University of Michigan Press, 1975.

[55] Houck, C. R., Joines, J. A., and Kay, M. G. A genetic algorithm for function optimization: a MATLAB implementation. Tech. Rep. NCSU-IE 95-09, North Carolina State University, 1995.

[56] Hu, H. *Variational Principles of Theory of Elasticity with Applications.* Gordon and Breach, 1984.

[57] Hunt, D. L., Dunlap, T. A., Weiss, S. P., and West, W. M. Development and implementation of a shuttle modal inspection system. In *Proceedings of the 8th International Modal Analysis Conference* (1900), pp. 919–925.

[58] Ibrahim, F. K. An elastoplastic cracked beam finite element for structural analysis. *Computers and Structures 49*, 6 (1993), 981–988.

[59] Inman, D. J. *Vibration with Control, Measurement and Stability*, 1 ed. Prentice Hall, Inc., 1989.

[60] Ismail, F., Ibrahim, A., and Martin, H. R. Identification of fatigue cracks from vibration testing. *Journal of Sound and Vibration 140*, 2 (1990), 305–317.

[61] Jones, R. L. A constitutive relationship between crack propagation and specific damping capacity in steel. Tech. Rep. N-1817, NCEL, October 1990.

[62] Kam, T. Y., and Lee, T. Y. Crack size identification using an expanded mode method. *International Journal of Solids and Structures 31*, 7 (1994), 925–940.

[63] Kim, H. M., and Bartkowicz, T. J. Damage detection and health monitoring of large space structures. *Journal of Sound and Vibration 27*, 6 (1993), 12–17.

[64] Kim, H. M., and Bartkowicz, T. J. A two-step structural damage detection approach with limited instrumentation. *Journal of Vibration and Acoustics 119* (April 1997), 258–264.

[65] Kirmser, P. G. the effect of discontinuities on the natural frequency of beams. In *Proceedings of the American Society of Testing and Materials* (1944), vol. 44, pp. 897–904.

[66] Larson, C., and Zimmerman, D. C. The effect of coding on genetic algorithm based structural damage detection. In *Proceedings of the 11th International Modal Analysis Conference* (1993), vol. 2, pp. 1095–1101.

[67] Lopes Jr., V., Pereira, J. A., and Weber, H. I. Using model updating technique to train neural network for fault detection. In *Proceedings of DETC'97* (1997).

[68] Lopez, F. P., and Zimmerman, D. C. Evaluation of reduced models for damage localization using subspace recognition. In *Proceedings of the 18th International Modal Analysis Conference* (2000), pp. 1200–1206.

[69] Luo, H., and Hanagud, S. Dynamic learning rate neural network training and composite structural damage detection. *AIAA Journal 35*, 9 (1997), 1522–1527.

[70] Mahmoud, M. A., and Kiefa, M. A. A. Neural network solution of the inverse vibration problem. *NDT & E International 32* (1999), 91–99.

[71] Mannan, M. A., and Richardson, M. H. Detection and location of structural cracks using FRF measurements. In *Proceedings of the 8th International Modal Analysis Conference* (1990), vol. 1, pp. 652–657.

[72] Mares, C., and Surace, C. An application of genetic algorithms to identify damage in elastic structures. *Journal of Sund and Vibration 195*, 2 (1996), 195–215.

[73] Masri, S. F., Nakamura, M., Chassiakos, A. G., and Caughey, T. K. Neural network approach to detection of changes in structural parameters. *Journal of Engineering Mechanics* (April 1996), 350–360.

[74] Meirovitch, L. *Principles and Techniques of Vibrations.* Prentice Hall, 1997.

[75] Michalewicz, Z. *Genetic Algorithms + Data Structures = Evolutionary Programs*, 3rd ed. Springer, 1995.

[76] Muñoz, A., Martorell, S., and Serradel, V. Genetic algorithms in optimizing surveillance and maintenance of components. *Reliability Engineering and System Safety 57* (1997), 107–120.

[77] Ostachowicz, W. M., and Krawczuk, M. Vibration analysis of a cracked beam. *Computers and Structures 36*, 2 (1990), 245–250.

[78] Ostachowicz, W. M., and Krawczuk, M. Analysis of the effect of cracks on the natural frequency of a cantilever beam. *Journal of Sound and Vibration 150*, 2 (1991), 191–201.

[79] Pandey, A. K., and Biswas, M. Experimental verification of the flexibility difference method for locating damage in structures. *Journal of Sound and Vibration 184*, 2 (1995), 311–328.

[80] Pandey, A. K., Biswas, M., and Samman, M. M. Damage detection from changes in curvature mode shapes. *Journal of Sound and Vibration 145*, 2 (1991), 321–332.

[81] Papadopoulos, C. A., and Dimarogonas, A. D. Coupled longitudinal and bending vibration of a rotation shaft with an open crack. *Journal of Sound and Vibration 117* (1986), 81–93.

[82] Pappa, R. S., Doebling, S. W., and Kholwad, T. On-line database of vibration-based damage detection experiments. In *Proceedings of the 18th International Modal Analysis Conference* (2000), pp. 1179–1185.

[83] Perchard, D. R., and Swamidas, A. S. J. Crack detection in slender cantilever plates using modal analysis. In *Proceedings of the 17th International Modal Analysis Conference* (1999), pp. 1769–1777.

[84] Plakhtienko, N. P., and Yasinskii, S. A. Resonance of second order in vibrations of a beam containing a transverse crack. *Strength of Materials 27*, 3 (1995), 146–152.

[85] Prenter, P. M. *Splines and Variational Methods*. John Wiley & Sons, 1975.

[86] Qian, G.-L., Gu, S.-N., and Jiang, J.-S. the dynamic behavior and crack detection of a beam with a crack. *Journal of Sound and Vibration 138*, 2 (1990), 233–243.

[87] Reddy, J. N. *Energy and Variational Methods in Applied Mechanics*. John Wiley & Sons, 1984.

[88] Rivola, A., and White, P. R. Bispectral analysis of the bilinear oscillator with application to the detection of fatigue cracks. *Journal of Sound and Vibration 216*, 5 (1998), 889–910.

[89] Rizos, P. F., Aspragathos, N., and Dimarogonas, A. D. Identification of crack location and magnitude in a cantilever beam from the vibration modes. *Journal of Sound and Vibration 138*, 3 (1990), 381–388.

[90] Ruotolo, R., and Surace, C. Damage assessment of multiple cracked beams: Numerical results and experimental validation. *Journal of Sound and Vibration 206*, 4 (1997), 567–588.

[91] Ruotolo, R., Surace, C., Crespo, P., and Storer, D. Harmonic analysis of the vibrations of a cantilevered beam with a closing crack. *Computer and Structures 61*, 6 (1996), 1057–1074.

[92] Rytter, A. *Vibration Based Inspection of Civil Engineering Structures*. PhD thesis, Aalborg University, Denmark, 1993.

[93] S. Seibold, S., and Weinert, K. A time domain method for the localization of cracks in rotors. *Journal of Sound and Vibration 195*, 1 (1996), 57–73.

[94] Salawu, O. S. Detection of structural damage through changes in frequency: a review. *Engineering Structures 19*, 9 (1997), 718–723.

[95] Sampaio, R. P. C. More insight into some frequency-response-function methods for damage detection. In *Proceedings of the 18th International Modal Analysis Conference* (2000), pp. 681–689.

[96] Schöeder, M. R. Synthesis of low peak-factor signals and binary sequences of low auto-correlation. *IEEE Trans. Information Theory 16* (January 1970), 85–89.

[97] Shames, I. H., and Clive, L. D. *Energy and Finite Element Methods in Structural Mechanics*, 1 ed. Taylor & Francis, 1985.

[98] Shen, M.-H. H. On-line structural damage detection. *Structronic Systems: Smart Structures, Devices and Systems, Part I 4* (1998), 271–332.

[99] Shen, M.-H. H., and Chu, Y. C. Vibrations of beams with a fatigue crack. *Computer and Structures 45*, 1 (1992), 79–93.

[100] Shen, M.-H. H., and Pierre, C. Natural modes of Bernoulli-Euler beams with symmetric cracks. *Journal of Sound and Vibration 138*, 1 (1990), 115–134.

[101] Shen, M.-H. H., and Pierre, C. Free vibrations of beams with a single edge crack. *Journal of Sound and Vibration 170*, 2 (1994), 237–259.

[102] Smith, S. W., Zimmerman, D. C., Bartkowicz, T. J., and Kim, H. M. Experiments for damage location in a damped structure. *Proc. DETC'97/ VIB-4231* (September 1997).

[103] Society for Experimental Mechanics, Ed. *15th International Modal Analysis Conference* (1997).

[104] Sohn, H., Fugate, M. L., and R., F. C. Continuous structural monitoring using statistical process control. In *Proceedings of the 18th International Modal Analysis Conference* (2000), pp. 660–667.

[105] SPIE, Ed. *Proceedings of SPIE Smart Materials and Structures Conference* (1997).

[106] Stubbs, N., Kim, J. T., and Farrar, C. R. Field verification of a nondestructive damage localization and sensitivity estimator algorithm. In *Proceedings of the 13th International Modal Analysis Conference* (1995), vol. 1, pp. 210–218.

[107] Stubbs, N., and Osegueda, R. Global damage detection in solids - experimental verification. *the International Journal of Analytical and Experimental Modal Analysis 5*, 2 (April 1990), 81–97.

[108] Stubbs, N., and Osegueda, R. Global nondestructive evaluation in solids. *the International Journal of Analytical and Experimental Modal Analysis 5*, 2 (April 1990), 67–79.

[109] Sundermeyer, J. N., and Weaver, R. L. On crack identification and characterization in a beam by non-linear vibration analysis. *Journal of Sound and Vibration 183*, 5 (1995), 857–871.

[110] Swamidas, A. S. J., and Chen, Y. Monitoring crack growth through change of modal parameters. *Journal of Sound and Vibration*, 2 (1995), 325–343.

[111] Swamidas, A. S. J., and Cheng, S. Detection of fatigue crack initiation and crack growth in tubular t-joints using modal analysis. In *Proceedings of the 15th International Modal Analysis Conference* (1997), vol. 2, pp. 1801–1807.

[112] Thomson, A. S. Vibration of slender bars with discontinuities in stiffness. *Journal of Applied Mechanics 17* (1949), 203–207.

[113] Tsai, T. C., and Wang, Y. Z. Vibration analysis and diagnosis of a cracked shaft. *Journal of Sound and Vibration 192*, 3 (1996), 607–620.

[114] Tsyfanskii, S. L., and Beresnevich, V. I. Vibrodiagnostics of fatigue cracks in flexible, geometrically nonlinear, beam- type structural elements. *Russian Journal of Nondestructive Testing 30*, 6 (1994), 427–433.

[115] Wang, Y. *Damping Modeling and Parameter Estimation in Timoshenko Beams*. PhD thesis, Brown University, 1991.

[116] Washizu, K. *Variational Methods in Elasticity and Plasticity*, second ed. Pergamon Press, 1975.

[117] Wauer, J. On the dynamics of cracked rotors: a literature survey. *Appl. Mech. Rev. 43*, 1 (January 1990), 13–17.

[118] West, W. M. Illustration of the use of modal assurance criterion to detect structural changes in an orbiter test specimen. In *Proceedings of the Air Force Conference on Aircraft Structural Integrity* (1984), pp. 1–6.

[119] Yam, L. H., Leung, T. P., Li, D. B., and Xue, K. Z. Theoretical and experimental study of modal strain analysis. *Journal of Sound and Vibration 191*, 2 (1996), 251–260.

[120] Yap, K. C., and Zimmerman, D. C. the effect of coding on genetic algorithm based structural damage detection. In *Proceedings of the 16th International Modal Analysis Conference* (1998), vol. 1, pp. 165–171.

[121] Yoo, S. H., Kwak, H. K., and Kim, B. S. Detection and location of a crack in a plate using modal analysis. In *Proceedings of the 17th International Modal Analysis Conference* (1999), vol. 2, pp. 1902–1908.

[122] Yuen, M. M. Numerical study of the eigenparameters of a damaged cantilever. *Journal of Sound and Vibration 103*, 3 (1985), 301–310.

[123] Zimmerman, D. C., and Kaouk, M. Structural damage detection using a minimum rank update theory. *Journal of Vibration and Acoustics 116* (1994), 222–230.

[124] Zimmerman, D. C., Kaouk, M., and Simmermacher, T. On the role of engineering insight and judgment structural damage detection. In *Proceedings of the 13th International Modal Analysis Conference* (1995), vol. 1, pp. 414–420.

Appendix A

Euler-Bernoulli Cracked Beam Models

A.1 Check of Self Adjointness of Shen's Model

The equations of motion derived in Ref. [100] are:

$$E(I_0 - I_1 - I_6 + I_7)Q_1 w^{(iv)} + E[2(I_0 - I_1 - I_6 + I_7)Q_1' + (2I_{10} + I_8 - I_6' - 2I_1')Q_1]w''' +$$

$$+E[(I_0 - I_1 - I_6 + I_7)Q_1'' + (2I_{10} + I_8 - I_6' - 2I_1')Q_1' + (I_{10}' - I_1'')Q_1]w'' + \rho A\ddot{w} = 0 \quad \text{(A.1)}$$

with the boundary conditions

$$\begin{aligned} E(I_0 - I_1 - I_6 + I_7)Q_1 w'' &= 0, \\ or \qquad\qquad w' &= 0\ ; \end{aligned} \quad \text{(A.2)}$$

and

$$\begin{aligned} E[(I_0 - I_1 - I_6 + I_7)(Q_1' w'' + Q_1 w''') + E(I_{10} - I_1')Q_1 w'' &= 0, \\ or \qquad\qquad w &= 0\ . \end{aligned} \quad \text{(A.3)}$$

were the definitions in Eqs.(3.39) and (3.42) still apply. The fourth order stiffness operator can be rewritten, for simplicity, as

$$\mathcal{L}w = E(p_4 w^{(iv)} + p_3 w''' + p_2 w'' + p_1 w' + p_0). \quad \text{(A.4)}$$

A fourth order differential operator with varying coefficients can only be self adjoint if it has the form

$$\frac{\partial^2}{\partial x^2}\left(q_2\frac{\partial^2}{\partial x^2}\right)+\frac{\partial}{\partial x}\left(q_1\frac{\partial}{\partial x}\right)+q_0. \tag{A.5}$$

Therefore, with the derived boundary conditions, $\mathcal{L}$ will be self adjoint if and only if we can write the correspondence

$$\begin{aligned} q_2 &= p_4, & 2q_2' &= p_3, & q_1+q_2'' &= p_2, \\ & & q_1' &= p_{1,} & q_0 &= p_0. \end{aligned} \tag{A.6}$$

Since $p_1 = 0$ and $p_0 = 0$ in Eq.(A.4), one must satisfy

$$p_3 = 2p_4', \tag{A.7}$$

$$p_2 = p_4'' + C, \tag{A.8}$$

where C is an arbitrary constant. The conditions in Eqns. (A.7) and (A.8) will only be satisfied if the displacement disturbance function $g(x,z)$ defined in Eq. (3.24) is identically zero. Therefore, we may conclude that the stiffness operator in Eq. (A.1) is in general *not* self-adjoint.

A.2 Proposed Correction

Start with the kinematic conditions in Eq. (3.75) and replace (3.75-a) with (3.77). The steps in the variational derivation can be summarized as follows.

Strain-Displacement Term

$$\int_V[\epsilon_{ij}-\frac{1}{2}(u_{i,j}+u_{j,i})]\delta\sigma_{ij}dV=\int_V\{[\epsilon_{xx}-\frac{\partial u_x}{\partial x}]\delta\sigma_{xx}=$$

$$=\int_V\{[(-z+f_1)S_1-(-z+g)w''-\frac{\partial g}{\partial x}w'](-z+f_1)\delta T_1\}dV=$$

$$= \int_V \{[z^2 S_1 - 2z f_1 S_1 + f_1^2 S_1 - z^2 w'' + z f_1 w'' + z g w'' + z g' w' - g f_1 w'' - g' f_1 w'] \delta T_1\} dV =$$

$$= \int_x \{[(I_0 - 2I_1 + I_2) S_1 - (I_0 - I_1 - I_6 + I_7) w'' - (I_8 - I_6') w'] \delta T_1\} dx \ , \qquad \text{(A.9)}$$

where the generalized inertia integrals are defined in Eq. (3.42).

Stress-Strain Term

$$\int_V (\sigma_{ij} - W_{,\epsilon_{ij}}) \delta \epsilon_{ij} dV = \int_V \{(\sigma_{xx} - W_{,\epsilon_{xx}}) \delta \epsilon_{xx}\} dV =$$

$$= \int_x \{(T_1 - E S_1)(I_0 - 2I_1 + I_2) \delta S_1\} dx. \qquad \text{(A.10)}$$

Velocity-Momentum Term

$$\int_V [\rho \dot{u}_i - (\frac{1}{2} \rho p_i p_i)_{,p_i}] \delta p_i dV =$$

$$\int_V \{[\rho \dot{w} - \rho P_z] \delta P_z\} dV. \qquad \text{(A.11)}$$

Dynamic Equilibrium Term

For zero body forces,

$$\int_V \{(\sigma_{ij,j} + B_i - \rho \dot{p}_i) \delta u_i\} dV =$$

$$\int_V \left\{ \left(\frac{\partial \sigma_{xx}}{\partial x} + \frac{\partial \sigma_{xz}}{\partial z} \right) (-z + g) \delta w' + \left(\frac{\partial \sigma_{xz}}{\partial x} - \rho \dot{P}_z \right) \delta w \right\} dV =$$

$$= \int_V \left\{ \left(\left((-z + f_1) T_1 \right)' + \frac{\partial \sigma_{xz}}{\partial z} \right) (-z + g) \delta w' + \left(\frac{\partial \sigma_{xz}}{\partial x} - \rho \dot{P}_z \right) \delta w \right\} dV. \qquad \text{(A.12)}$$

Integrate the terms in $\delta w'$ by parts and get

$$\int_{YZ} \left\{ \left(\left((-z + f_1) T_1 \right)' + \frac{\partial \sigma_{xz}}{\partial z} \right) (-z + g) \delta w \Big|_0^L \right\} dA -$$

$$- \int_V \left\{ \frac{\partial}{\partial x} \left[\left(\left((-z + f_1) T_1 \right)' + \frac{\partial \sigma_{xz}}{\partial z} \right) (-z + g) \right] + \left(\frac{\partial \sigma_{xz}}{\partial x} - \rho \dot{P}_z \right) \right\} \delta w dV \qquad \text{(A.13)}$$

Integrate the terms in T_1 in the volume integral in (A.13) over the cross section, plug into Eq. A.12 and get the dynamic equilibrium term expressed as

$$\int_{YZ}\left\{\left(\left(\left(-z+f_1\right)T_1\right)'+\frac{\partial\sigma_{xz}}{\partial z}\right)(-z+g)\delta w\Big|_0^L\right\}dA-\int_V\left\{\frac{\partial}{\partial x}\left[(-z+g)\frac{\partial\sigma_{xz}}{\partial z}\right]+\frac{\partial\sigma_{xz}}{\partial x}\right\}\delta w dV$$
$$-\int_X\left\{\left[(I_0-I_1-I_6+I_7)T_1^{''}+(2I_{10}+I_8-I_6'-2I_1')T_1^{'}+(I_{10}'-I_1'')T_1\right]+\rho A\ddot{P}_z\right\}\delta w dx \tag{A.14}$$

The boundary term and the terms in σ_{xz} in expression A.14 will be used in the derivation of the boundary conditions.

Boundary Integrals - Prescribed Forces

The lateral surfaces of the beam are assumed to be traction-free, i.e., $\bar{g}_i = 0$. Over the surfaces $z = \pm d$, the tractions are defined by $g_i = \sigma_{ij}n_j$ and result in $g_x = \pm\sigma_{xz}$ and $g_y = g_z = 0$. This implies that the shear stress distribution, which is not relevant for the derivation, must vanish at the surfaces. The term is kept in the boundary integral to permit further simplifications and a consistent derivation of the boundary conditions.

The boundary integral over the lateral surfaces will be part of $\mathcal{S}_1$ and can be written as

$$\left[\int_{XY}\left\{(\overline{g_x}-g_x)\delta u_x\right\}dA\right]_{z=d}+\left[\int_{XY}\left\{(\overline{g_x}-g_x)\delta u_x\right\}dA\right]_{z=-d}=$$
$$\left[\int_{XY}\left\{(-\sigma_{xz})(-z+g)\delta w'\right\}dA\right]_{z=d}+\left[\int_{XY}\left\{(\sigma_{xz})(-z+g)\delta w'\right\}dA\right]_{z=-d}$$
$$=\left[\int_{XY}\left\{(-\sigma_{xz})(-z+g)\delta w'\right\}dA\right]_{z=-d}^{z=d}$$

integrate by parts over x and get

$$\left[\int_Y\left\{(-\sigma_{xz})(-z+g)\delta w\right\}dy\right]_{z=-d}^{z=d}\Bigg|_{x=0}^{x=L}-\left[\int_{XY}\frac{\partial}{\partial x}\left\{(-\sigma_{xz})(-z+g)\right\}\delta w dA\right]_{z=-d}^{z=d}. \tag{A.15}$$

Now deal with the volume integral in expression (A.14). The term in square brackets can be integrated by parts over z as

$$-\int_V\frac{\partial}{\partial x}\left[(-z+g)\frac{\partial\sigma_{xz}}{\partial z}\right]\delta w dV=$$

$$= -\int_{XY} \frac{\partial}{\partial x} \left\{ [(-z+g)\sigma_{xz}]_{z=-d}^{z=d} \right\} \delta w dA + \int_V \frac{\partial}{\partial x} \left[(-1+\frac{\partial g}{\partial z})\sigma_{xz} \right] \delta w dV. \tag{A.16}$$

The first integral on the right-hand-side of Eq. (A.16) cancels the last integral in expression (A.15). The first term in the volume integral on the right-hand-side of Eq. (A.16) will cancel the last term of the volume integral in (A.14).

The last term of the boundary integral in (A.14) can also be integrated by parts over z yielding

$$\int_A \left\{ \left(\frac{\partial \sigma_{xz}}{\partial z} \right) (-z+g)\delta w \Big|_{x=0}^{L} \right\} dA =$$

$$= \left[\int_Y \{(\sigma_{xz})(-z+g)\delta w\}\, dy \right]_{z=-d}^{z=d} \Bigg|_{x=0}^{x=L} - \left[\int_A \left\{ (\sigma_{xz})(-1+\frac{\partial g}{\partial z})\delta w \right\} dA \right] \Bigg|_{x=0}^{x=L}. \tag{A.17}$$

The first integral on the right-hand-side of Eq. (A.17) cancels the first integral in expression (A.15). The last term inside the second integral on the right-hand-side of Eq. (A.17) cancels the corresponding term in the volume integral on the right-hand-side of Eq. (A.16) after integrating over x. All that is left from the boundary integrals in the dynamic equilibrium term, the terms in σ_{xz}, and from the lateral surface integrals are the first part in the boundary term of (A.14) and a term from the last integral in Eq. (A.17), i.e.,

$$\left[\int_{YZ} \left\{ \left((-z+f_1)\, T_1 \right)' (-z+g) + \sigma_{xz} \right\} \delta w dA \right]_{x=0}^{x=L}. \tag{A.18}$$

The end surfaces $x = 0$ and $x = L$ can be either part of $\mathcal{S}_1$ or $\mathcal{S}_2$. When tractions are prescribed, we have $g_x = \pm\sigma_{xx}$ and $g_z = \pm\sigma_{xz}$ and the end surfaces will produce the boundary integrals

$$\left[\int_{YZ} \{(\overline{g_x} - g_x)\delta u_x + (\overline{g_z} - g_z)\delta u_z\}\, dA \right]_{x=L} + \left[\int_{YZ} \{(\overline{g_x} - g_x)\delta u_x + (\overline{g_z} - g_z)\delta u_z\}\, dA \right]_{x=0} =$$

$$= \left[\int_{YZ} \{\overline{g_x} - ((-z+f_1)T_1)(-z+g)\delta w' + (\overline{g_z} - \sigma_{xz})\delta w\}\, dA \right]_{x=0}^{x=L}. \tag{A.19}$$

Combine (A.18) and (A.19) and finally get

$$\left[\left\{ \int_{YZ} \overline{g_x}(-z+g)dA - (I_0 - I_1 - I_6 + I_7)T_1 \right\} \delta w' \right]_{x=0}^{x=L} +$$

$$+ \left[\left\{ \int_{YZ} \overline{g_z} dA + (I_0 - I_1 - I_6 + I_7)T_1' + (I_{10} - I_1')T_1 \right\} \delta w \right]_{x=0}^{x=L}. \tag{A.20}$$

Boundary Integrals - Prescribed Displacements

When displacements are prescribed over the end surfafces $x = 0$ and $x = L$, we have

$$\left[\int_A \left\{\left(u_x - \overline{u_x}\right)\delta\sigma_{xx} + \left(u_z - \overline{u_z}\right)\delta\sigma_{xz}\right\} dA\right]_{x=L} +$$

$$\left[\int_A \left\{\left(u_x - \overline{u_x}\right)\delta\left(-\sigma_{xx}\right) + \left(u_z - \overline{u_z}\right)\delta\left(-\sigma_{xz}\right)\right\} dA\right]_{x=0} =$$

$$= \left[\int_A \left\{\left((-z+g)w' - \overline{u_x}\right)(-z+f_1)\delta T_1 + (w - \overline{u_z})\delta\sigma_{xz}\right\} dA\right]_{x=0}^{x=L} =$$

$$= \left[\left\{-\int_A \overline{u_x}(-z+f_1)dA + (I_0 - I_1 - I_6 + I_7)w'\right\}\delta T_1\right]_{x=0}^{x=L} + \left[\left\{A(w - \overline{u_z})\right\}\delta\sigma_{xz}\right]_{x=0}^{x=L}. \quad \text{(A.21)}$$

Differential Equation of Motion

Since δT_1, δS_1, δP_z, and δw are independent and arbitrary, each corresponding term in the integrals must independently be zero. Hence, Eqs. (A.9), (A.10) and (A.11) yields, respectively

$$S_1 = Q_1 w'' + Q_2 w' \,, \tag{A.22}$$

$$T_1 = E S_1 \,, \tag{A.23}$$

and

$$P_z = \dot{w}. \tag{A.24}$$

Performing all the necessary substitutions into expression (A.14) and taking into account Eqs. (A.22), (A.23) and (A.24), get

$$\int_x \left\{\left[(I_0 - I_1 - I_6 + I_7)E\frac{\partial^2}{\partial x^2}\left(Q_1 w'' + Q_2 w'\right) + (2I_{10} + I_8 - I_6' - 2I_1')E\frac{\partial}{\partial x}\left(Q_1 w'' + Q_2 w'\right) + \right.\right.$$

$$\left.\left. + \left(I_{10} - I_1'\right)\left(Q_1 w'' + Q_2 w'\right) + \rho A\ddot{w}\right]\delta w\right\} dx = 0,$$

Finally, considering that δw is arbitrary, obtain

$$E(I_0 - I_1 - I_6 + I_7)Q_1 w^{(iv)} + E[(I_0 - I_1 - I_6 + I_7)(2Q_1' + Q_2) + (2I_{10} + I_8 - I_6' - 2I_1')Q_1]w''' +$$

$$+ E[(I_0 - I_1 - I_6 + I_7)(Q_1'' + 2Q_2') + (2I_{10} + I_8 - I_6' - 2I_1')(Q_1' + Q_2) + (I_{10}' - I_1'')Q_1]w''$$

$$E[(I_0 - I_1 - I_6 + I_7)Q_2'' + (2I_{10} + I_8 - I_6' - 2I_1')Q_2' + (I_{10}' - I_1'')Q_2]w' + \rho A\ddot{w} = 0. \quad \text{(A.25)}$$

After some algebra, Equation (A.25) can be simplified and rewritten as

$$E[p_2(x)w(x,t)'']'' + E[p_1(x)w'(x,t))]' + \rho A\ddot{w}(x,t) = 0, \quad \text{(A.26)}$$

with

$$p_2(x) = (I_0 - I_1 - I_6 + I_7)Q_1(x), \quad \text{(A.27)}$$

$$p_1(x) = (I_0 - I_1 - I_6 + I_7)Q_2' + (I_{10}' - I_1'')Q_2. \quad \text{(A.28)}$$

Boundary Conditions

The boundary integrals in expressions (A.20) and (A.21) also have to be equal to zero. Therefore, the homogeneous boundary conditions for zero prescribed forces and/or displacements can be written as

$$\begin{aligned} E(I_0 - I_1 - I_6 + I_7)(Q_1 w'' + Q_2 w') &= 0 \\ \text{or} \qquad w' &= 0\,, \end{aligned} \quad \text{(A.29)}$$

and

$$\begin{aligned} E(I_0 - I_1 - I_6 + I_7)(Q_1 w''' + (Q_1' + Q_2)w'' + Q_2' w') + & \\ + \; E(I_{10} - I_1')(Q_1 w'' + Q_2 w') &= 0 \\ \text{or} \qquad w &= 0\,. \end{aligned} \quad \text{(A.30)}$$

Self-Adjointness

Since equation (A.26) is in the form required by Eq. (A.5), the operator can be integrated by parts and, using the BC's in Eq. (A.29) and (A.30), will automatically render a symmetric form. Therefore, we conclude that the stiffness operator is self-adjoint.

Appendix B

Cubic B-Spline Functions

B.1 Preliminary Remarks

The estimation of damage parameters from time responses belongs to a class of inverse problems that has been extensively investigated by Banks and co-workers at the Center for Research in Scientific Computation at North Carolina State University. Cubic splines are their usual choice for approximation schemes in PDE-based estimation problems for two main reasons. First, the polynomial forms permit very efficient numerical implementation; and second, they provide straightforward satisfaction of hypothesis in important theorems developed in the rigorous mathematical investigations of well-posedness and convergence of solutions to inverse problems [13].The following is a summary of the key equations defining the cubic b-splines used as test functions in the Galerkin method discussed in Chapter 4. Most of these definitions can be found in Ref.[13] or in the more detailed discussions of Ref. [85].

B.2 Mathematical Definitions

Let $s(x)$ be an approximation of the function $f(x) \in C^1(I)$ over the interval $I = [0,1]$. Define $\{\frac{i}{\hat{N}}\}_{i=0}^{\hat{N}}$ an equidistant partition of $[0,1]$. Let $S_3^{\hat{N}}$ be the linear space defined by

$$\begin{aligned} S_3^{\hat{N}}(I) &= \{s \in C^2(I) : s \text{ is a cubic polinomial on each} \\ &\qquad \text{subinterval } [x_i, x_{i+1}],\ 0 \le i < \hat{N}\ \}. \end{aligned}$$

One can prove that there is a unique function $s(x)$ in $S_3^{\hat{N}}(I)$ satisfying the $\hat{N}+3$ constraints

$$\begin{aligned} s'(0) &= f'(0), \\ s(i/\hat{N}) &= f(i/\hat{N}), \quad 0 \le i \le \hat{N}, \\ s'(1) &= f'(1). \end{aligned} \tag{B.1}$$

and such function is called the *cubic spline interpolate* to $f(x)$.

To construct $S_3^{\hat{N}}(I)$,define the basic piecewise cubic function over $[-2,2]$ as

$$B(x) = \begin{cases} (2-x)^3/24 - (1-x)^3/6 - x^3/4 + (1+x)^3/6 & \text{for} \quad -2 \le x \le -1 \\ (2-x)^3/24 - (1-x)^3/6 - x^3/4 & \text{for} \quad -1 \le x \le 0 \\ (2-x)^3/24 - (1-x)^3/6 & \text{for} \quad 0 \le x \le 1 \\ (2-x)^3/24 & \text{for} \quad 1 \le x \le 2 \\ 0 & \text{elsewere.} \end{cases} \tag{B.2}$$

Let $\mathcal{B}$ be the set of functions defined by

$$\mathcal{B} = \{\hat{b}_i(x) = B(\hat{N}x - i) \quad -1 \le i \le \hat{N}+1\}. \tag{B.3}$$

The functions $\hat{b}_i(x)$, illustrated in Figure B.1, are linearly independent in $[0,1]$. Moreover, it can be shown that $\mathcal{B}$ spans $S_3^{\hat{N}}(I)$. Therefore, $\mathcal{B}$ is a basis of $S_3^{\hat{N}}(I)$ and the linear space has dimension $\hat{N}+3$.

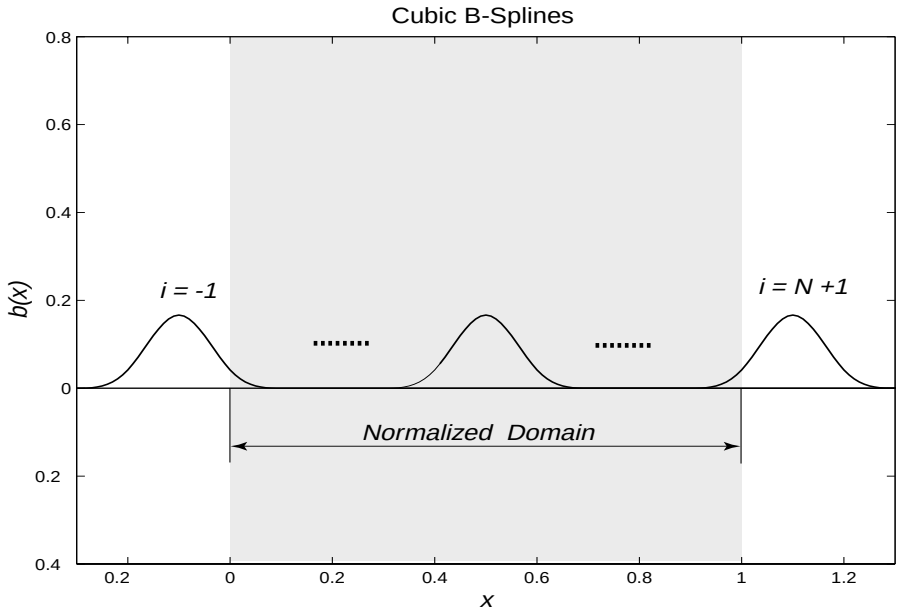

Figure B.1: Basis of cubic B-splines for N=10.

B.3 Test Functions for Galerkin Discretization of PDE's

The test functions used in the Galerkin approximations for beam PDE models are defined in linear subspaces $\{\phi_i\}^N$ of $S_3^{\hat{N}}([0,L])$ generated by the imposition of the geometric boundary conditions. As a first example, consider the approximation for the transverse displacements of a cantilever beam given by

$$w(x) \simeq w^N(x) = \sum_{i=1}^{N} a_i \phi_i(x). \tag{B.4}$$

The geometric boundary conditions to be satisfied are $w(0) = 0$ and $w'(0) = 0$. Select ϕ_i such that

$$\begin{aligned} \phi_1 &= -2\hat{b}_{-1} + \hat{b}_0 - 2\hat{b}_1 \\ \phi_i &= \hat{b}_i, \quad 2 \le i \le N = \hat{N} + 1 \end{aligned} \tag{B.5}$$

and the geometric BC's will be automatically satisfied by $w^N(x)$. Similarly, for a simply-supported beam, define

$$\phi_1 = \hat{b}_0 - 4\hat{b}_{-1}$$

$$\begin{aligned} \phi_2 &= \hat{b}_1 - \hat{b}_0/4 \\ \phi_i &= \hat{b}_{i-1}, \quad 3 \leq i \leq N-2 \\ \phi_{N-1} &= \hat{b}_{\hat{N}-1} - \hat{b}_{\hat{N}}/4 \\ \phi_N &= \hat{b}_{\hat{N}} - 4\hat{b}_{\hat{N}+1} \end{aligned} \tag{B.6}$$

and the conditions $w(0) = 0$ and $w(L) = 0$ will be satisfied by $w^N(x)$. For the free-free case, $\{\phi_i\}^N \equiv \mathcal{B}$ and consequently $N = \hat{N} + 3$. Variations of the linear combinations described in Eqs. (B.5) and (B.6) can be used to impose the most common boundary conditions (free, clamped, pinned) both in Euler-Bernoulli and Timoshenko beam models.

Vita

Capt. Sergio H. S. Carneiro was born on January 29, 1964, in Rio de Janeiro, RJ, Brazil, the first child of Joaquim M. S. Carneiro and Neli C. S. Carneiro. He graduated from the ITA - Instituto Tecnológico de Aeronáutica, in São José dos Campos, SP, Brazil, in December, 1987, with a Bachelors degree in Aeronautical Mechanics Engineering. While in college, Sergio joined the Brazilian Air Force and upon graduation he was assigned to the Air Force Institute of Aeronautics and Space (CTA/IAE) in São José dos Campos, SP as a researcher in the Space Systems Division. In January of 1990 he married the former Lúcia Fernandes da Silva and together they celebrated the birth of Pedro Henrique F. Carneiro in June, 1992. During his tenure at CTA/IAE, Sergio combined a full-time job with part-time graduate studies at ITA, and graduated with a Masters of Science in Aeronautics and Mechanics in December, 1993. The Carneiro family joyfully welcomed a new member with the birth of Letícia F. Carneiro in November, 1995. In 1996, Sergio was selected to pursue a Ph.D. degree in the US and was assigned to the Department of Engineering Science and Mechanics at Virginia Polytechnic Institute and State University starting in August, 1996, under the supervision of Prof. Daniel J. Inman. Upon graduation, Sergio will return to Brazil and resume his assignment at CTA/IAE, now joining the Structural Integrity Group in the Aeronautical Systems Division.